Time-reversed measurement of the ^{18}Ne(α,p)^{21}Na cross-section for Type I X-ray bursts

Philip J. C. Salter

A thesis submitted in fulfilment of the requirements
for the degree of Doctor of Philosophy
to the
University of Edinburgh
April 2012

For
My Loving Family

Abstract

Type I X-ray bursts (XRB) are highly energetic and explosive astrophysical events, observed as very sudden and intense emissions of X-rays. X-ray bursts are believed to be powered by a thermonuclear runaway on the surface of a neutron star in a binary system. XRB models are dependent on the accurate information of the nuclear reactions involved. The ^{18}Ne(α,p)^{21}Na reaction is considered to be of great importance as a possible breakout route from the Hot-CNO cycle preceding the thermonuclear runaway.

In this thesis work, the ^{18}Ne(α,p)^{21}Na reaction cross-section was indirectly measured at $E_{cm}(\alpha,p)$ = 2568, 1970, 1758, 1683, 1379 and 1194 keV, using the time-reverse ^{21}Na(p,α)^{18}Ne reaction. Since the time-reverse approach only connects the ground states of ^{21}Na and ^{18}Ne, the cross sections measured here represent lower limits of the ^{18}Ne(α,p)^{21}Na cross-section. An experiment was performed using the the ISAC-II facility at TRIUMF, Vancouver, Canada. A beam of ^{21}Na ions was delivered to a polyethylene $(CH_2)_n$ target placed within the TUDA scattering chamber. The reaction ^{18}Ne and ^{4}He ions were detected using silicon strip detectors, with time-of-flight and $\Delta E/E$ particle identification techniques used to distinguish the ions from background. The measurement at E_{cm} = 1194 keV is the lowest energy measurement to date of the ^{18}Ne(α,p)^{21}Na cross section.

The measured cross sections presented in this thesis were compared to the NON-SMOKER Hauser-Feshbach statistical calculations of the cross section and to the unpublished results of another time-reverse investigation performed by a collaboration at the Argonne National Laboratory. A ^{18}Ne(α,p)^{21}Na reaction rate calculation based on the measured cross sections was performed. In comparison with previous reaction rate estimates, our results indicate a rate that is about a factor 2-3 lower than Hauser-Feshbach calculations, suggesting that a statistical approach may not be appropriate for cross section calculations for nuclei in this mass region. The astrophysical consequences of our new results appear to remain nevertheless negligible. These are also presented in this thesis.

Acknowledgements

I would like to begin by thanking my supervisor Marialuisa Aliotta, for her guidance, inspiration and encouragement, without which this thesis would not have been possible. Thanks to Phil Woods and Alex Murphy for their suggestions and advice, and special thanks to Tom Davinson for his patience, advice and support. Thank you to Gordon Turnball for all his technical support in the laboratory.

Thank you to my fellow students in the Edinburgh Nuclear Physics Group, both those who have moved to pastures new and those still working here. You have provided me with much support, friendship and advice over the last four years and I am grateful to you all; I wish I could name every one but there are just so many of you!

I wish to thank those in the York Nuclear Physics Group who have been involved in the last four years; especially Alison Laird for inspiring me to move to Edinburgh to study a PhD, and Matt Taggart for his advice and friendship. And I must not forget Paul Mumby-Croft; I forgot to include you in my MPhys dissertation acknowledgements so I would like to take this opportunity to thank you now.

A special mention to my experimental partner in crime, Clare Beer. Our experiences at TRIUMF will stay with me forever, you are a great friend and your support over the last four years has helped me greatly. Thank you for introducing me to chocolate covered coffee beans!

Thank you to my close friends Emma, Duncan, Hugo and Michelle. I am truly grateful of your friendship; your support has kept me going through the tough times. Thank you to Joe Mancell and Simon Myers; your continued friendship is greatly appreciated. It has meant a lot to me.

Mum, Dad and Emily, thank you for all your love and support. Without

which I would not have taken that giant leap to Edinburgh. Emily, thank you for keeping me sane, and Mum, thank you for always being there. Dad, thank you for inspiring me from an early age, I have always enjoyed chatting about the scientific news with you.

And finally, thank you to Laura. I owe you so much. Thank you for putting up with me and my physics for the last four years. Thank you for your constant encouragement, love and support. Thank you for always being there for me and for making me smile. Thank you.

Declaration

The experiment described in this thesis was performed by myself, fellow members of the University of Edinburgh Nuclear Physics Group, and our collaborators at TRIUMF. The data analysis and interpretation of results are my own work, and this thesis has been written by myself. No portion of the work referred to in this thesis has been submitted in support of an application for another degree qualification at this university or any other academic institution.

P. J. C. Salter
April 2012

Contents

List of Figures

List of Tables

Introduction

No one regards what is before his feet; we all gaze at the stars.

Quintus Ennius
(239-169 B.C.)

It is fundamental to human nature to question the universe in which we exist. The field of Nuclear Astrophysics is the study of the nuclear processes which drive the birth, evolution and death of stars; it is quite fitting that to understand the macroscopic world of stars, we need to investigate the microscopic world of nuclear physics.

Interpretation of the observed Galactic elemental and isotopic abundance distributions, beginning with the the famous Burbidge, Burbidge, Fowler and Hoyle paper [1], in terms of primordial and stellar nucleosynthesis has been one of the greatest successes of nuclear astrophysics. Space-based observatories probing the electromagnetic spectrum from infrared to γ-ray wavelengths have multiplied the amount of information about abundance distributions in the winds of massive stars, in the ejecta of nova and supernova, and about galactic X- and γ-ray sources, linking the production of various elements directly with certain astrophysical sites. And advances in computing have allowed the development of increasingly sophisticated models of stellar hydrodynamics that, in explosive events, are driven by the nuclear processes. Direct comparisons between the predicted and observed energy emission and time-scales of explosive events yield information about the temperature, density and hydrodynamical conditions in the stellar explosion. A complete interpretation of the observations, however, requires a detailed knowledge and understanding of the underlying nuclear physics.

Nucleosynthesis and energy generation in stellar environments both depend on the time-scales of the relevant nuclear processes. While slow throughout most of a star's life, nucleosynthesis and energy generation become exceedingly fast in explosive conditions, leading to dramatic increases in the luminosity of novae, supernovae, X-ray bursts and γ-ray bursts. Quiescent nuclear burning is characterised by processes with time-scales much longer than typical nuclear β-decay lifetimes, whereas, reactions that occur in explosive environments, where extreme temperatures and densities are encountered, are often much quicker than the β-decay time-scales. Under these conditions, nuclear reactions can occur far from β-stability. An understanding of these nuclear reactions, therefore, requires detailed studies of nuclear structure, nuclear reactions and decay mechanisms for unstable nuclei. Models applied to these explosive scenarios are often based on rather simple predictions for nuclear reaction rates and decay properties. Though the basic concept of nucleosynthesis and energy generation in explosive scenarios is quite well understood, detailed experimental information and improved observational data allow for a deeper analysis of the hydrodynamic conditions of dynamic events such as novae, supernovae and X-ray bursts. Much of the required experimental information can be obtained with measurements involving radioactive ion beams. However, most nuclear reactions are extremely difficult to study, owing to the low reaction cross sections and low beam intensities available at present.

The focus of this thesis is the investigation of the ^{18}Ne(α,p)^{21}Na nuclear reaction relevant to X-ray bursts. The reaction is thought to be an important breakout route from the Hot-Carbon-Nitrogen-Oxygen cycle during the X-ray burst nucleosynthesis. Chapter 1 of this thesis introduces the X-ray burst phenomenon and highlights the nuclear reactions which are believed to be responsible for such an explosive event and the motivation for studying the ^{18}Ne(α,p)^{21}Na reaction. Chapter 2 outlines the theory of two important nuclear reaction mechanisms in the X-ray burst environment that are relevant to this work. Chapter 3 presents a summary of all previous investigations of the ^{18}Ne(α,p)^{21}Na reaction and the most recent results, and highlights discrepancies between data sets where present. Chapter 4 outlines the methodology used to perform a measurement of the ^{18}Ne(α,p)^{21}Na cross section, and chapter 5 describes the experimental procedure involved in the measurement. Chapters 6 and 7 are concerned with the methods of analysis, results and conclusions drawn from the analysis. And the final chapter is a short summary of this thesis work and proposal of possible future work.

Chapter 1

The X-ray Burst Phenomenon

This chapter introduces the X-ray burst phenomenon, and relevant to this study, the Type-I X-ray burst. The nuclear processes considered to be responsible for a Type-I X-ray burst are presented, and the motivation for measuring the ^{18}Ne(α,p)^{21}Na cross section at astrophysical energies is introduced.

1.1 Observational Features

Extensive studies of the X-ray burst phenomena have been made using a number of space-based X-ray observatories, such as RXTE [2], BeppoSAX [3], Chandra [4], HETE-2 [5] and XMM/Newton [6]. As of 2010, there have been 92 galactic X-ray burst sources identified [7], since their discovery in 1976 [8], and the first extragalactic X-ray burst sources have been identified in two globular cluster candidate sources of the Andromeda galaxy. X-ray bursts are categorised as either type-I or type-II; type-I are the most common and form the focus of this work.

Type-I X-ray bursts are typically characterised by sudden and intense emissions of X-rays, with energies of 10^{39}-10^{40} ergs[1] over a luminosity rise time of 1-10 seconds, followed by an exponential like decay in the luminosity over a time-scale of 10-100 seconds. Type I X-ray bursts typically repeat on a time-scale of hours-days; the luminosity spectrum of a type-I X-ray burst observation by the EXOSAT satellite [9] is shown in Figure 1.1: the bursts clearly repeat on a time-scale of approximately three hours.

---

[1] 1 erg = 624.15MeV

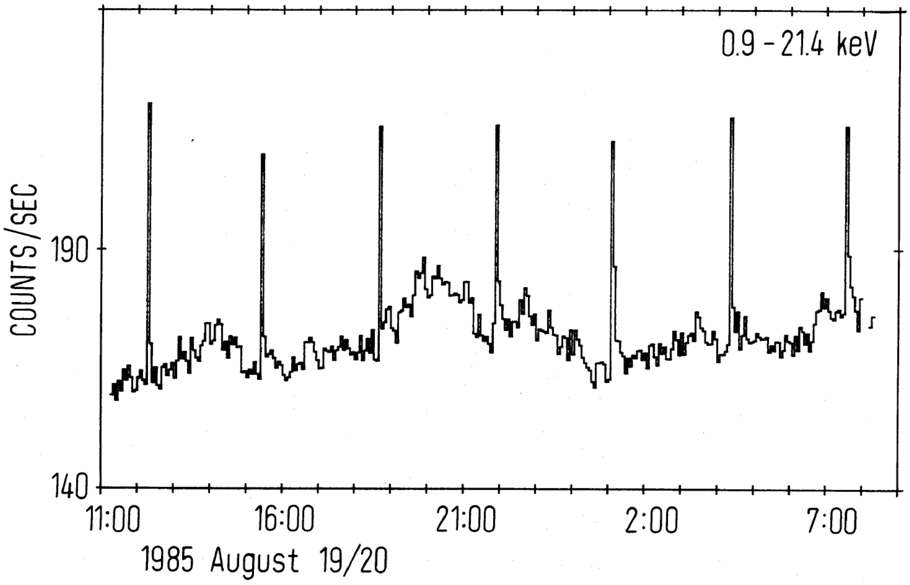

Figure 1.1: *Type I X-ray burst light curve. Observation made by the EXOSAT satellite over a 20 hour period on 19/20 August 1985 [9].*

1.2 The X-ray Burst Model

It is estimated that approximately half of all stars in the Galaxy exist as binary systems [10]. The evolution of a binary system can depend on the separation of the two stellar bodies, and if they are close, both stars may interact via the transfer of matter. Each star in a binary system has a hypothetical *Roche* lobe that represents the volume within which orbiting material gravitationally bound to the star. A schematic diagram depicting the Roche lobes of two stars in a close binary system is shown in Figure 1.2; the point at which the Roche lobe of the two stars intersects is known as the *inner Lagrangian point*. If one of the stars evolves off the main sequence and becomes a *Red Giant*, the star may fill its Roche lobe, and any further expansion of the Red Giant results in the transfer of material through the inner Lagrangian point to the Roche lobe of the companion star. A close binary system in which material is transferred from one star to the other is referred to as a *semi-detached* binary system.

Type-I X-ray bursts are believed to be caused by a thermonuclear runaway on the surface of a neutron star which is accreting material from a companion star in a semi-detached binary system; an artistic impression of this scenario is shown in Figure 1.3. It is considered that hydrogen- and helium-rich material

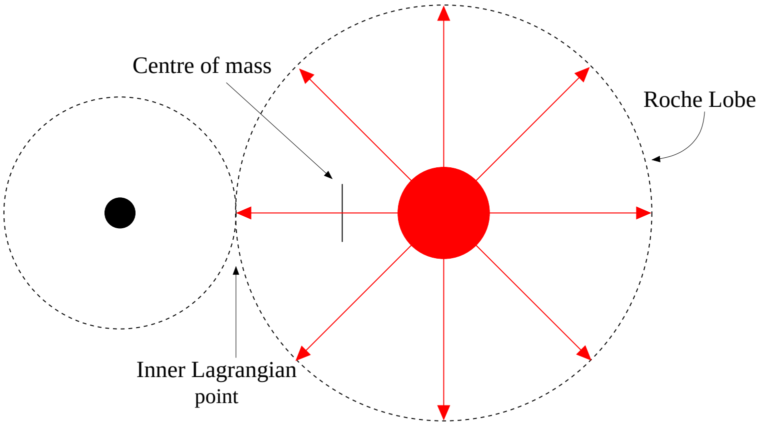

Figure 1.2: *Schematic diagram of a close binary system, showing the inner Lagrangian point and Roche lobes of the two stellar bodies. If the star on the right fills its Roche lobe and expansion persists, material may flow through the inner Lagrangian point to the companion star.*

is accreted onto the surface of a neutron star at an approximate accretion rate of 10^{-8} to 10^{-10} $M_{\odot}$ yr^{-1} [11]. An envelope of accreted matter forms as an accretion disk surrounding the neutron star, and at densities $\rho \geq 10^5$ g/cm^3, nuclear burning is ignited at the base of the envelope, via the pp-chains and CNO cycles. The high gravitational potential of the neutron star and the high densities at the base of the accreted envelope lead the matter at the base to become electron degenerate. Under these degenerate conditions, the degenerate matter in the envelope is prevented from cooling through expansion; the energy released from the nuclear burning triggers a thermal runaway, with temperatures up to T = 3 GK reached before degeneracy is lifted. At these high temperatures (T $\gtrsim$ 0.6 GK), explosive hydrogen burning via the *αp*-process and *rp*-process is triggered [12–17], which causes rapid nucleosynthesis towards heavier nuclei (A $\lesssim$ 100) and produces the energy ultimately observed as an X-ray burst. It should be noted, it is unlikely any accreted or processed matter escapes the large gravitational potential of the neutron star and therefore, an X-ray burst is not expected to seed the interstellar medium.

1.3 Nucleosynthesis in an X-ray Burst

Nuclear processes responsible for an X-ray burst are highly sensitive to temperature. The initial nuclear burning at the base of the accreted envelope

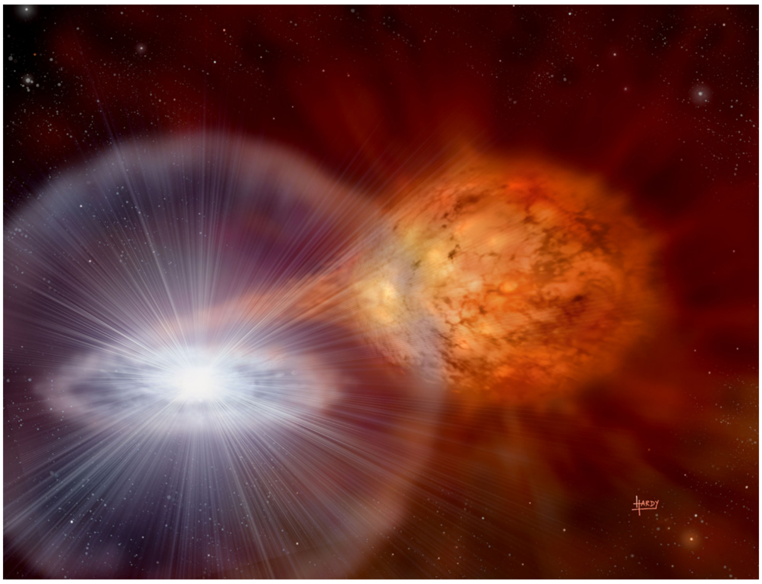

Figure 1.3: *Artistic impression of an X-ray burst event, showing the accretion of material from a companion star onto the surface of a neutron star [18].*

on the surface of the neutron star, proceeds via the pp-chains and CNO cycles. Under degenerate conditions, temperatures in excess of T ~ 0.06 GK are reached. At these extreme temperatures (and densities, $\rho \sim 10^3$ g/cm^3) it is possible for the nuclear reactions involved in the CNO cycles to occur on time-scales of a few seconds; β-unstable nuclei live long enough to be burned by nuclear reactions before they β-decay. New cycles of reactions are possible, known as the Hot-CNO (HCNO) cycles. These HCNO cycles are show in Figure 1.4.

Nuclear burning through the Hot-CNO cycles is limited by the β-decaying *waiting point* isotopes of ^{14}O, ^{15}O and ^{18}Ne. For further nucleosynthesis to occur, it is necessary to *breakout* from the Hot-CNO cycles. At temperatures T $\gtrsim$ 0.5 GK for ^{15}O and T $\gtrsim$ 0.8 GK for ^{18}Ne, the HCNO β-decaying waiting points can be bypassed by the ^{15}O(α,γ)^{19}Ne and ^{18}Ne(α,p)^{21}Na reactions respectively. Davids *et al.* [19] show there is no significant contribution to breakout from the Hot-CNO cycles via the ^{15}O(α,γ)^{19}Ne reaction for X-ray burst scenarios. Therefore, the favoured breakout sequence is ^{18}Ne(α,p)^{21}Na(p,γ)^{22}Mg(α,p)^{25}Al(p,γ)^{26}Si, which leads to a sequence of rapid proton captures, known as the *rp*-process, driving nucleosynthesis towards the proton dripline and forming nuclei with masses up to A ~ 100. A schematic of the path of the *rp*-process has been

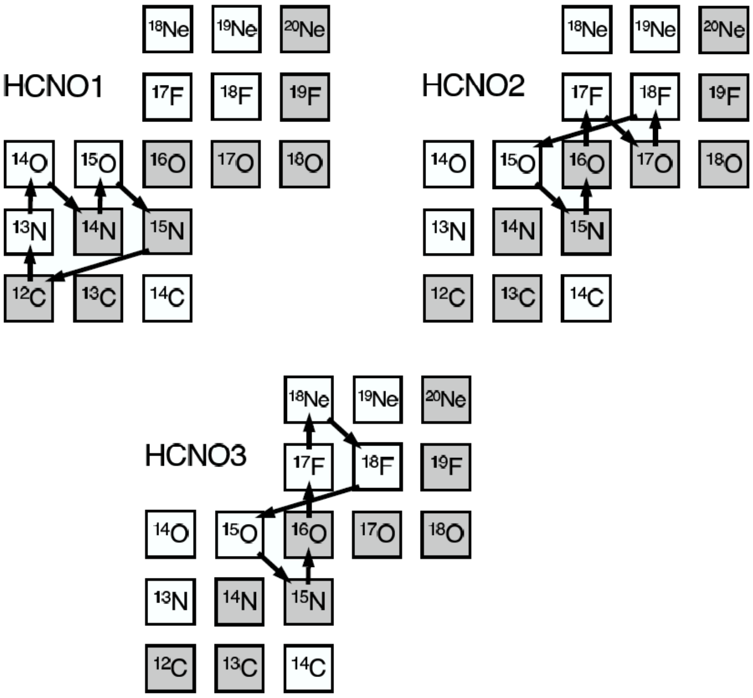

Figure 1.4: *The Hot-CNO cycles. Stable nuclei are shaded [10].*

calculated by H. Schatz [20] and is shown in Figure 1.5.

1.4 Motivation to Study the ^{18}Ne(α,p)^{21}Na Reaction

Breakout from the Hot-CNO cycle is an important precursor to the thermonuclear runaway of the *rp*-process. Models of the breakout are highly sensitive to the temperature and density conditions of the environment.

The mean lifetime of ^{18}Ne in a pre X-ray burst environment is dependent on the competing destructive ^{18}Ne(β^{+})^{18}F and ^{18}Ne(α,p)^{21}Na reactions. An illustration of the temperature and density conditions at which either destructive reaction is believed to dominate is shown in Figure 1.6: the contour corresponds to conditions for which the rates/cross-sections of both destructive reactions are equal (assuming a solar composition for the accreted material, with a helium mass fraction of 0.27). Nucleosynthesis to the left of the contour recycles material back to the Hot-CNO cycle, and to the right of the contour, nucleosynthesis towards the *rp*-process can occur. Typical densities at the base

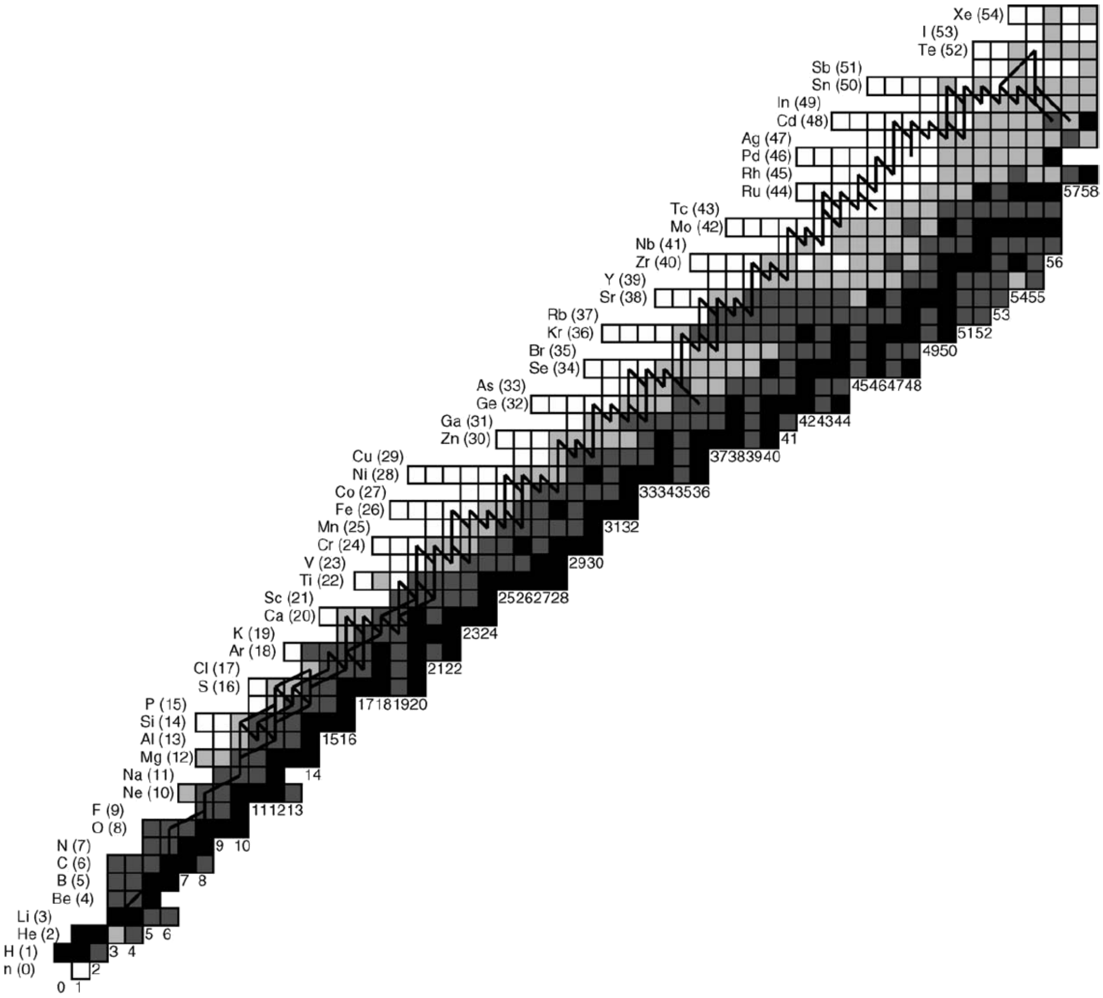

Figure 1.5: *The path of the rp-process on the chart of nuclides [20]. Stable nuclei are represented in black, unstable nuclei with experimentally known masses are shown in various shades of grey: dark-grey for masses with an uncertainty of 10 keV or less, and light-grey for masses with larger than 10 keV uncertainty.*

of an accreted envelope on the surface of a neutron star are believed to be in the range ρ = 10^5 - 10^7 g/cm^3 [21]. At this density range, breakout from the Hot-CNO cycle through the ^{18}Ne(α,p)^{21}Na reaction is seen to occur in the temperature range T = 0.6 - 0.8 GK.

The position of the contour in Figure 1.6 is dependent on accurate knowledge of the ^{18}Ne(α,p)^{21}Na reaction rate. Any variation of the reaction rate has the potential to change the position of the density-temperature contour; moving the location of Hot-CNO breakout to higher or lower temperatures, with implications on the X-ray burst model which are beyond the scope of this work and given elsewhere [22, 23]. However, as will be discussed in Chapter 3, there is current uncertainty in the ^{18}Ne(α,p)^{21}Na reaction rate, especially for temperatures $T < 1$ GK relevant for Hot-CNO breakout. It is therefore obvious that an investigation of the ^{18}Ne(α,p)^{21}Na reaction is warranted given the importance in the role the reaction plays as a Hot-CNO breakout route.

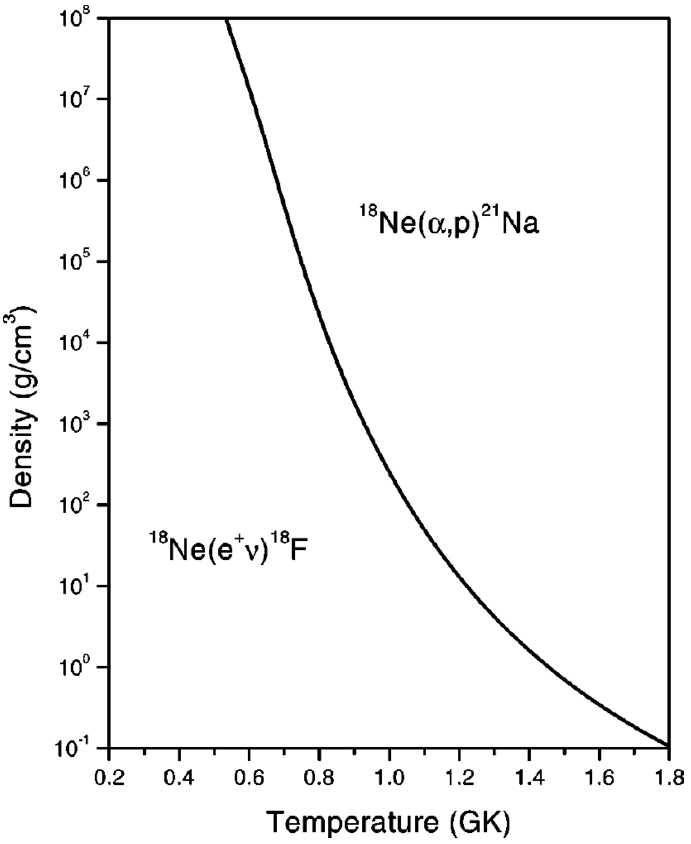

Figure 1.6: *The conditions under which the* ^{18}*Ne*(β^+)^{18}*F and* ^{18}*Ne*(α,*p*)^{21}*Na reactions are believed to dominate the destruction of* ^{18}*Ne (assuming a solar composition of the material accreted onto the neutron star surface). The contour corresponds to the conditions at which the* β*-decay and* (α,*p*) *reaction rates are equal [21].*

Chapter 2

Thermonuclear Reactions in Stars

Key to our understanding of energy generation and nucleosynthesis in X-ray burst environments is an in-depth knowledge of thermonuclear reactions and in particular reaction rates.

In this chapter, we discuss the general properties of stellar reaction rates and identify two reaction mechanisms, resonant and non-resonant, that are important in Nuclear Astrophysics, and present an analytical formalism for the determination of the reaction rate for each reaction mechanism. This is not an extensive description of all reaction theory, but provides the critical elements required to understand this thesis work.

2.1 Cross Sections and Stellar Reaction Rates

The probability that a nuclear reaction will occur, or 'cross section', is a very useful quantity when modelling stellar reactions, especially in determining how many reactions occur per unit time and unit volume. The cross section, σ, of a reaction is dependent on the energy at which the reaction occurs and therefore the velocity of the reacting particles, *i.e.* $\sigma = \sigma(v)$ where v is the relative velocity between the interacting particles. If we consider the reaction X(a,b)Y in a unit volume of stellar gas, involving N_a particles of a and N_X particles of X, the rate at which the reaction occurs, or *reaction rate* is expressed as:

$$r = N_X N_a v \sigma(v) \tag{2.1}$$

where r is in units of reactions per unit time per unit volume.

In a stellar environment the particle velocities are given by the probability function $\phi(v)$, where

$$\int_0^\infty \phi(v)dv = 1 \tag{2.2}$$

with $\phi(v)\mathrm{d}v$ representing the probability that the relative velocity, v, is between v and $v + \mathrm{d}v$.The reaction rate per particle pair is subsequently expressed as:

$$< \sigma v > = \int_0^\infty \phi(v) v \sigma(v) dv \tag{2.3}$$

and the total reaction rate becomes:

$$r = N_X N_a < \sigma v > \tag{2.4}$$

In a stellar environment, the energy available to nuclei to interact comes from thermal motion; reactions initiated by thermal motion are called *thermonuclear reactions*, and the movement of nuclei can be described as non-relativistic. The velocities of these nuclei are therefore approximated by a Maxwell-Boltzmann velocity distribution:

$$\phi(v) = 4\pi v^2 \left(\frac{\mu}{2\pi kT}\right)^{\frac{3}{2}} exp\left(-\frac{\mu v^2}{2kT}\right) \tag{2.5}$$

where T is the temperature of the stellar plasma, μ is the reduced mass of the system, $\mu = m_a m_X/(m_a + m_X)$, and k the Boltzmann constant. The above function, $\phi(v)$, can be expressed in terms of energy such that:

$$\phi(E) \propto E exp\left(\frac{-E}{kT}\right) \tag{2.6}$$

Combining the above with Equation 2.3, the reaction rate per particle pair for a stellar plasma becomes:

$$\begin{aligned} < \sigma v > &= \int_0^\infty \phi(v)\ v\ \sigma(v)\ dv = \int_0^\infty \phi(E)\ v\ \sigma(E)\ dE \\ &= \left(\frac{8}{\pi\mu}\right)^{\frac{1}{2}} \frac{1}{(kT)^{\frac{3}{2}}} \int_0^\infty \sigma(E)\ E\ exp\left(\frac{-E}{kT}\right)\ dE \end{aligned} \tag{2.7}$$

2.2 Charged-Particle-Induced Non-resonant Reaction

A reaction that proceeds as a single-step process, where there is a single transition from the initial state (a+X) to a final state (b+Y), is referred to as a *direct* or *non-resonant* reaction, and may occur at all projectile energies.

For charged particles to react, the effective potential barrier, *V(r)*, that exists between the particles must be overcome. The potential barrier that exists between the two charged particles, each of charge $Z_a e$ and $Z_X e$, and separated by a distance r, consists of two components; the repulsive Coulomb potential between positive charges:

$$V_c(r) = \frac{Z_a Z_X e^2}{4\pi\epsilon_0 r} \tag{2.8}$$

and the centrifugal potential arising from the relative orbital angular momentum of the particles:

$$V_{cf}(r) = \frac{l(l+1)\hbar^2}{2\mu r^2} \tag{2.9}$$

To reach the nuclear interaction distance[1], R_n in Figure 2.1, where the particles interact via the strong force and a nuclear reaction can occur, then either the energy of approach of the charged particles must be greater than the height of the potential barrier, or the potential barrier is penetrated in a phenomenon called *Quantum Tunnelling*.

The energy dependent cross section for charged-particle-induced reactions, $\sigma(E)$, is given by:

$$\sigma(E) = \frac{1}{E} exp(-2\pi\eta) S(E) \tag{2.10}$$

Here, the exp(-$2\pi\eta$) term arises from the barrier penetration probability, where η = $Z_1 Z_2 e^2/\hbar v$ and is called the *Sommerfeld* parameter[2]; the *1/E* term arises from the geometrical energy-dependent de Broglie wavelength of the particle, $\pi/k^2 \propto 1/E$; and the function *S(E)* is known as the *astrophysical S-factor* and contains all the strictly nuclear effects. A useful property of the S-factor is that it is a smoothly varying function of energy, varying much less with energy than the cross section, as shown in Figure 2.2.

---

[1] $R_n = R_a + R_X$, where R_a and R_X are the nuclear radii of the two interacting particles.

[2] $2\pi\eta = 31.29 Z_1 Z_2 \left(\frac{\mu}{E}\right)^{\frac{1}{2}}$, with E and μ in units of keV and *amu* respectively.

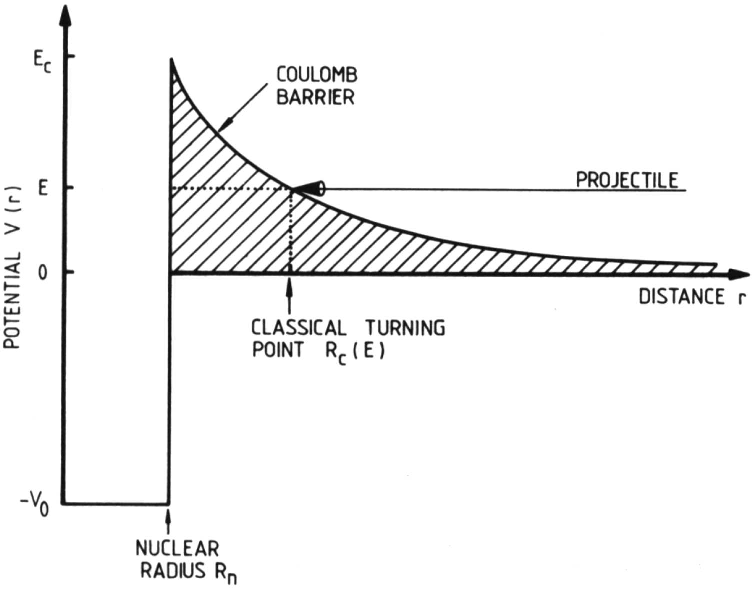

Figure 2.1: *Schematic representation of the effective potential between two positively charged nuclei. For a projectile with energy* $E < E_c$*, the barrier must be penetrated to reach the nuclear radius,* R_n*. The classical turning point,* R_c*, is the closest distance the projectile reaches before penetration of the barrier is required [24].*

If Equation 2.10 is placed into Equation 2.7, the reaction rate per particle pair for a non-resonant reaction is given by:

$$< \sigma v > = \left(\frac{8}{\pi\mu}\right)^{\frac{1}{2}} \frac{1}{(kT)^{\frac{3}{2}}} \int_0^{\infty} S(E) exp\left(-\frac{E}{kT} - 2\pi\eta\right) dE \tag{2.11}$$

The energy dependence in Equation 2.11 is dominated by the two exponential terms: the *exp(-E/kT)* term is a measure of the number of particles in the high energy tail of the Maxwell-Boltzmann distribution and disappears at high energies; the remaining exponential term is the penetrability of the Coulomb barrier, which is very small at low energies. The product of these two exponential terms gives rise to a peak of the integrand close to an energy E_0, shown in Figure 2.3; the peak is known as the *Gamow* peak, and E_0 is given by:

$$E_0 = \left(\frac{bkT}{2}\right)^{\frac{2}{3}} \tag{2.12}$$

$$= 1.22\left({Z_a}^2 {Z_X}^2 \mu {T_6}^2\right)^{\frac{1}{3}} \quad \text{(keV)} \tag{2.13}$$

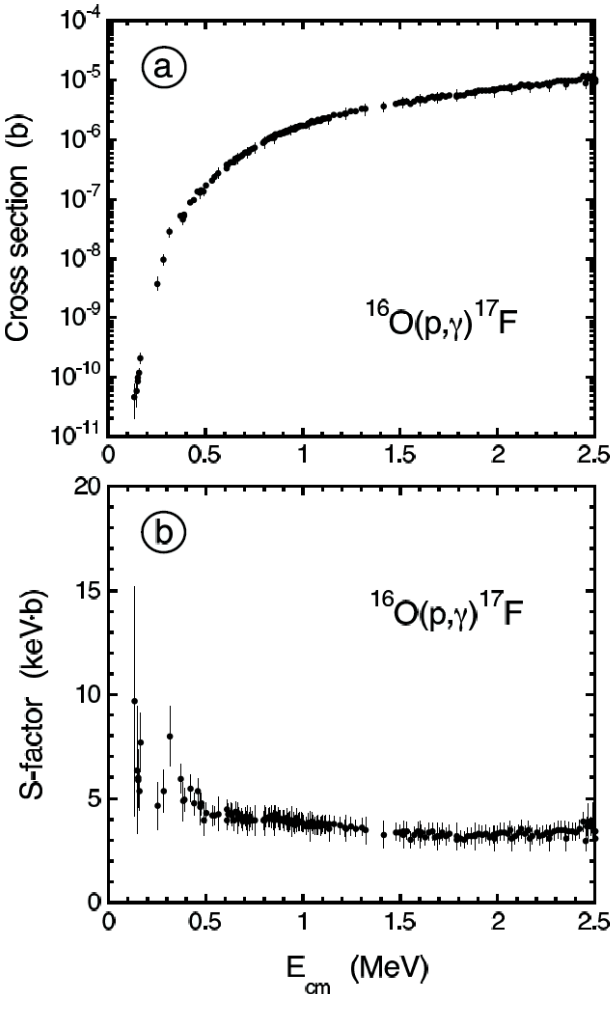

Figure 2.2: *(a) Experimental cross section and (b) astrophysical S-factor of the $^{16}O(p,\gamma)^{17}F$ reaction. The cross section has a strong energy dependence and falls rapidly for energies below the Coulomb barrier, the S-factor is much less energy dependent and varies more linearly with energy. The data for these plots are from [25], the plots are from [10].*

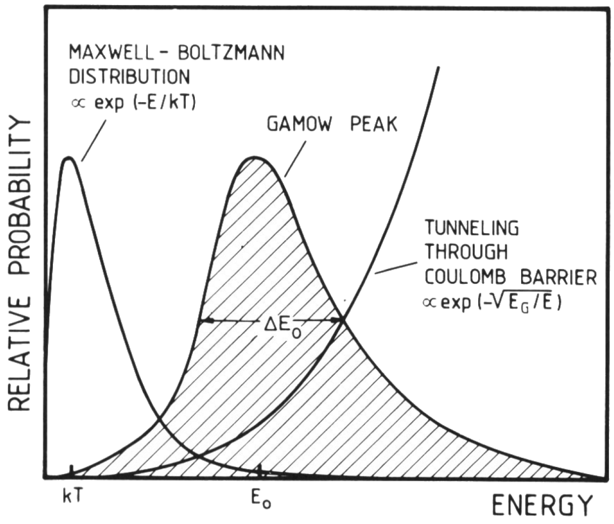

Figure 2.3: *The convolution of the Maxwell-Boltzmann distribution and the Coulomb barrier penetrability gives rise to a peak, known as the Gamow peak, about the energy E_0. The energy E_0 is the effective mean energy for a thermonuclear reaction at a temperature T [24].*

where $b = (2\mu)^{\frac{1}{2}}\pi e^2 Z_a Z_X/\hbar$ and $T_6 = T\times10^6$ K. The energy E_0 is the effective mean energy for a thermonuclear reaction at a temperature T. If the Gamow peak is approximated as a Gaussian function, the effective width of the Gamow peak can be expressed as:

$$\Delta E_0 = \frac{4}{\sqrt{3}}(E_0 kT)^{\frac{1}{2}} \tag{2.14}$$

$$= 0.749\left(Z_1{}^2 Z_2{}^2 \mu T_6{}^5\right)^{\frac{1}{6}} \quad \text{(keV)} \tag{2.15}$$

For a given stellar temperature T, the effective width of the Gamow peak is relatively narrow; the $S(E_0)$ factor can be considered to be approximately constant over the peak width and can therefore be taken out of the integral in Equation 2.11 to give the reaction rate per particle pair for a non-resonant reaction:

$$<\sigma v> = \left(\frac{8}{\pi\mu}\right)^{\frac{1}{2}} \frac{1}{(kT)^{\frac{3}{2}}} S(E_0) \int_0^\infty exp\left(-\frac{E}{kT} - 2\pi\eta\right) dE \tag{2.16}$$

In a stellar environment non-resonant reactions are not the only mechanism through which a reaction may proceed. Resonances may exist within the width of the Gamow peak which may have a strong effect on the cross section and thus may dominate the reaction rate. In the following section we shall discuss a particular type of resonant reaction involving *isolated* and *narrow* resonances.

2.3 Narrow Resonance Reaction

In contrast to non-resonant reactions, a reaction may proceed through an excited state E_x of a compound nucleus, C, which subsequently decays to the exit channel products:

$$a + X \rightarrow C^* \rightarrow b + Y \tag{2.17}$$

This reaction mechanism is referred to as a *resonant* reaction and may only occur if the centre-of-mass kinetic energy of the entrance channel particles, a and X, coincides with the energy, E_x, of one of the excited, or *resonant*, states of the compound nucleus. Furthermore, conservation of angular momentum demands that:

$$\vec{J} = \vec{j_a} + \vec{j_X} + \vec{l} \tag{2.18}$$

for a resonance to occur, where $\vec{J}$ is the angular momentum of the resonant state in the compound nucleus, $\vec{j_a}$ and $\vec{j_X}$ the spin of the entrance channel particles, and $\vec{l}$ the orbital angular momentum of a relative to X. In addition, parity conservation requires that:

$$(-1)^l \, \pi(j_a) \, \pi(j_X) = \pi(J) \tag{2.19}$$

where $\pi(j_a)$ and $\pi(j_X)$ are the parities of the reacting particles and $\pi(J)$ is the parity of the resonant state. For spinless particles in the entrance channel with parities $\pi(j_a) = \pi(j_X) = +1$, the parity of the resonant state is determined by the orbital angular momentum of the entrance channel: $(-1)^l = \pi(J)$; the resonant state is referred to as having *natural* parity. Conversely, a resonant state with $(-1)^l \neq \pi(J)$ is known as an *unnatural* parity state.

For reactions that occur on or near a resonant energy, there is a rapid increase or decrease in the reaction cross-section/astrophysical S-factor over a small energy range. The cross section can be considered as a product of the probabilities of the formation and decay of the compound nucleus, usually expressed in terms of partial width Γ_i:

$$\sigma \propto \Gamma_a \Gamma_b \tag{2.20}$$

where Γ_a is the partial width for the formation and Γ_b the partial width for the decay of the compound state. The total width of a resonance is the sum of the partial widths of all open decay channels:

$$\Gamma = \Gamma_a + \Gamma_b + \Gamma_c + ... \tag{2.21}$$

For a narrow resonance, typically where the resonance energy in the entrance channel is much greater than the resonance total width, $E_R >> \Gamma$, the reaction cross section is described by the Breit-Wigner formula:

$$\sigma_{BW}(E) = \frac{\lambda^2}{4\pi}(1+\delta_{Xa})\frac{(2J+1)}{(2j_X+1)(2j_a+1)}\frac{\Gamma_a\Gamma_b}{(E-E_R)^2+\Gamma^2/4} \tag{2.22}$$

where $\lambda = 2\pi\hbar/\sqrt{2\mu E}$, and E_R is the resonance energy in the entrance channel. All energies and widths are in the centre-of-mass system. The term $(1+\delta_{Xa})$, with δ_{Xa} Kronecker delta, takes into account the factor of two increase on the cross section if the nuclei in the entrance channel are identical.

Equation 2.22 can be inserted into Equation 2.7 to obtain the stellar reaction rate per particle pair for a narrow resonance:

$$\begin{aligned} <\sigma v> &= \left(\frac{8}{\pi\mu}\right)^{\frac{1}{2}}\frac{1}{(kT)^{\frac{3}{2}}}\int_0^\infty \sigma_{BW}(E)\, E\, exp\left(\frac{-E}{kT}\right) dE \\ &= \frac{\sqrt{2\pi}\hbar^2}{(\mu kT)^{\frac{3}{2}}}\,\omega\int_0^\infty \frac{\Gamma_a\Gamma_b}{(E-E_R)^2+\Gamma^2/4}\, exp\left(-\frac{E}{kT}\right) dE \end{aligned} \tag{2.23}$$

where $\omega = (2J+1)(1+\delta_{Xa})/[(2j_X+1)(2j_a+1)]$. Over a sufficiently narrow resonance, the Maxwell Boltzmann factor and the partial widths are approximately constant and can be replaced by their values at $E = E_R$ and taken outside the integral:

$$<\sigma v> = \frac{\sqrt{2\pi}\hbar^2}{(\mu kT)^{\frac{3}{2}}}\, exp\left(-\frac{E_R}{kT}\right)\,\omega\,\frac{\Gamma_a\Gamma_X}{\Gamma}\, 2\int_0^\infty \frac{\Gamma/2}{(E-E_R)^2+\Gamma^2/4}\, dE$$

$$= \left(\frac{2\pi}{\mu kT}\right)^{\frac{3}{2}} \hbar^2 \, exp\left(-\frac{E_R}{kT}\right) \, (\omega\gamma) \tag{2.24}$$

where $\omega\gamma = \omega\Gamma_a\Gamma_X/\Gamma$ and is proportional to the area under the resonance cross section curve. $\omega\gamma$ is referred to as the *resonance strength*.

When several narrow resonances contribute to a nuclear reaction, the reaction rate per particle pair is given by the sum of the individual contributions:

$$< \sigma v > = \left(\frac{2\pi}{\mu kT}\right)^{\frac{3}{2}} \hbar^2 \sum exp\left(-\frac{E_i}{kT}\right)(\omega\gamma)_i \tag{2.25}$$

In scenarios where several narrow resonances contribute to the reaction rate, a detailed knowledge of the resonance energies, total widths and partial widths is required in order to calculate the reaction rate.

In the previous sections, narrow resonance and non-resonant contributions to the reaction rate have been discussed separately. In general, however, both these reaction mechanisms can contribute to the total reaction rate over the effective energy range in the stellar environment. There may also be interference effects between resonances of the same spin and parity which can amplify or reduce the reaction rate. For a calculation of the total reaction rate, all mechanisms that contribute to the rate in the effective astrophysical energy range have to be taken into account. As we will see in the next chapter, for the case of the ^{18}Ne(α,p)^{21}Na reaction, there is much uncertainty in the reaction rate arising from discrepancies between experimental measurements of the cross section, calculations of the cross section based on experimentally measured properties of resonances, and theoretical approximations of the cross section.

Chapter 3

Current status of the ^{18}Ne(α,p)^{21}Na Reaction

There is currently considerable uncertainty in the ^{18}Ne(α,p)^{21}Na reaction rate; previous attempts to measure the reaction directly have produced ambiguous results, and there are discrepancies between theoretical calculations and experimental data. This chapter summarises the current state of the art of the ^{18}Ne(α,p)^{21}Na reaction.

The first estimate of the ^{18}Ne(α,p)^{21}Na reaction rate was made by Görres *et al.* [26], using the limited experimental data available at the time on the level structure of the compound ^{22}Mg nucleus; only two α-unbound natural parity states in ^{22}Mg above the ^{18}Ne+α threshold (E_x = 8.14 MeV) were known: E_x = 8.29 MeV and E_x = 8.55 MeV. Görres *et al.* used the mirror nucleus ^{22}Ne to estimate the energy, spin and resonance strength of predicted states in ^{22}Mg, and calculated the reaction rate based on the estimated resonance parameters; a summary of the resonance parameters used in the calculation is provided in Table 3.1. The reaction rate calculated by Görres *et al.* is shown in Figure 3.1 and compared with the Hauser-Feshbach rate calculated with the SMOKER code [27] (the Hauser-Feshbach rate is a theoretical calculation and will be discussed in more detail later in this chapter). The Görres *et al.* reaction rate was in good agreement with the Hauser-Feshbach rate for the temperature range T = 1-3 GK, however, at astrophysically important temperatures $T < 1$ GK, the calculated rate is significantly smaller than the Hauser-Feshbach rate,

Table 3.1: *Resonance parameters estimated from the mirror* ^{22}*Ne nucleus for the* ^{18}*Ne(*α*,p)*^{21}*Na reaction rate calculated by Görres et al. [26]. The states in* ^{22}*Ne used to predict the location of resonances in* ^{22}*Mg and estimate resonance parameters are listed.*

$E_x(^{22}Mg)$ (MeV)	$E_x(^{22}Ne)$ (MeV)	J^π	E_r	$\omega\gamma$ (eV)
8.29	8.49	2^+	0.15	1.5×10^{-33}
	8.59	2^+	0.23	6.2×10^{-19}
8.55	8.74	3^-	0.41	7.8×10^{-13}
	8.98	4^+	0.65	3.9×10^{-8}
	9.10	3^-	0.96	8.4×10^{-4}
	9.72	3^-	1.58	4.0
	9.84	2^+	1.70	4.6×10^{1}
	10.05	0^+	1.91	9.8×10^{2}

and for temperatures T > 3 GK, Görres *et al.* explained the discrepancy between the two rates by the limited number of known levels in ^{22}Mg included in the reaction rate calculation.

With the aim of improving on the lack of information (resonance energies, partial and total widths and resonance strengths) on states in ^{22}Mg, there have been two attempts to investigate the ^{18}Ne(α,p)^{21}Na by a direct measurement [28, 29]. ^{18}Ne has a half-life of 1.67s so a direct measurement requires a ^{18}Ne beam on a helium target. So far, only two direct measurements have been made which, however, were limited by the low ^{18}Ne beam intensities that are available. Both direct measurements were performed at Louvain-la-Neuve, Belgium, in inverse kinematics using a ^{18}Ne beam on a helium-filled chamber. Silicon detector telescopes were housed within the chamber for the detection of the reaction protons of interest. The measurements were performed at E_{cm} = 2.0-3.0 MeV [28] and at E_{cm} = 1.7-3.0 MeV [29], corresponding to astrophysical temperatures T = 1.9-3.4 GK and T = 1.5-3.4 GK respectively. The Bradfield-Smith *et al.* [28] study identified, unambiguously, three states at 10.91, 10.99 and 11.13 MeV in ^{22}Mg, and a possible further three states at 10.58, 10.82 and 11.05 MeV: the resonance parameters and strengths of the three unambiguously identified states are presented in Table 3.2. The resonance strengths were extracted with an error of ~ 30% and used to perform calculations of the reaction rate; the reaction rate determined by Bradfield-Smith *et al.* is presented in Figure 3.2.

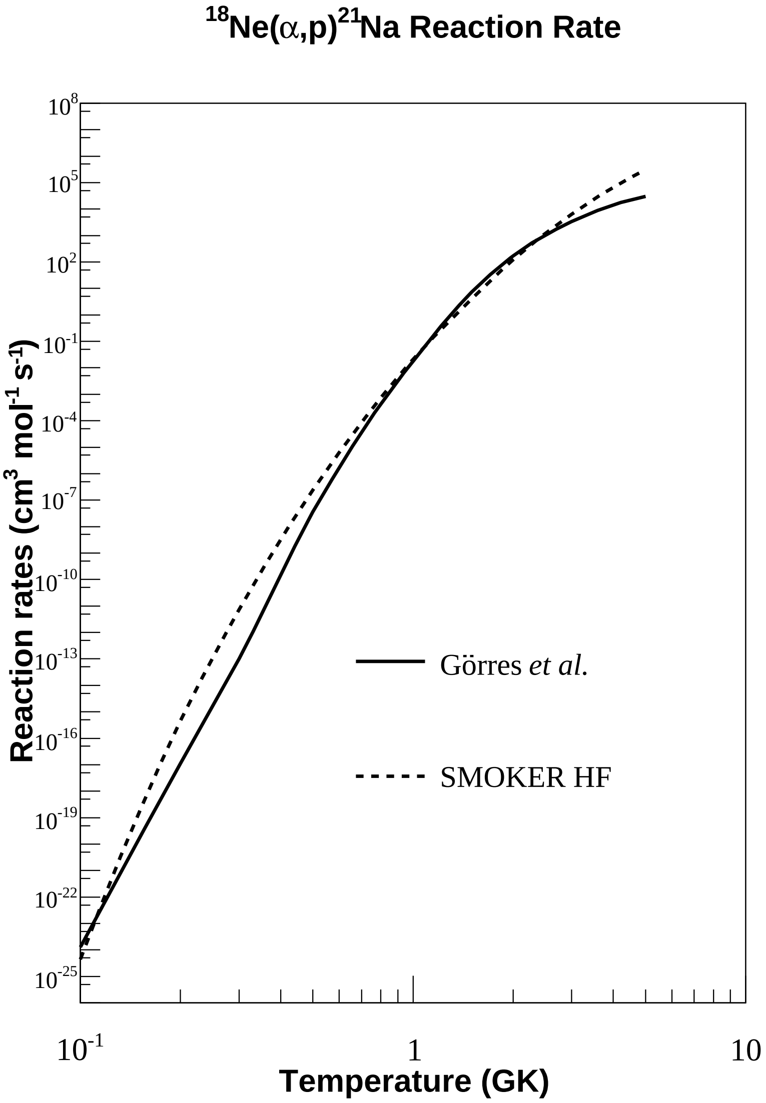

Figure 3.1: ^{18}*Ne*(α,*p*)^{21}*Na reaction rates calculated by Görres et al. [26] and the Hauser-Feshbach code SMOKER [27].*

Table 3.2: *Resonance parameters of* ^{22}*Mg states identified Bradfield-Smith et al. [28].*

$E_x(^{22}Mg)$ (MeV)	E_r (MeV)	Γ (keV)	$\omega\gamma$ (keV)
10.91	2.77	218±30	$3.8^{+3.6}_{-1.7}$
10.99	2.85	310±63	$3.7^{+3.0}_{-1.7}$
11.13	2.99	210±50	$4.2^{+3.6}_{-2.7}$

Groombridge *et al.* [29] aimed at improving on the previous work by Bradfield-Smith *et al.* [28] by improving the rejection of background proton events, thus increasing the detection efficiency. This in turn allowed for studying the ^{22}Mg nucleus at lower excitation energies which are more relevant to Type-I X-ray bursts. Groombridge *et al.* identified eight states and proposed spin assignments, which are presented in Table 3.3 along with resonance parameters and resonance strengths . The resonance strengths of the identified states were used to calculate the stellar reaction rate, shown in Figure 3.2: for temperatures T ≥ 1.5 GK there is reasonable agreement with the SMOKER [27] calculations. However, the Groombridge *et al.* [29] reaction rate rapidly falls below the Hauser-Feshbach prediction at temperatures T < 1.5 GK.

Table 3.3**:** *Resonance parameters of ^{22}Mg states identified Groombridge et al. [29].*

$E_x(^{22}Mg)$ (MeV)	E_r (MeV)	J^{π}	Γ (keV)	$\omega\gamma$ (keV)
10.12±0.14	1.98±0.14	2^+ (3^-,5^-)	100± 20	$1.4^{+0.3}_{-0.2}$
10.31±0.14	2.17±0.14	2^+ (3^-,5^-)	130± 80	$10.3^{+8.6}_{-1.4}$
10.42±0.15	2.28±0.15	2^+ (1^-,3^-)	210± 100	$7.3^{+9.7}_{-1.5}$
10.55±0.14	2.41±0.14	2^+ (3^-,5^-)	160± 30	$18.8^{+2.9}_{-2.2}$
10.66±0.14	2.52±0.14	2^+ (1^-,3^-)	100± 50	$18.2^{+8.9}_{-1.9}$
10.86±0.14	2.72±0.14	0^+ (1^-)	210± 10	$45.2^{+14.6}_{-11.8}$
10.92±0.14	2.78±0.14	2^+ (1^-,3^-)	120± 20	$34.0^{+4.9}_{-3.6}$
11.01±0.14	2.87±0.14	2^+ (1^-,3^-)	100± 20	$8.1^{+2.9}_{-2.0}$

Since the direct measurements of the ^{18}Ne(α,p)^{21}Na reaction by Bradfield-Smith *et al.* [28] and Groombridge *et al.* [29] in 1999 and 2002 respectively, there have been a wide range of experiments performed with the aim to selectively populate α-unbound natural-parity states in ^{22}Mg: the knockout reaction ^{24}Mg(p,t)^{22}Mg [30–34], the transfer reactions ^{12}Mg(^{16}O,^{6}He)^{22}Mg [21], ^{25}Mg(^{3}He,^{6}He)^{22}Mg [35] and ^{24}Mg(^{4}He,^{6}He)^{22}Mg [36], the proton capture reaction ^{21}Na(p,γ)^{22}Mg [37, 38], and resonant scattering ^{21}Na(p,p)^{21}Na [39, 40] reaction have provided information on excited states in ^{22}Mg; more than 40 states have been observed above the ^{18}Ne+α threshold in ^{22}Mg, however, most of the information obtained is only on the excitation energy of the levels with little or no constraints on the spins and partial/total widths. Excited states above the ^{18}Ne + α threshold from the most recent study of ^{22}Mg [34] are listed

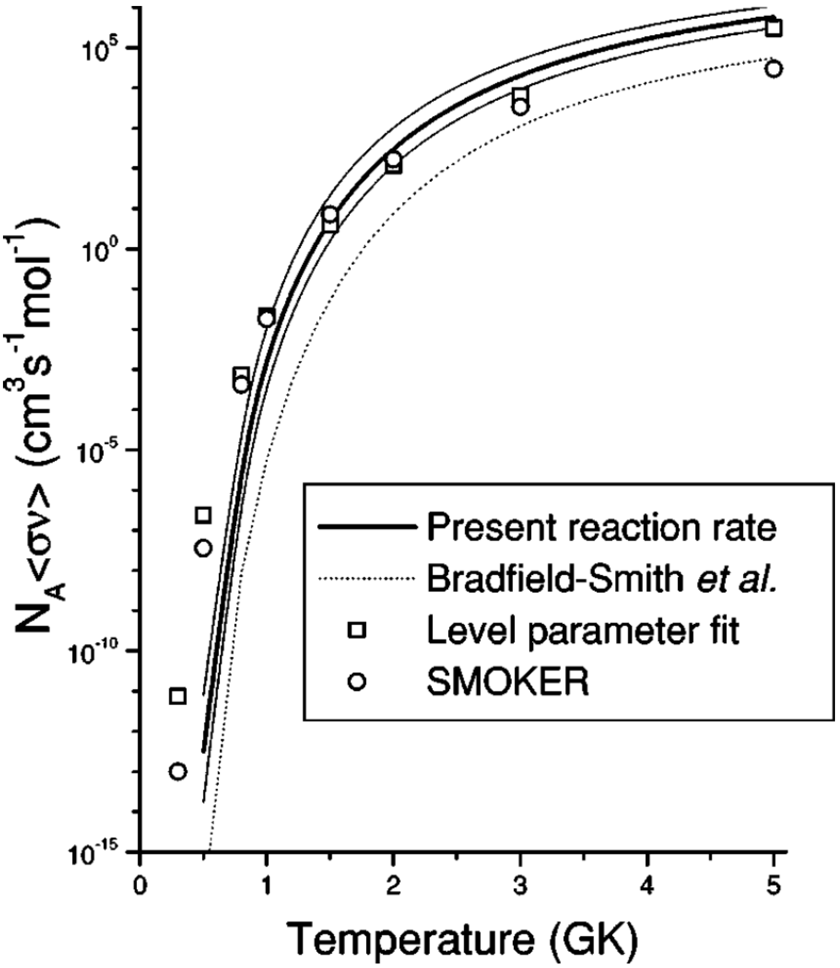

Figure 3.2: *^{18}Ne(α,p)^{21}Na reaction rates calculated by Groombridge et al. [29] (thick solid line, with thinner solid line error bands) and Bradfield-Smith et al. [28] (dashed line). Also plotted are the Hauser-Feshbach calculation of the reaction rate using the SMOKER code, and the level parameter fit refers to Görres et al. [26]. The plot is from [29].*

in Table 3.4 and illustrated in Figure 3.3. The spin and parity assignments shown are inferred from the well-known ^{22}Ne mirror nucleus.

This completes the discussion on the current state of the art from published experimental data. However there has been a recent study of the ^{18}Ne(α,p)^{21}Na reaction using the time-reverse technique, *i.e.* with a ^{21}Na beam on a solid $(CH_2)_n$ target, performed by a collaboration at the Argonne National Laboratory (ANL), but the results were never published and are only available in annual reports [41,42]. The ^{18}Ne ions from the ^{21}Na(p,α)^{18}Ne reaction were detected using a gas ionisation chamber and in coincidence with α-particles detected in silicon detectors. The results of the study are displayed in Figure 3.4; at E_{cm} = 2.5 MeV, the ANL cross section was determined to be a factor $\sim$ 50 smaller than the cross section calculated using resonance parameters of Groombridge *et al.* [29]. However, it should be noted that the excitation function of the Groombridge *et al.* [29] study drawn in Figure 3.4 is calculated as an incoherent sum of contributions from the resonances identified in [29], and do not take into account interference between resonances. It should also be noted, the cross sections measured in the ANL studies represent lower limits of the cross section since the time-reverse technique only connects the ground states of ^{21}Na and ^{18}Ne; Sinha *et al.* [42] suggest the contribution to the cross section from reactions to excited states in ^{21}Na will account for only a factor 2 increase of the cross section. If interference effects between resonances are present, then destructive interference could reduce the ^{18}Ne(α,p)^{21}Na cross section possibly leading to a better agreement between the Groombridge *et al.* excitation function and the ANL measurement. However, Γ values very different from those in [29] would be required [43].

This concludes the discussion of the state of the art from experimental data. There will now be a brief discussion on the theoretical estimates of the reaction rate and the statistical model used.

Theoretical estimates of the ^{18}Ne(α,p)^{21}Na reaction rate are provided by the Hauser-Feshbach (HF) statistical model [44,45]. A discussion on the theory of the Hauser-Feshbach formalism goes beyond the scope of this work and can be found in [46] and [47]. In the formalism, level densities in the compound nucleus may be calculated by the shell model [48], Fermi gas [49] or back-shifted Fermi gas approximations [50]. The only condition on the applicability

***Table 3.4*:** *Resonance parameters and strengths of ^{22}Mg states above the ^{18}Ne+α threshold from Matić et al. [34]. The J^{π} assignments are inferred from the well-known ^{22}Ne mirror nucleus.*

$E_x(^{22}\mathrm{Mg})$ (MeV)	E_r (MeV)	J^{π} [^{22}Ne]	Γ_{α} (eV)	$\omega\gamma$ (keV)
8.1812(16)	0.039	[2^+]	1.7×10^{-65}	8.53×10^{-65}
8.385(7)	0.243	[2^+]	2.7×10^{-18}	1.33×10^{-17}
8.5193(20)	0.377	[3^-]	7.0×10^{-15}	4.87×10^{-14}
8.574(6)	0.432	[4^+]	3.6×10^{-13}	3.26×10^{-12}
8.6572(17)	0.515	[0^+]	5.0×10^{-8}	4.97×10^{-8}
8.743(14)	0.601	[4^+]	5.7×10^{-10}	5.15×10^{-9}
8.7832(22)	0.642	[1^-]	4.0×10^{-6}	1.21×10^{-5}
8.9318(27)	0.790	[2^+]	8.3×10^{-5}	4.13×10^{-4}
9.080(7)	0.938	[1^-]	7.7×10^{-3}	2.31×10^{-2}
9.157(4)	1.015	[4^+]	9.7×10^{-5}	8.70×10^{-4}
9.318(12)	1.176	[2^+]	9.9×10^{-2}	4.97×10^{-1}
9.482(11)	1.342	[3^-]	1.8×10^{-2}	1.25×10^{-1}
9.542(9)	1.401	[2^+]	3.6×10^{-1}	1.78
9.709(19)	1.565	[0^+]	5.2×10^{1}	5.18×10^{1}
9.7516(27)	1.610	[2^+]	1.6	8.22
9.860(5)	1.718	[0^+]	2.1×10^{1}	2.07×10^{1}
10.085(13)	1.944	[2^+]	4.5×10^{1}	2.25×10^{2}
10.2715(17)	2.130	2^+	-	1.03×10^{4}[a]
10.429(13)	2.287	[4^+]	-	7.30×10^{3}[a]
10.651(13)	2.513	[3^-]	-	1.82×10^{4}[a]
10.768(13)	2.626	[2^+]	2.3×10^{3}	1.16×10^{4}
10.873(14)	2.734	[4^+]	-	4.52×10^{4}[a]
11.001(11)	2.859	[0^+]	-	8.10×10^{3}[a]
11.315(16)	3.173	[4^+]	2.0×10^{2}	1.83×10^{3}
11.499(17)	3.357	[2^+]	1.7×10^{4}	8.64×10^{4}
11.595(12)	3.455	[1^-]	2.0×10^{4}	6.11×10^{4}
11.747(17)	3.607	[0^+]	7.1×10^{4}	7.13×10^{4}
11.914(13)	3.780	[0^+]	8.8×10^{4}	8.82×10^{4}
12.003(20)	3.861	[1^-]	1.4×10^{5}	4.31×10^{5}
12.185(17)	4.050	[3^-]	3.7×10^{4}	2.60×10^{5}
12.474(26)	4.332	[2^+]	7.8×10^{4}	3.89×10^{5}
12.665(17)	4.523	[3^-]	4.9×10^{4}	3.45×10^{5}
13.010(50)	4.865	[0^+]	2.2×10^{5}	2.16×10^{5}

[a] Resonance strengths as given by Groombridge *et al.* [29].

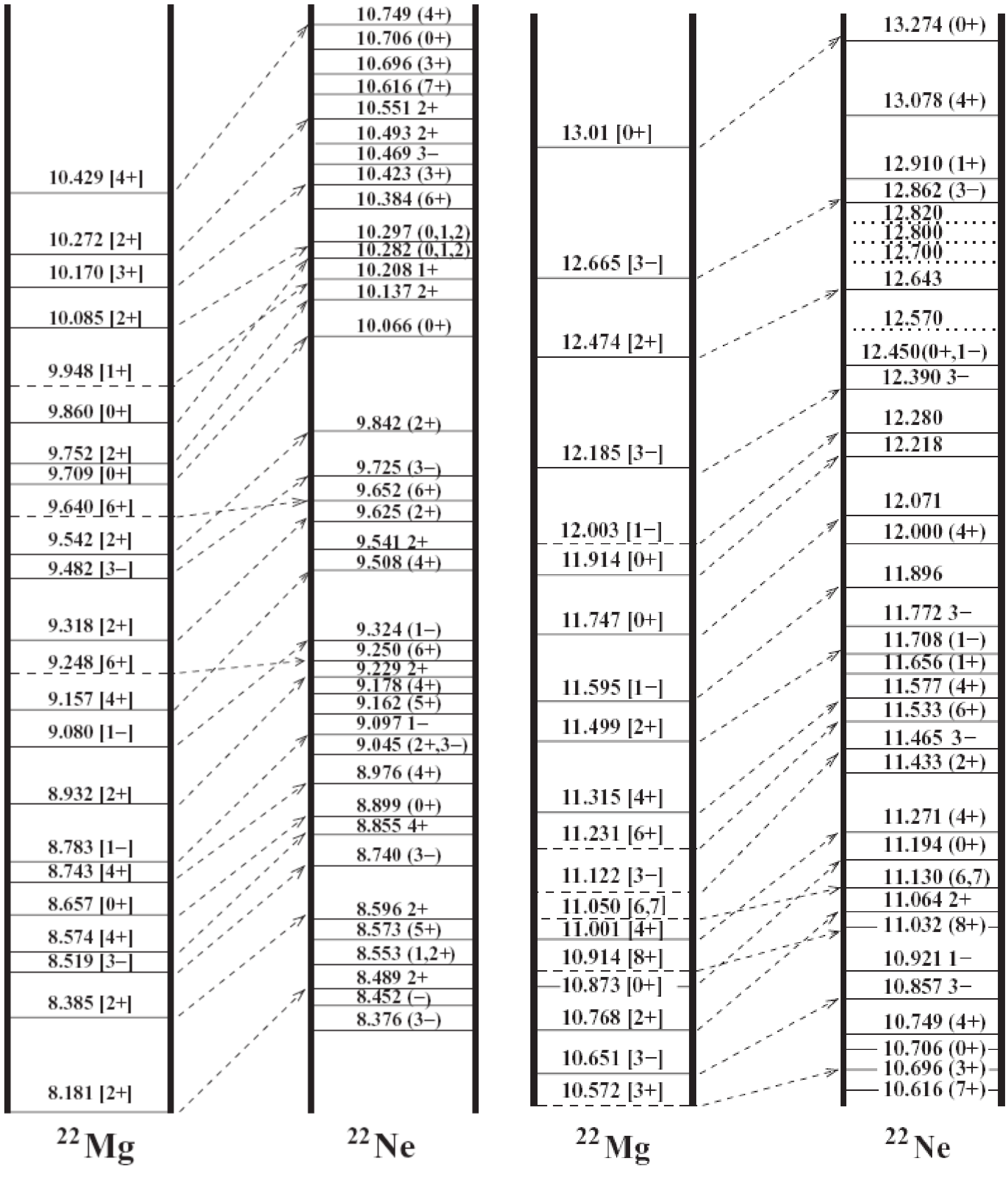

Figure 3.3: *^{22}Mg level diagrams with mirror spin assignments for levels above the ^{18}Ne+α threshold from [34]. Dashed levels represent adopted states which were not observed by Matić et al. [34].*

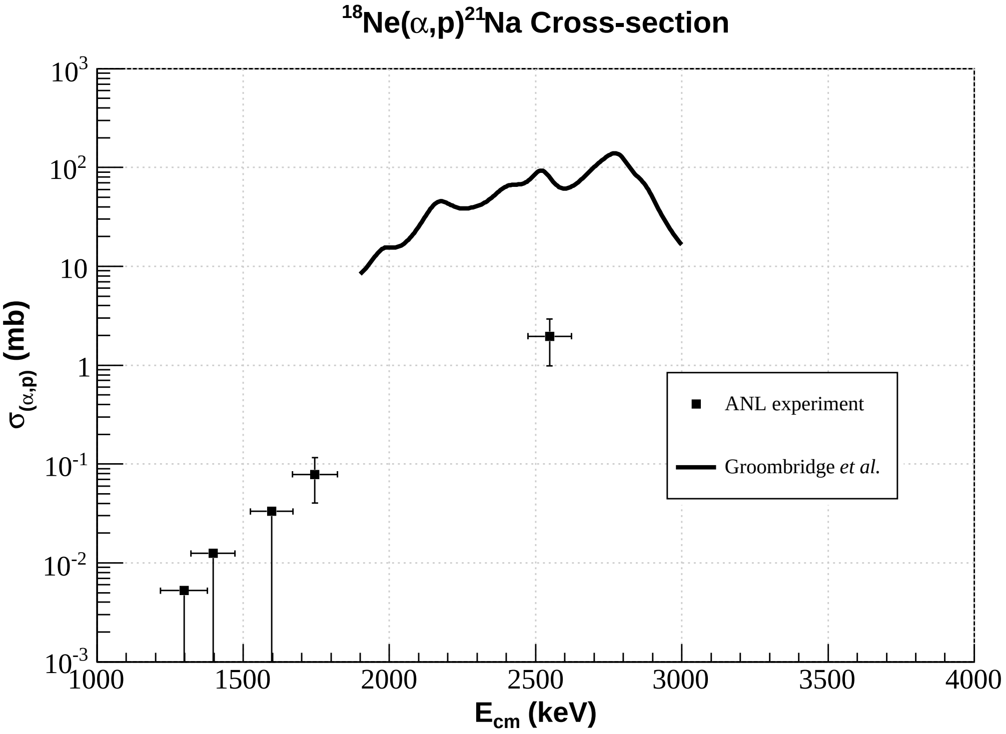

Figure 3.4: *^{18}Ne(α,p)^{21}Na cross-sections for the ANL [42] and Groombridge et al. [29] studies. The excitation function of Groombridge et al. [29] is calculated as an incoherent sum of contributions from the resonances identified in [29].*

of the statistical model is that the level density in the compound nucleus in the centre-of-mass energy region of astrophysical interest is sufficiently high so that the cross section can be described by an average over all resonances [51]; a sufficiently high level density is estimated to be between 5 - 10 MeV^{-1} [52]. At present, the spin assignments of ^{22}Mg states are inferred from the mirror ^{22}Ne nucleus. There is, therefore, an uncertainty in the level density of natural parity states in ^{22}Mg, especially in the energy range of interest $E_x(^{22}\mathrm{Mg}) \approx$ 8-11 MeV, and an uncertainty in the applicability of the HF formalism to the ^{18}Ne(α,p)^{21}Na reaction.

There are numerous HF formalism codes available; the one used in this work is the NON-SMOKER [53] code. The NON-SMOKER code is derived from the SMOKER [27] code which is used in Görres *et al.* [26], Bradfield-Smith *et al.* [28], Groombridge *et al.* [29] and Matić *et al.* [34]. The results of the SMOKER and NON-SMOKER calculations for the ^{18}Ne(α,p)^{21}Na reaction are in very strong agreement; the NON-SMOKER code was chosen for this work because access to the results is more freely available. The results of the NON-SMOKER Hauser-Feshbach cross section calculation for the ^{18}Ne(α,p)^{21}Na reaction can be found in [46, 54] and are presented in Figure 3.5; the calculations were performed assuming the level density above the ^{18}Ne+α threshold in ^{22}Mg is sufficient for the Hauser-Feshbach formalism. Web-based access to these calculations is available at [55].

In summary, the current state of the art of the ^{18}Ne(α,p)^{21}Na reaction rate is illustrated in Figure 3.6, a plot taken from [34]. In this plot, the reaction rates calculated by by Matić *et al.* [34], Chen *et al.* [21], Bradfield-Smith *et al.* [28], Groombridge *et al.* [29], Görres *et al.* [26] and the SMOKER Hauser-Feshbach calculation are presented: for temperatures T = 1-2 GK there is a fair agreement between all reaction rate calculations, except for the Bradfield-Smith *et al.* study; but for temperatures T > 2 GK and, more importantly, at astrophysical temperatures T < 1 GK there are discrepancies between all the studies; and in particular for T < 0.8 GK, which is the temperature region of interest for HCNO breakout leading to thermonuclear runaway, by many orders of magnitude between the Groombridge *et al.* and the Matić *et al.*, Chen *et al.*, Görres *et al.* and Hauser-Feshbach studies.

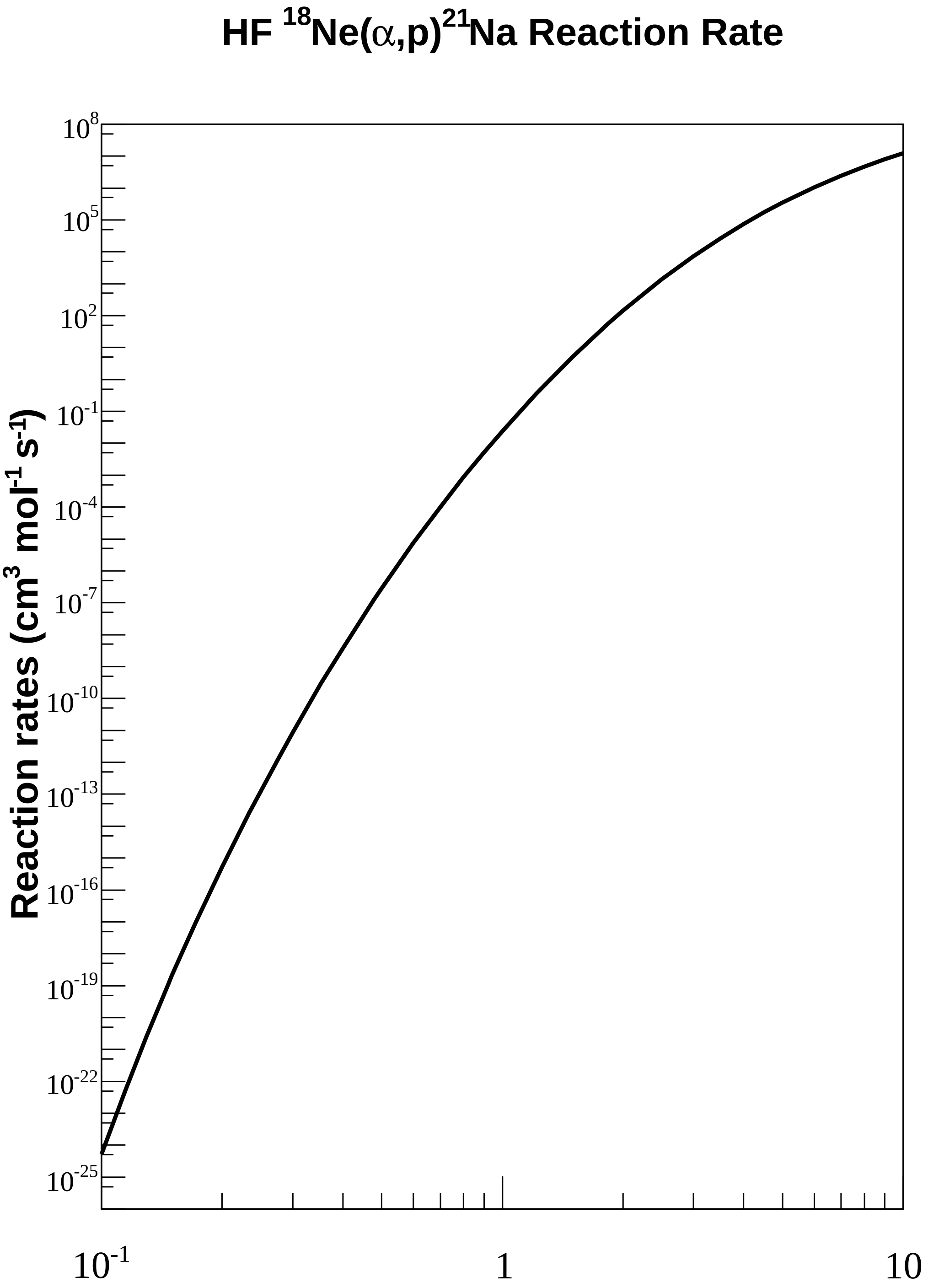

Figure 3.5: *Hauser-Feshbach* ^{18}*Ne(*α*,p)*^{21}*Na reaction rate calculated by the NON-SMOKER code [46, 54].*

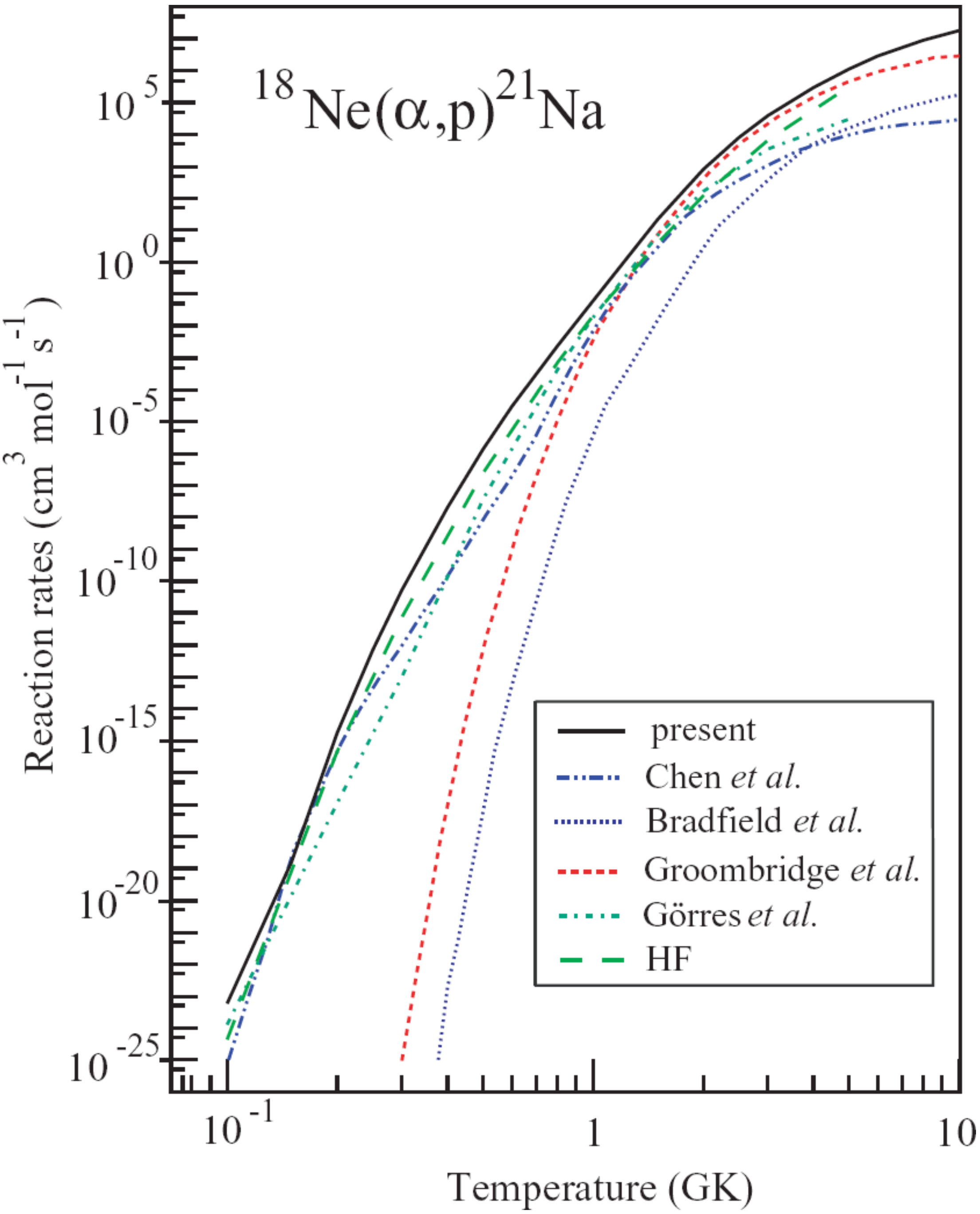

Figure 3.6: *^{18}Ne(α,p)^{21}Na reaction rates calculated as a function of temperature for 5 previous studies [21,26,28,29,34]. 'Present' refers to the work of Matić et al. [34]. The Hauser-Feshbach calculation has been taken from [26]. Figure taken from [34].*

The aim of this work is to perform a time-reverse measurement of the ^{18}Ne(α,p)^{21}Na cross section at energies lower than any previous measurement and more appropriate for an X-ray burst; test the effectiveness of the Hauser-Feshbach approximation of the reaction rate provided by the NON-SMOKER code; and perform a comparison with the previous ANL time-reverse measurement.

Chapter 4

Methodology

The aim of this work was the time-reverse measurement of the ^{18}Ne(α,p)^{21}Na reaction cross section. This was achieved by using a radioactive ion beam on a solid $(CH_2)_n$ target, and coincident detection of the reaction products by silicon strip detectors. This chapter will discuss the time-reverse method and how the direct and time-reverse cross sections are related radioactive ion beam production; particle identification techniques used in this work; and the methodology of calculating the ^{21}Na(p,α)^{18}Ne cross section from the measured ^{21}Na(p,α)^{18}Ne reaction yield.

4.1 The Time-Reverse Method

For the reaction A(a,b)B, where A and a denote the target and projectile, respectively, and B and b denote the reaction products, the cross section of the A(a,b)B reaction is related to that of the reverse reaction, B(b,a)A, since both forward and reverse processes are invariant under time-reversal. In other words, time is not a component of the equations describing both processes. It can be shown that [10]:

$$\frac{k_{Aa}^2 \sigma_{Aa\rightarrow Bb}}{(1+\delta_{Aa})} = \frac{k_{Bb}^2 \sigma_{Bb\rightarrow Aa}}{(1+\delta_{Bb})} \tag{4.1}$$

where k is the wave number of the free particle, $\sigma_{Aa\rightarrow Bb}$ and $\sigma_{Bb\rightarrow Aa}$ are the cross sections for the forward and time reverse directions, and the Kronecker delta, δ_{ij}, terms take into account the factor of two increase on the cross section if the nuclei in the entrance channel are identical. Equation (4.1) is known as the *reciprocity theorem* and is true for differential and total cross sections. For particles with spin, Equation (4.1) is modified such that:

$$\frac{k_{Aa}^2(2j_A+1)(2j_a+1)\sigma_{Aa\to Bb}}{(1+\delta_{Aa})} = \frac{k_{Bb}^2(2j_B+1)(2j_b+1)\sigma_{Bb\to Aa}}{(1+\delta_{Bb})} \tag{4.2}$$

and rearranging for $\sigma_{Aa\to Bb}/\sigma_{Bb\to Aa}$:

$$\frac{\sigma_{Bb\to Aa}}{\sigma_{Aa\to Bb}} = \frac{(2j_A+1)(2j_a+1)k_{Aa}^2(1+\delta_{Bb})}{(2j_B+1)(2j_b+1)k_{Bb}^2(1+\delta_{Aa})} \tag{4.3}$$

and since the wave number $k = mv/\hbar$, Equation (4.3) can be rewritten for the ^{18}Ne(α,p)^{21}Na reaction:

$$\frac{\sigma_{\alpha^{18}Ne\to p^{21}Na}}{\sigma_{p^{21}Na\to\alpha^{18}Ne}} = \frac{m_p m_{^{21}Na} E_{p^{21}Na}(2j_p+1)(2j_{^{21}Na}+1)}{m_\alpha m_{^{18}Ne} E_{\alpha^{18}Ne}(2j_\alpha+1)(2j_{^{18}Ne}+1)} \tag{4.4}$$

where $E_{\alpha^{18}Ne}$ and $E_{p^{21}Na}$ are the centre-of-mass energies for the direct and inverse reactions respectively, and m_i and j_i the masses and nuclear spins of the interacting particles respectively. Hence, a value for the ^{18}Ne(α,p)^{21}Na cross section at $E_{\alpha^{18}Ne}$ can be extracted by a measurement of the ^{21}Na(p,α)^{18}Ne cross section at $E_{p^{21}Na} = E_{\alpha^{18}Ne}$ + Q, where Q is the Q-value of the ^{18}Ne(α,p)^{21}Na reaction (Q = 2.6373 MeV).

The primary limitation of using the time reverse method is that excited states in the ^{21}Na+p system, which would otherwise be populated in the forward ^{18}Ne(α,p)^{21}Na direction and thus be important for the astrophysical scenario, cannot be accessed. As such, the cross section extracted for the ^{18}Ne(α,p)^{21}Na direction is a lower limit and refers to ground-state to ground-state transitions only.

An important consideration when using the time-reverse technique in this work, is the lack of restriction on states in ^{22}Mg through which the ^{21}Na(p,α)^{18}Ne reaction may proceed; for the ^{18}Ne(α,p)^{21}Na direction, the particles in the entrance channel are spin-less and therefore, conservation of angular momentum and parity restrict access to states in ^{22}Mg of natural parity. However, for the ^{21}Na(p,α)^{18}Ne direction, the ^{21}Na and ^{1}H ions have ground-state spins of $J^\pi = \frac{3}{2}^+$ and $\frac{1}{2}^+$ respectively; both natural and unnatural parity states in ^{22}Mg are accessible. However, by kinematically selecting events which leave the ^{18}Ne and ^{4}He ions in their ground states, one can make sure that only natural parity states have been populated through the ^{21}Na(p,α)^{18}Ne direction.

^{21}Na has a half-life of 22.5s so a measurement of the ^{21}Na(p,α)^{18}Ne reaction requires a ^{21}Na beam on a proton target. A discussion of the method used to produce and accelerate a radioactive ^{21}Na beam will be given in the following section.

4.2 Radioactive Ion Beam (RIB) Production

Proton- and α-particle induced reactions involving unstable nuclei offer an additional experimental challenge given the short lived nature of the unstable nuclei. If the half-life of the unstable isotope exceeds a few days, it is feasible to manufacture a radioactive target and use a beam of protons/α-particles to induce the reaction of interest. However, if the unstable isotope has a half-life of a day or less, then manufacturing a radioactive target is not logistically feasible since the target will β-decay before any meaningful experiment can be performed. In this case, the reaction of interest can only be studied using a beam of the unstable isotope. For reactions involving protons or alpha particles as a target, the study must therefore be performed in inverse kinematics. A discussion of various techniques used for producing and accelerating a radioactive beam can be found in [10]. In this work the isotope separator online technique was used to produce a radioactive beam.

The Isotope Separator OnLine (ISOL) technique is a two stage process, schematically shown in Figure 4.1. The first stage involves a beam of stable nuclei, commonly protons, bombarding a thick target. Nuclear reactions occur on the target and the products are allowed to diffuse out through a transfer tube and into an ion source. In the ion source, the reaction products are ionised and extracted, before being separated based on their atomic-mass/charge (A/q) ratio. Using a post accelerator, the selected radioactive ions are then accelerated to the desired energy and delivered to the experimental chamber. ISOL beam facilities are available, for example, at Oak Ridge National Laboratory, CERN and TRIUMF. Further details on the production at TRIUMF of the ^{21}Na beam used for this work are given in Chapter 5.

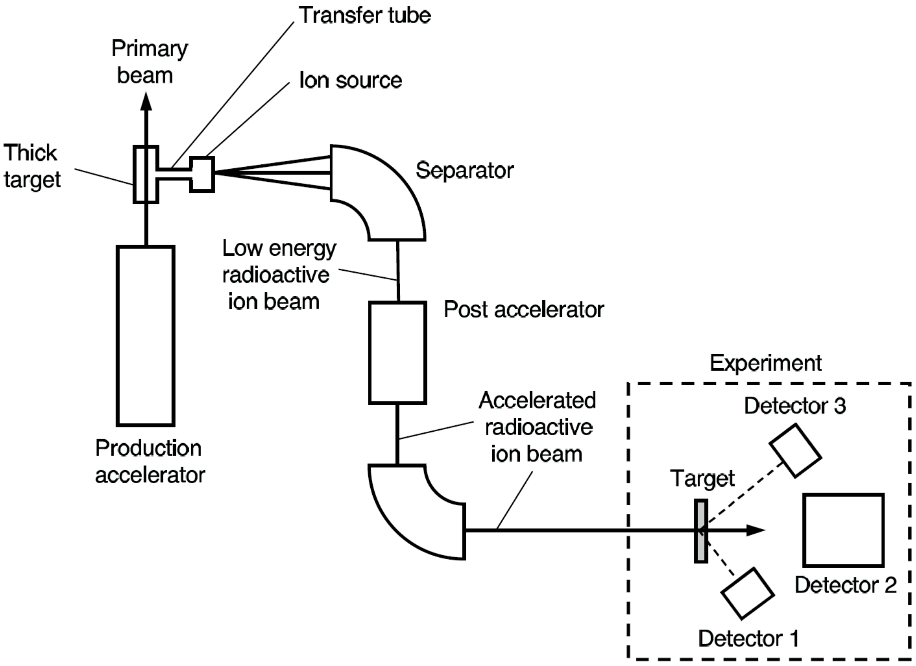

Figure 4.1: *Schematic view of the basic components in an ISOL facility. A primary beam of stable nuclei is accelerated onto a thick target where nuclear reactions occur and the products are allowed to diffuse out into the ion source. The reaction products are separated and the isotope of interest selected, accelerated and delivered to the experimental chamber. Diagram taken from [10].*

4.3 Particle Detection & Identification

For the detection of charged particles, silicon semiconductors are most commonly used. The interaction of a charged particle within a semiconductor results in the formation of electron-hole pairs. If an electric field is applied to the semiconductor, the electron-hole pairs drift, creating an electric current which, if connected to an external circuit, provides the basis for measuring the charged particle interaction. A discussion of semiconductor detectors may be found in [56].

For charged particle identification, two primary techniques have been employed: ΔE-E telescopes and time-of-flight. These techniques will be briefly discussed in the following subsections.

4.3.1 ΔE-E Telescope

If a thin detector is placed in the path of a charged particle, such that the thickness of the detector is less than the range of the particle, the energy deposited by the charged particle is charge dependent and can be used to identify the particle. The thin detector is commonly referred to as a Δ*E* detector and is used in conjunction with a second much thicker detector in which the particle is stopped. This arrangement is illustrated in Figure 4.2 and is known as a Δ*E-E* or *particle identifier* telescope.

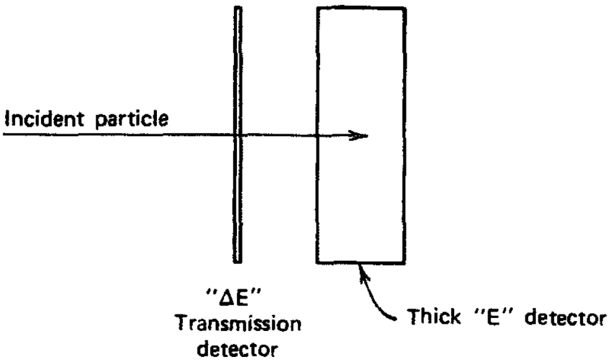

Figure 4.2: *Typical ΔE-E telescope arrangement [56].*

The approach used here to identify particles from the ΔE-E telescope is described by [57,58] and is based on the observation that the range of a charged particle in a medium is related to the energy of the particle by a power-law approximation, such that:

$$R(E) \propto aE^{b} \tag{4.5}$$

where a and b are constants for a given particle, with a roughly proportional to $1/mq_{\text{eff}}^{2}$ (where q_{eff} is the rms charge state of the moving ion since it may or may not be fully stripped of atomic electrons, *i.e.* $q_{\text{eff}} \leq Z$) and b of the order of 1.73 for protons and 1.65 for carbon ions. If an incident particle passes through the first detector of thickness Δx, depositing energy ΔE, and then into a thicker second detector where all the particle's remaining energy, E, is deposited then

$$\Delta x \propto R(E + \Delta E) - R(E) \tag{4.6}$$

or, substituting for Equation 4.5,

$$\frac{\Delta x}{a} \propto (E + \Delta E)^{b} - E^{b} \tag{4.7}$$

As a is approximately proportional to $1/mq_{\text{eff}}^{2}$, the left side of Equation 4.7 is therefore roughly proportional to mq_{eff}^{2}; and, from here on, the quantity $\Delta x/a$ will be referred to as the *PI* number. Provided a suitable value for b is used, the PI number is characteristic of particle type and independent of particle energy. A particle identification spectrum for all particles entering a ΔE-E telescope, such as the one shown in Figure 4.3, can be used to separate in mq_{eff}^{2} the particles in the telescope and select those of interest.

This technique has been applied for ^{4}He and ^{18}Ne identification as described in the data analysis (see Chapter 6).

4.3.2 Time-of-flight

Stated by Goulding *et al.* [57], the principle of time-of-flight identification is to determine the velocity of a particle and hence the ratio *E/m*. Thus, if a separate measurement of particle energy, E, is made, the mass, m, of the particle can be determined [57]:

$$m = 2E\frac{t^{2}}{d^{2}} \tag{4.8}$$

where t is the time-of-flight, and d is the distance over which the particle travels.

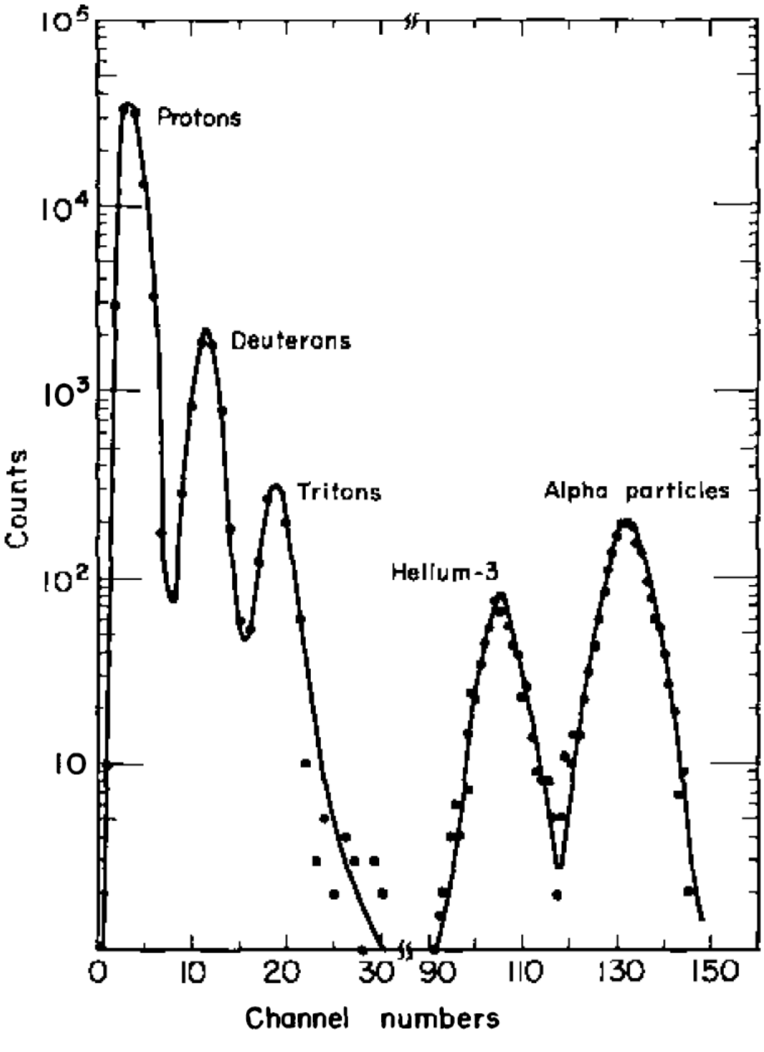

Figure 4.3: *Example particle identification spectrum using a silicon ΔE-E telescope and the range power law algorithm (Equation 4.7). Taken from [57].*

Another use of time-of-flight, and the one used in this work, is the selection of events between two detectors based on the difference of their time-of-flight. For the two-body reaction X(*a*,*b*)Y, if reaction product Y, of mass m_Y and energy E_Y, is detected in detector *1* a distance d_1 from the target, and reaction product b, of mass m_b and energy E_b, is detected in detector *2* a distance d_2 from the target, then the time difference between the two reaction products arriving at their detectors is given by:

$$\Delta t \;=\; t_Y - t_b \;=\; \sqrt{\frac{1}{2}}\left[d_1\sqrt{\frac{m_Y}{E_Y}} - d_2\sqrt{\frac{m_b}{E_b}}\right] \tag{4.9}$$

where t_Y and t_b are the time-of-flight of reaction products Y and b respectively. Events from the reaction X(*a*,*b*)Y can be identified by selecting event pairs across the two detectors with a time-of-flight difference given by Equation 4.9.

4.4 Yields and Cross Sections for Charged-Particle-Induced Reactions

Using the particle identification methods discussed in the previous section, the products from the reaction of interest can be selected; providing a measurement of the reaction yield. The reaction yield can then be used to determine the reaction cross section. This section will provide a brief discussion on how the reaction yield may used to determine the reaction cross section.

The yield of a reaction is effectively the ratio of the total number of nuclear reactions, N_R, that occurred to the total number of incident beam particles, N_b. A target of thickness x can be divided into thin slices, each of thickness Δx_i, such that for an incident beam, of energy E_0, the cross section, σ_i, and stopping power, ϵ_i, are constant over each slice. The yield, ΔY_i, of nuclear reactions from an individual slice is given by:

$$\Delta Y_i \;=\; \frac{N_{R,i}}{N_b} \;=\; \sigma_i \frac{N_{t,i}}{A} \;=\; \sigma_i N_i \Delta x_i \tag{4.10}$$

where $N_{t,i}/A$ is the number of target nuclei per unit area and N_i the number of target nuclei per unit volume in the target slice.

The total yield, Y, over the entire target is given by integrating Equation 4.10 over all target slices:

$$\begin{aligned} Y(E_0) &= \frac{N_R}{N_b} = \int \sigma(x)N(x)\,dx = \int \sigma(x)N(x)\,dx\,\frac{dE(x)}{dx}\,\frac{dx}{dE(x)} \\ &= \int_{E_0-\Delta E}^{E_0} \frac{\sigma(E)}{\epsilon(E)}\,dE \end{aligned} \tag{4.11}$$

If the reaction cross section is approximately constant over the entire target thickness, implying the reactions occur equally over the target thickness, and if the stopping power, ϵ, is also approximately constant over the target, the target is referred to as *thin* and the yield is then given by:

$$Y(E_0) = \frac{\sigma(E_{\text{eff}})}{\sigma(E_0)} \int_{E_0-\Delta E}^{E_0} dE = \frac{\Delta E(E_0)}{\epsilon(E_0)}\sigma(E_{\text{eff}}) = n\sigma(E_{\text{eff}}) \tag{4.12}$$

where $n = N_t/A$, and E_{eff} is the mean effective energy such that $E_{\text{eff}} = E_0 - \Delta E/2$ (*i.e.* beam energy at mid-target). For differential cross sections, the following equation holds:

$$\left[\frac{dY(E_0)}{d\Omega}\right]_\theta = \frac{\Delta E(E_0)}{\epsilon(E_0)}\left[\frac{d\sigma(E_{\text{eff}})}{d\Omega}\right]_\theta = n\left[\frac{d\sigma(E_{\text{eff}})}{d\Omega}\right]_\theta \tag{4.13}$$

If the cross section has a weak energy dependence, *i.e.* is moderately varying, but the stopping power remains constant over the target, the effective beam energy must be modified to reflect the fact that reactions still occur over the entire target thickness, but the number of reactions at different target depths is no longer constant. If the cross section is approximated as varying linearly over the target, with $\sigma_1 = \sigma(E_0)$ and $\sigma_2 = \sigma(E_0 - \Delta E)$, then the effective beam energy is given by [24]:

$$E_{\text{eff}} = E_0 - \Delta E + \Delta E\left[-\frac{\sigma_2}{\sigma_1 - \sigma_2} + \sqrt{\frac{\sigma_1^2 + \sigma_2^2}{2(\sigma_1 - \sigma_2)^2}}\right] \tag{4.14}$$

Chapter 5

Experimental Investigation

The experiment was performed using the TRIUMF UK Detector Array (TUDA) at the ISAC-II facility at TRIUMF, Vancouver, Canada. TRIUMF is the TRI-Universities Meson Facility and is Canada's national physics laboratory for particle and nuclear physics research. The laboratory uses, to date, the world's largest sector-focusing cyclotron which accelerates H^- ions up to 500 MeV. The cyclotron is used for the production of Radioactive Ion Beams (RIBs) with the ISAC (Isotope Separator and Accelerator) facility. TRIUMF was chosen for the time-reverse ^{21}Na(p,α)^{18}Ne cross section measurement as it has the capabilities to produce the highest intensity ^{21}Na beams compared to any other operational RIB facilities. The objective of the experiment was the investigation of the ^{18}Ne(α,p)^{21}Na reaction at energies of astrophysical interest by means of the time-reversal approach in inverse kinematics, using a ^{21}Na RIB on to a $(CH_2)_n$ target. The ^{21}Na(p,α)^{18}Ne reaction was studied at six centre-of-mass energies in the range E_{cm} = 3.6 - 5.3 MeV (E_{cm}^{direct} = 1.2 - 2.6 MeV).

This chapter details the production, transportation and acceleration of ^{21}Na and ^{21}Ne beams (the latter was used for calibration purposes - see later); a description of the TUDA scattering chamber and detectors; and a description of the data acquisition system used for the experiment. An outline of the experimental arrangement and procedure for the ^{21}Na(p,α)^{18}Ne cross section measurements is also provided.

5.1 The ISAC facilities at TRIUMF

The ISAC facility post-accelerates radioactive and stable beams. There are two operational ISAC facilities at TRIUMF: ISAC-I, which is capable of accelerating A<30 nuclei to 1.5 MeV/A; and the recently commissioned ISAC-II facility, which will eventually be capable of accelerating A<150 nuclei to 6.5 MeV/A. ISAC-I consists of six separate sections: beam production, Low-Energy Beam Transport (LEBT), Radio Frequency Quadrupole (RFQ) acceleration, Medium-Energy Beam Transport (MEBT), Drift-Tube Linac (DTL) linear accelerator and High-Energy Beam Transport (HEBT). ISAC-II consists of seven sections: beam production, LEBT, RFQ, MEBT, DTL, Superconducting Linac linear accelerator and High-Energy Beam Transport (SEBT). A layout of the TRIUMF complex is shown in Figure 5.1 and Figure 5.2.

5.1.1 RIB Production

The production of radioactive ion beams at TRIUMF is through the ISOL technique discussed in Chapter 4. The main cyclotron accelerates H^- ions, with energies of up to 500 MeV and intensities up to 100 μA, along beam line BL2A onto one of two thick targets (1.8 cm in diameter and up to 19 cm long [61]) situated beneath ISAC-I. The targets are made from Silicon Carbide, Tantalum or Niobium depending on the nuclear species required, and are cooled or heated depending on the intensity of H^- beam used; for low intensity beams the target is externally heated, whilst the target is water cooled for high intensity beams. For the production of ^{21}Na, a 500 MeV H^- beam was used with a current of up to 15 μA on a water cooled composite Silicon Carbide target. The resulting spallation reactions produce a variety of radioactive and stable isotopes. The isotopes diffuse out of the target and then must be ionised so that they may be separated and the isotope of interest isolated. Elements with low electron ionisation potentials ($\approx$5 eV) are ionised using a surface and/or laser ion source, whilst elements with larger electron ionisation potentials (>5 eV) are ionised using a Forced Electron Beam Induced Arc Discharge (FEBIAD) source. Sodium has a low electron ionisation potential (the first ionisation potential is 5.1391 eV [62]) so the spallation products from the target were extracted and ionised using the surface ion source. Following extraction, the

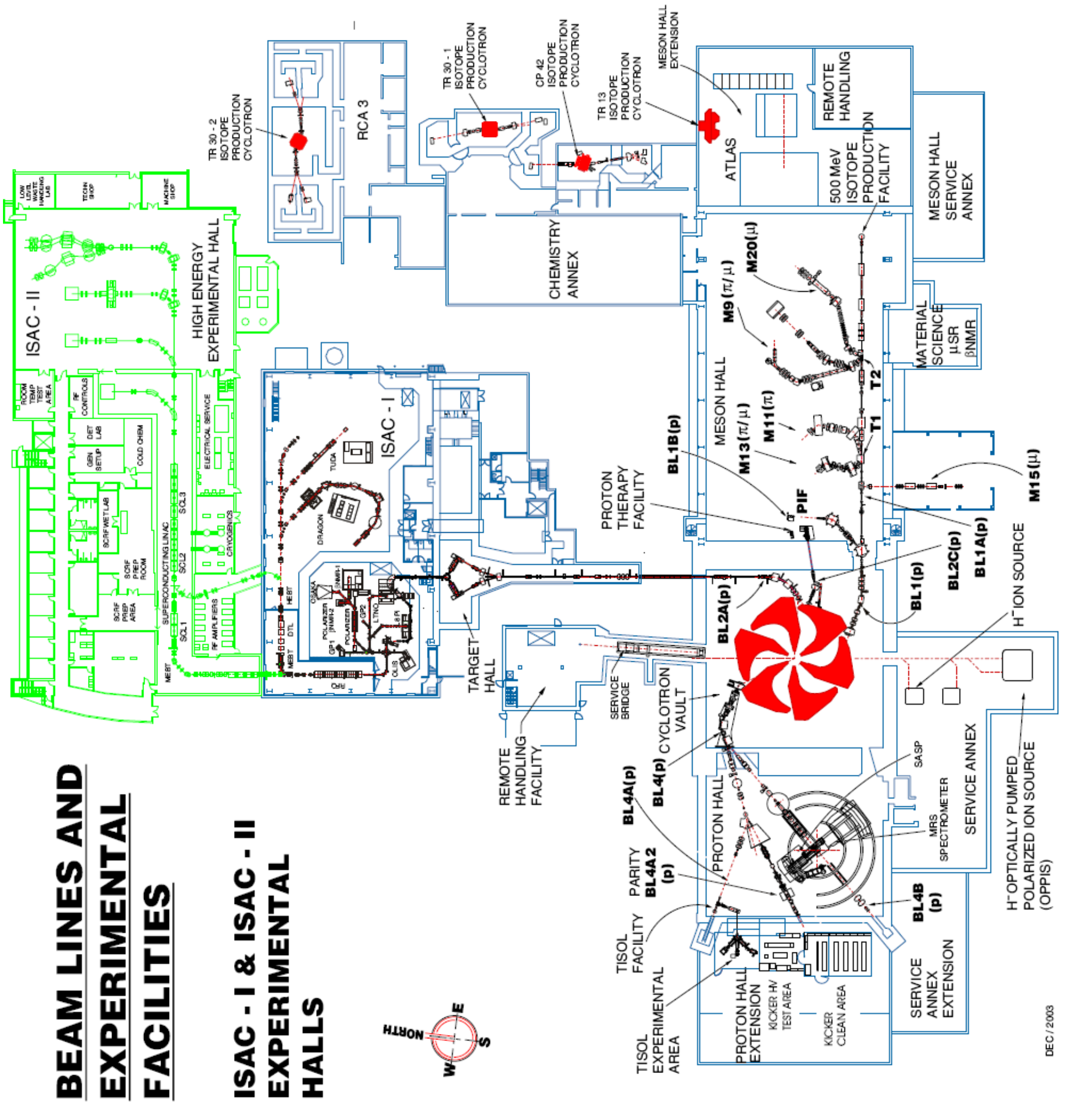

Figure 5.1: *Schematic layout of the TRIUMF complex [59]. The main cyclotron, shown in the cyclotron vault, provides up to 500 MeV H^- beams to both ISAC-I and ISAC-II and other facilities around the site. The ISAC-I and ISAC-II experimental halls are shown and the various beam delivery stations identified. The TUDA scattering chamber (shown at ISAC-I in this layout) can be moved between ISAC-I and ISAC-II.*

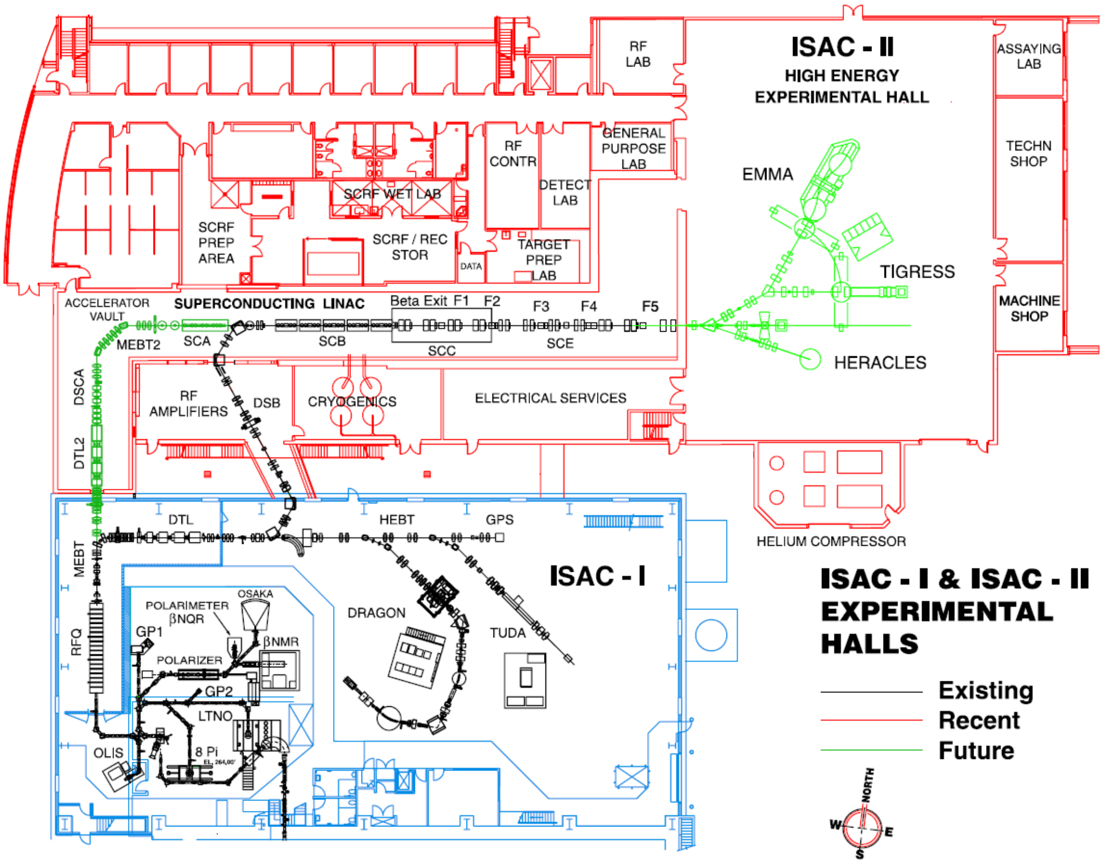

Figure 5.2: *Updated schematic layout of the ISAC-I and ISAC-II facilities, indicating in more detail the various transport sections of the beam lines [60]. TUDA can be used at either in ISAC-I (at the position shown) or upstream of Heracles in ISAC II.*

ions are low-energy accelerated into a mass separator where the radioactive species of interest are selected. The purity of 1^+ ^{21}Na at TRIUMF is 100%.

5.1.2 Stable Beam Production

For the production of a stable ^{21}Ne ion beam, used for setup and calibration purposes, an off-line ion source (OLIS) was used. The OLIS terminal consists of a microwave ion source, surface ion source and a hybrid surface-arc discharge source, all connected to an electrostatic switch [63]. The microwave ion source is the primary ion source used for the production of stable beams at TRIUMF; the 1^+ ^{21}Ne ions were produced by injecting ^{21}Ne gas into the microwave ion source. OLIS delivers the stable beam at a cross-junction (shown in Figure 5.2) after the mass separator used for radioactive isotope separation. This enables delivery of either stable or radioactive beams to ISAC-I or ISAC-II.

5.1.3 Ion Beam Transportation and Acceleration

After the beam species has been selected, the ions are transported into the low-energy transport (LEBT) section of the beam line. In the LEBT section, the beam is pre-bunched by a four-harmonic sawtooth electrostatic pre-buncher, introducing an 86 ns bunch spacing into the beam [64]. Following the pre-buncher, the beam is transported into the RFQ, which accelerates ions with $3 \leq A/Q \leq 30$ to energies from 2 keV/u to 150 keV/u [60].

After the RFQ is the MEBT section, where the beam is chopped to remove satellite peaks that are not 86 ns apart and ionised further by a thin Carbon foil to meet the $2 \leq A/Q \leq 6$ acceptance ratio of the DTL. As the beam travels round the corner of the MEBT line, the ions with the most probable charge state are selected. For our experiment, the 5^+ charge state was used for the ^{21}Na and ^{21}Ne beams. The DTL accelerates the beam to energies up to 1.5 MeV/A. For TUDA experiments at ISAC-I the beam enters the HEBT section where several quadrupoles and rebunchers maintain the time structure and focus of the beam, and deliver the beam to the experimental station. For experiments at ISAC-II, the beam is transported from the DTL through an ‘S’ shaped beam line to the Superconducting LINAC. The LINAC has a $2 \leq A/Q \leq 7$ acceptance ratio and currently accelerates up to 6.5 MeV/A. Following the LINAC is the SEBT section where quadrupoles and rebunchers maintain the time structure and focus of the beam; the beam is then delivered to TUDA or other experimental stations at ISAC-II.

5.1.4 Beam Tuning

Tuning of the accelerators and beam lines is performed using a high intensity stable pilot beam from the OLIS terminal. The stable beam species is chosen to have the same A/Q ratio as the RIB required. The tuning is based on transmission of the beam through the various beam line sections to the experimental station and is performed for each beam energy that the experiment will run at. Once the tuned settings are acquired they are saved and it is then straightforward to switch between stable and radioactive species. For this experiment a ^{21}Ne pilot beam was used. The tuning at each energy occurred in two stages: first a 10 mm aperture was placed at the target position within TUDA and the beam tuned until 100% transmission was obtained through the aperture. The second stage of tuning used the settings from the first stage and tuned the beam until there was at least 80% transmission through a 3 mm aperture placed at the TUDA target position. Throughout the tuning procedure, a Zinc-Sulphide target was placed in the target position and the beam spot examined using a CCTV camera, until a centrally aligned and symmetric beam spot is achieved.

5.2 The TUDA Scattering Chamber

The TUDA device is a highly customisable scattering chamber and instrumentation rack. The scattering chamber, shown in Figure 5.3, comprises two cylindrical sections joined either side of a rectangular section and is positioned co-axially to the beam line.

The central rectangular section contains the target ladder which is fixed on one of two calibrated variable linear translators. Either solid or gaseous targets can be mounted within the TUDA chamber; there are up to ten positions on the target ladder for solid targets, and gas cells can be mounted for reactions involving gaseous targets. On the top of the rectangular section are electrical feed-throughs for diagnostic instruments. The panels on either side of the

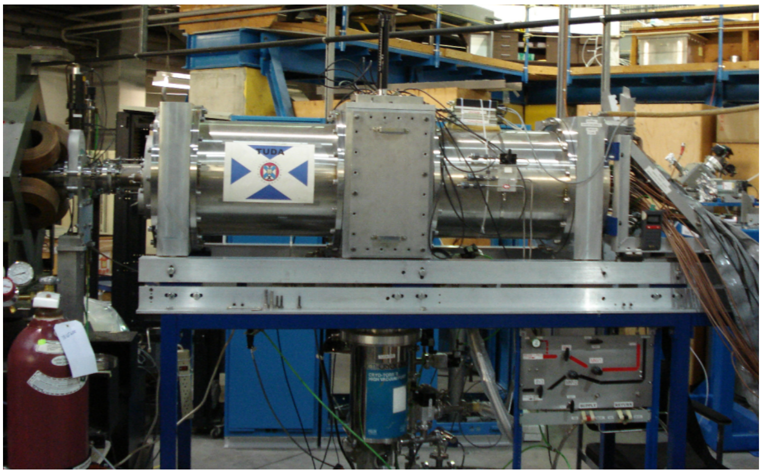

Figure 5.3: *Photograph of the TUDA scattering chamber.*

section can be removed for easy access to the instruments, and there are two ports on the underside of the section through which the vacuum system is connected. The vacuum system comprises an oil free scroll-pump, a turbo-pump and a cryo-pump and is intended to operate at 5x10^{-6} mbar.

Located at the entrance of the TUDA chamber, immediately after the last quadrupole, is a collimator assembly. The collimator diameter can be varied depending on the focus of the beam between the quadrupole and target position; for our experiment, a 15 mm diameter Tantalum collimator was used. The detector assemblies are mounted perpendicular to the beam line at varying distances upstream and downstream of the target. The assemblies are mounted on four support rods that are permanently fixed in position at the rear flange of the scattering chamber. To mount the assemblies, the rear flange is withdrawn from the chamber providing access to the four supporting rods, as shown in Figure 5.4. In addition to the detector assemblies, an array of collimators and 4-vane diagnostic instruments are mounted on the supporting rods. Positioned upstream of the target and any detector assemblies is a 10 mm anti-scattering collimator to provide additional protection, in conjunction with the main collimator, of the target and detectors from scattered primary beam. Two 4-vane monitors are used for beam diagnostics: one is placed immediately after the upstream anti-scattering collimator and the second is positioned immediately before the rear flange of the scattering chamber. A beam dump Faraday cup is mounted on the rear flange and used for beam

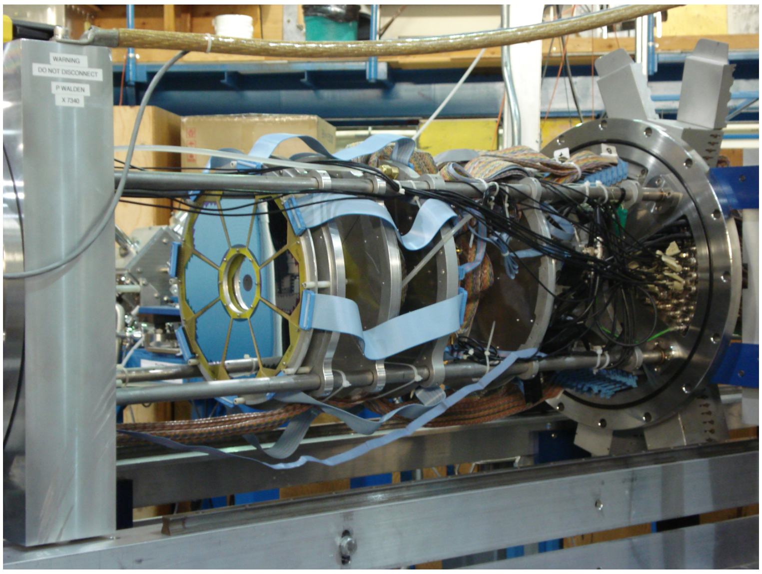

Figure 5.4: *Photograph of the four supporting rods withdrawn from the TUDA scattering chamber for mounting of detector assemblies. Photo courtesy of C. Beer.*

intensity measurements and beam tuning during an experimental run.

5.2.1 Segmented Silicon Detector Arrays

Segmented silicon detectors are typically used in the TUDA facility for the detection of charged particles. The model of detectors used depends entirely on the reaction of interest and type of measurement to be performed. For the ^{21}Na(p,α)^{18}Ne measurement detectors with high angular resolution, in both θ and ϕ directions, were an important consideration for particle identification. Another consideration was to obtain detectors with appropriate thicknesses for the ΔE-E technique to work. This is particularly important for the heavy ^{18}Ne ions which will lose a higher proportion of their energy in the ΔE detector and thicknesses must be chosen such that the heavy ions are not stopped in the ΔE detector. The detectors used in the experiment were MSL type S2 (Figure 5.5(a)), MSL type QQQ/2 (Figure 5.5(b)) and MSL type QQQ/1 (Figure 5.5(c)) detectors, all manufactured by Micron Semiconductor Ltd. [65].

The MSL type S2 detector is a Double Sided Silicon Strip Detector (DSSSD), consisting of 48 annular strips on the front p$^+$n junction side of the detector (lower image in Figure 5.5(a)) and 16 azimuthal sectors on the rear n$^+$n ohmic side (upper image of Figure 5.5(a)). The detector is fabricated using 4-inch wafer technology and uses aluminium contacts to both the front strips and rear segments for bias and output signals. The type S2 detector is supplied by MSL with nominal thicknesses of 65, 140, 300, 500 and 1000 μm.

The MSL type QQQ/2 (or 'CD') detector is a DSSSD consisting of 16 annular front $p^{+}n$ junction strips (left quadrants in Figure 5.5(b)) and 24 azimuthal rear $n^{+}n$ ohmic sectors (right quadrants in Figure 5.5(b)). The detectors are supplied as quadrants and are assembled as shown in Figure 5.5(b). Similar to the type S2, the QQQ/2 is fabricated using 3-inch wafer technology and uses aluminium contacts to both front and rear strips. Nominal thicknesses of 35 to 1000 μm are supplied by MSL.

The MSL type QQQ/1 (or 'PAD') detector is a Single Sided Silicon Detector (SSSD) and is commonly used in conjunction with the QQQ/2 detector array in a ΔE-E arrangement. A PAD quadrant is a single element of silicon so cannot provide any angular information on an incident charged particle, but when used in conjunction with a CD detector, the angular information can be extracted from the CD detector. Like the QQQ/2, the QQQ/1 is supplied as a quadrant and is assembled as a disc of four. The QQQ/1 is fabricated using 3-inch wafer technology and uses aluminium contacts. Thicknesses of 40 to 1500 μm are available from MSL. Specifications of all three MSL detectors are shown in Table 5.1.

Table 5.1: *MSL detector specifications [65]. The value of the S2 active area provided on the MSL website [65] is incorrect [66]; the corrected value is given here.*

	S2	**QQQ/2**	**QQQ/1**
Wafer	4″ diameter	3″ diameter	3″ diameter
Package	PCB	PCB	PCB
Active Area	25.37 cm^2	1139 mm^2	1731 mm^2
Active Outer Diameter	140 mm	41 mm	50 mm
Active Inner Diameter	46.12 mm	9 mm	9 mm
Front Strips	48	16	-
Rear Sectors	16	24	-
Strip Pitch	491 μm	2.0 mm	-
Strip Separation	0.1 mm	0.1 mm	-
Sector Angle	22.5°	3.4°	82°

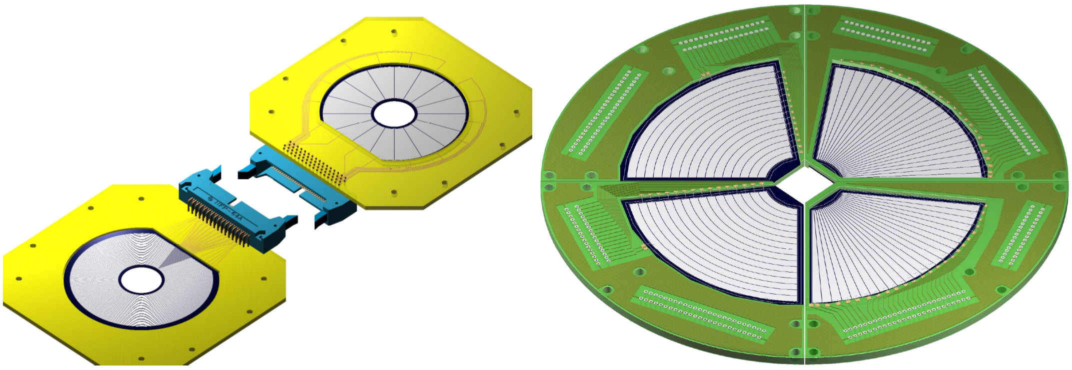

(a) Type S2 Detector **(b)** Type QQQ/2 Detector

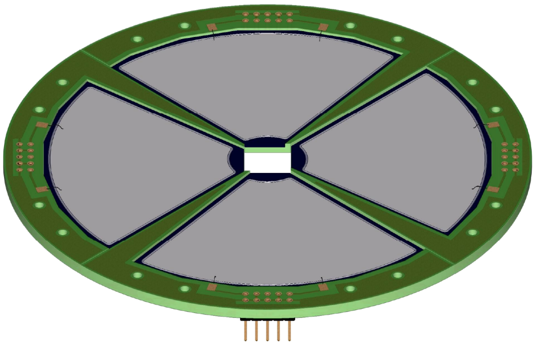

(c) Type QQQ/1 Detector

Figure 5.5: *MSL type S2, QQQ/2 and QQQ/1 detectors [65].*

5.2.2 Targets

Throughout the course of the experiment, solid polyethylene $(CH_2)_n$ and $(CD_2)_n$ targets were used. These are easier to handle than a hydrogen gas target; however, the disadvantage of using a target containing nuclei other than the ones of interest is the increase of background reactions as both fusion and scattering reactions are likely to occur on the natural Carbon in the polyethylene target.

Two sets of $(CH_2)_n$ targets were used during the experiment: one set was produced by Paul Demaret at UCL, Louvain-la-Neuve (LLN), Belgium, and the other set by Carmelo Marchetta at INFN LNS-Catania, Italy. Prior to the experiment the targets were tested for thickness and uniformity (a more thorough discussion of these measurements is given in Appendix A). Results of the thickness measurements are shown in Table 5.2. A non-uniform target results in a non-uniform energy loss of the beam through the target and therefore increases the uncertainty in determining the interaction energy of a reaction event. Targets with a measured thickness variation of more than 10% across the target surface area were discarded, which resulted in 5 of the 6 targets in the LNS-Catania set being omitted. The LNS-Catania target used in the experiment was that designated 'POS 6' with a measured thickness of 310 ± 25 μg/cm^2. The LLN targets were determined to have acceptable uniformity. The 233 μg/cm^2 LLN and 78 μg/cm^2 LLN targets were sandwiched together to create a 311 μg/cm^2 target, and the 258 μg/cm^2 LLN and 292 μg/cm^2 LLN were sandwiched to create a 550 μg/cm^2 target. These target thicknesses were chosen as a compromise between covering an energy region of interest in ^{22}Mg and a sufficiently thick target to give a meaningful reaction yield that can be measured. The energy loss of the ^{21}Na/^{21}Ne beam through the target was calculated using the technique discussed in Appendix B and the SRIM range data tables [67].

The LNS-Catania 368 μg/cm^2 $(CD_2)_n$ target was used to investigate background reactions on the ^{12}C/^{13}C and any other contaminants (e.g. ^{16}O) in the polyethylene target.

Table 5.2: *Nominal and measured thicknesses of* $(CH_2)_n$ *and* $(CD_2)_n$ *targets used in the experiment. LLN refers to targets manufactured at Louvain-la-Neuve, and LNS to those made at LNS-Catania.*

Target	Nominal Thickness (μg/cm^2)	Measured Thickness (μg/cm^2)
$(CH_2)_n$ LNS POS 6	321	310 ± 25
$(CH_2)_n$ LLN 250 #1	250	258 ± 21
$(CH_2)_n$ LLN 250 #2	250	292 ± 23
$(CH_2)_n$ LLN 80	80	78 ± 6
$(CH_2)_n$ LLN 250 #3	250	233 ± 19
$(CD_2)_n$ LNS 322	322	368 ± 26

5.3 Experimental Setup at TRIUMF

The experimental setup was optimised for the coincident detection of reaction ^{18}Ne and ^{4}He ions. The following sections discuss the experimental setup inside the TUDA scattering chamber and the electronic configuration of the TUDA instrumentation rack.

5.3.1 Reaction Kinematics and Detector Configuration

Six beam energies were chosen for the experiment, Table 5.3 provides a summary of: the beam energies; corresponding centre-of-mass energy in the inverse and direct channels; target thickness in the centre-of-mass frame; excitation energy in the compound ^{22}Mg nucleus; and the energy and spin of natural parity ^{22}Mg states[1] within the target thickness. The measurement at 5.476 MeV/A was intended as a comparison with the ANL measurement at $E_{cm}(\alpha,p) = 2.5$ MeV. The remaining beam energies were chosen to investigate the energy range $E_{cm}(\alpha,p) = 2.1 - 1.3$ MeV ($E_x(^{22}Mg) = 10.8 - 9.2$ MeV); a compromise between extending the measurements to as low an energy as possible into the energy region of astrophysical interest, and the anticipated low cross sections which make a measurement impractical.

At the chosen beam energies, the positioning of detectors was dictated by the ^{21}Na(p,α)^{18}Ne reaction kinematics (see Figures 5.6 and 5.7 for a beam energy of

---

[1] The resonances at $E_x(^{22}Mg) = 9.248$ [6$^+$] and $E_x(^{22}Mg) = 9.640$ [6$^+$] have been emitted from Table 5.3.

Table 5.3: *Summary of the beam energies used in the experiment, including the centre-of-mass energies for both (p,α) and (α,p) reactions, the target thickness in the centre-of-mass frame, the excitation energy in the compound ^{22}Mg nucleus and the energy and spin of natural-parity resonances within the target thickness.*

E_{beam} (MeV/A)	E_{cm}(p,α) (MeV)	E_{cm}(α,p) (MeV)	$(CH_2)_n$ Target (μg/cm^2)	ΔE_{cm}(α,p) (keV)	E_x(^{22}Mg) (MeV)	E_{res}(^{22}Mg) (MeV)	J^π [^{22}Ne]
5.476	5.27	2.63	311	122	10.7 ± 0.06	10.651	[3^-]
4.910	4.72	2.08	550	234	10.1 ± 0.12	10.085	[2^+]
4.642	4.46	1.82	311	138	9.90 ± 0.07	9.860	[0^+]
4.619	4.44	1.80	550	242	9.82 ± 0.12	9.860	[0^+]
						9.752	[2^+]
						9.709	[0^+]
4.310	4.14	1.50	550	258	9.52 ± 0.13	9.542	[2^+]
						9.482	[3^-]
4.120	3.96	1.32	550	260	9.33 ± 0.13	9.318	[2^+]

E_{beam} = 5.476 MeV/A). The experiment was performed using inverse kinematics which results in the heavy ^{18}Ne ions along with the ^{4}He ions being emitted in a forward cone. As such, all the detectors were positioned downstream of the target. The detectors used primarily for ^{18}Ne detection were 4x 35 μm QQQ-2 and 4x 1500 μm QQQ-1 in a CD-PAD ΔE-E arrangement. For a beam energy of 5.476 MeV/A, the energy of the emitted ^{18}Ne ions, see Figure 5.6, ranges from approximately 76 - 102 MeV. ^{18}Ne ions at energies of 76 - 102 MeV are stopped in the 65 μm S2 DSSSD, whereas they deposit 60 - 55 MeV in the 35 μm QQQ-2 DSSSD. The CD-PAD telescope was positioned downstream of the target, with the QQQ/2 detectors a distance of 34.6 ± 0.1 cm and the QQQ/1 detectors a distance of 35.7 ± 0.1 cm from the target; providing an effective laboratory angular coverage for the CD-PAD telescope of 1.6° - 6.6° (assuming a point beam spot at the centre of the target position). As can be seen from Figure 5.7, this angular range covers the majority of the ^{18}Ne cone, and provides a sufficient angular gap for the more intense, high-energy ^{21}Na beam to pass through without hitting the detector.

The detectors chosen for the primary detection of ^{4}He ions were a pair of S2 DSSSDs in a ΔE-E arrangement: 1x 65 μm ΔE and 1x 500 μm E. The type S2 was chosen over the type QQQ-2 since the type S2 provides a greater angular resolution as a result of the greater number of front $p^{+}n$ strips. The S2-S2 telescope was positioned downstream of the target, with the ΔE S2 detector a distance of 9.5 ± 0.1 cm and the E S2 detector a distance of 11.0 ± 0.1 cm from the target; providing an effective laboratory angular coverage for the S2-S2 telescope of 7.0° - 17.6° (assuming a point beam spot at the centre of the target position). A schematic of the detector arrangement in the TUDA scattering chamber is shown in Figure 5.8.

5.3.2 Electronics and Data Acquisition

The data acquisition system is shown schematically in Figure 5.9. The preamplifiers used for the amplification of signals from the S2 and CD detectors were RAL108 charge sensitive preamplifiers [68], and those for the PAD were Cooknell EC572 charge sensitive preamplifiers. The preamplifiers were positioned as close to the detectors as possible to reduce noise on the input signal to the preamplifier. As such, 128 RAL108 preamplifiers were mounted

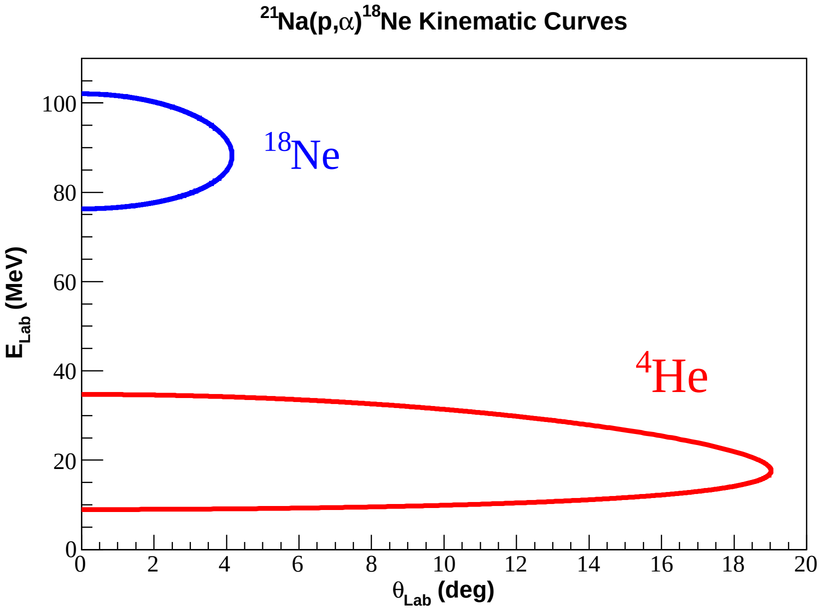

Figure 5.6: *E_{Lab} vs. θ_{Lab} kinematic loci of the ^{18}Ne and ^{4}He products from the ^{21}Na(p,α)^{18}Ne reaction at a beam energy of E_{beam} = 5.476 MeV/A. The reaction is assumed to occur at the mid-point of the 311 μg/cm^2 $(CH_2)_n$ target. Energy losses of the ^{18}Ne and ^{4}He ions through the target and detector dead-layers are not considered here.*

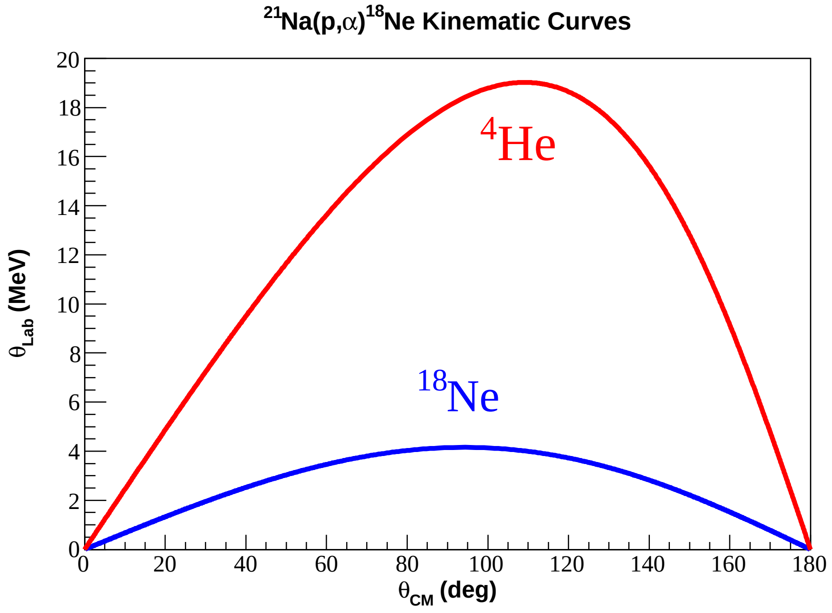

Figure 5.7: *θ_{Lab} vs. θ_{cm} kinematics of the ^{18}Ne and ^{4}He products from the ^{21}Na(p,α)^{18}Ne reaction at a beam energy of E_{beam} = 5.476 MeV/A. The reaction is assumed to occur at the mid-point of the 311 μg/cm^2 $(CH_2)_n$ target. Energy losses of the ^{18}Ne and ^{4}He ions through the target and detector dead-layers are not considered here.*

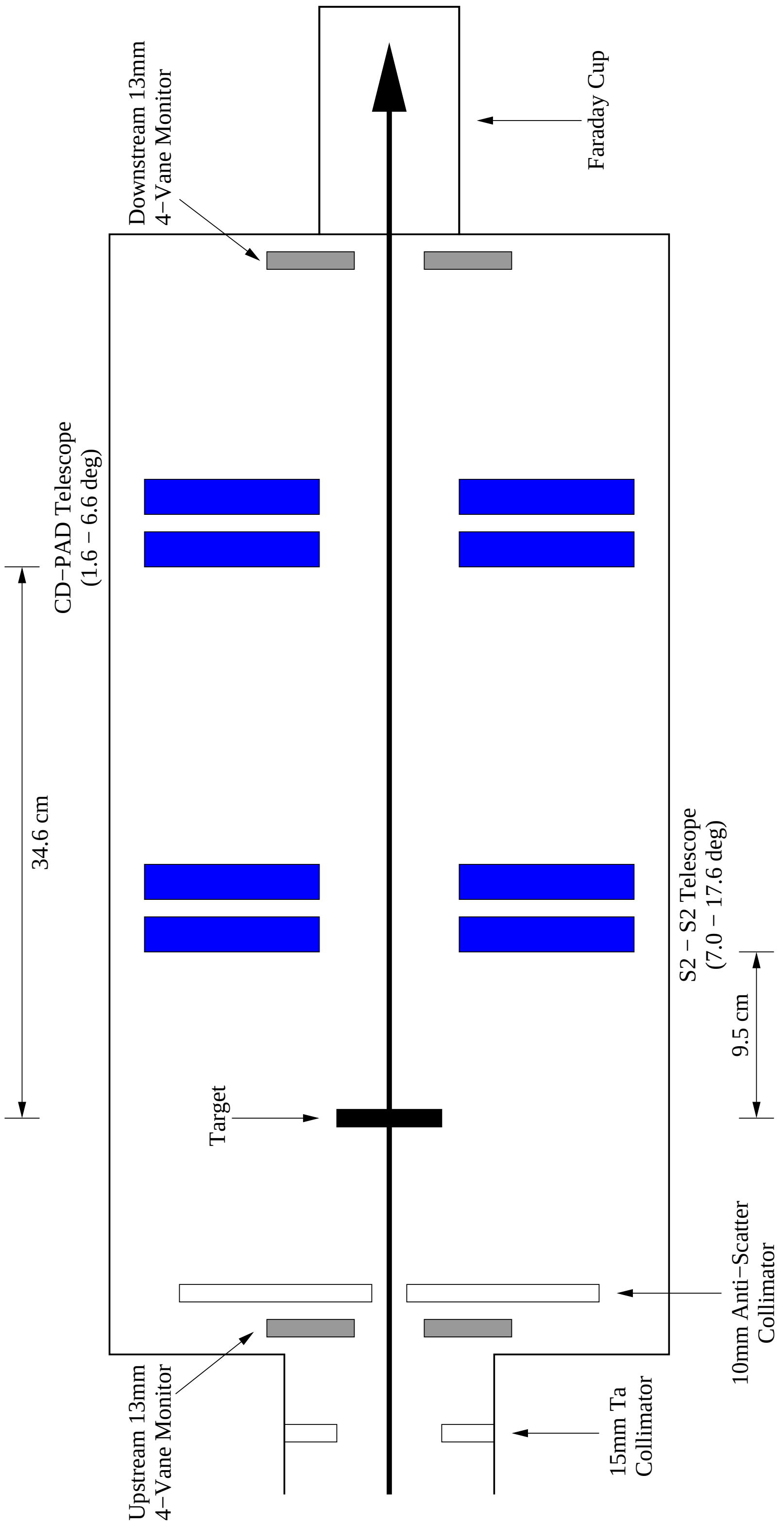

Figure 5.8: *Scheme of the experimental setup within the TUDA scattering chamber (not to scale).*

on a plate directly behind the *E* S2 detector for the S2-S2 telescope, and another 160 RAL108 preamplifiers were mounted on a plate directly behind the *E* PAD detector for the CD detector. The 4 Cooknell EC575 preamplifiers could not be mounted within the TUDA scattering chamber so they were placed on the outside and were connected via a vacuum feedthrough to the PAD detector. Since the experiment was conducted in vacuum, conventional fan-assisted cooling for the RAL108 preamplifiers was not possible. Instead, copper heat-sinks were mounted in thermal contact, using Gap Pad® 5000S35 [69], with the preamplifier circuit boards. A 1/4 inch nylon tubing was used to connect all the heat-sinks, creating a cooling system through which ethanol was pumped, using an external FTS RS44CL2 recirculating cooler [70] set to a constant temperature of -10°C. Throughout the experiment the preamplifiers maintained a stable temperature between T ~ 10° - 30°C.

Cables for detector output signals, HV bias inputs, test signal inputs and thermocouple connectors exit the chamber through vacuum feedthroughs on the rear flange of the TUDA chamber. The output signals from the preamplifiers are carried via IDC 34-way cables to a set of junction boxes located in the electronics rack. Both the electronics rack and TUDA scattering chamber were electrically isolated from the experimental hall and the ISAC II beamline, providing a separate clean ground for the experimental equipment and allowing all noise levels and possible interferences to be kept at a minimum. The junction boxes split each 34-way cable into 2x 16-way outputs which were fed into the 8-channel RAL109 shaping amplifier/discriminator units [68]. The RAL109 units provide two output signals: an amplified analogue signal and a leading-edge discriminated digital signal. The amplification of each RAL109 channel is set using interchangeable DIP resistors and a 100 Ω terminator SIL resistor. 0.022 kΩ resistors were used in the S2-ΔE RAL109 modules (^{4}He ions ~ 2.5 MeV), and 2.2 kΩ resistors in the S2-E RAL109 modules (^{4}He ions ≤ 32 MeV). The CD RAL109 modules used 3.3 kΩ resistors (^{18}Ne ions ~ 55 MeV) and 4.7 kΩ resistors were used in the PAD RAL109 modules (^{18}Ne ions ≤ 55 MeV). A summary of the resistors used and corresponding Full-Scale Range (FSR) of the RAL109 amplifiers is given in Table 5.4. The linearity of the RAL108 preamplifiers used in conjunction with the RAL109 shaping amplifiers is approximately 0.03 % [68], which was sufficient for this experiment. The

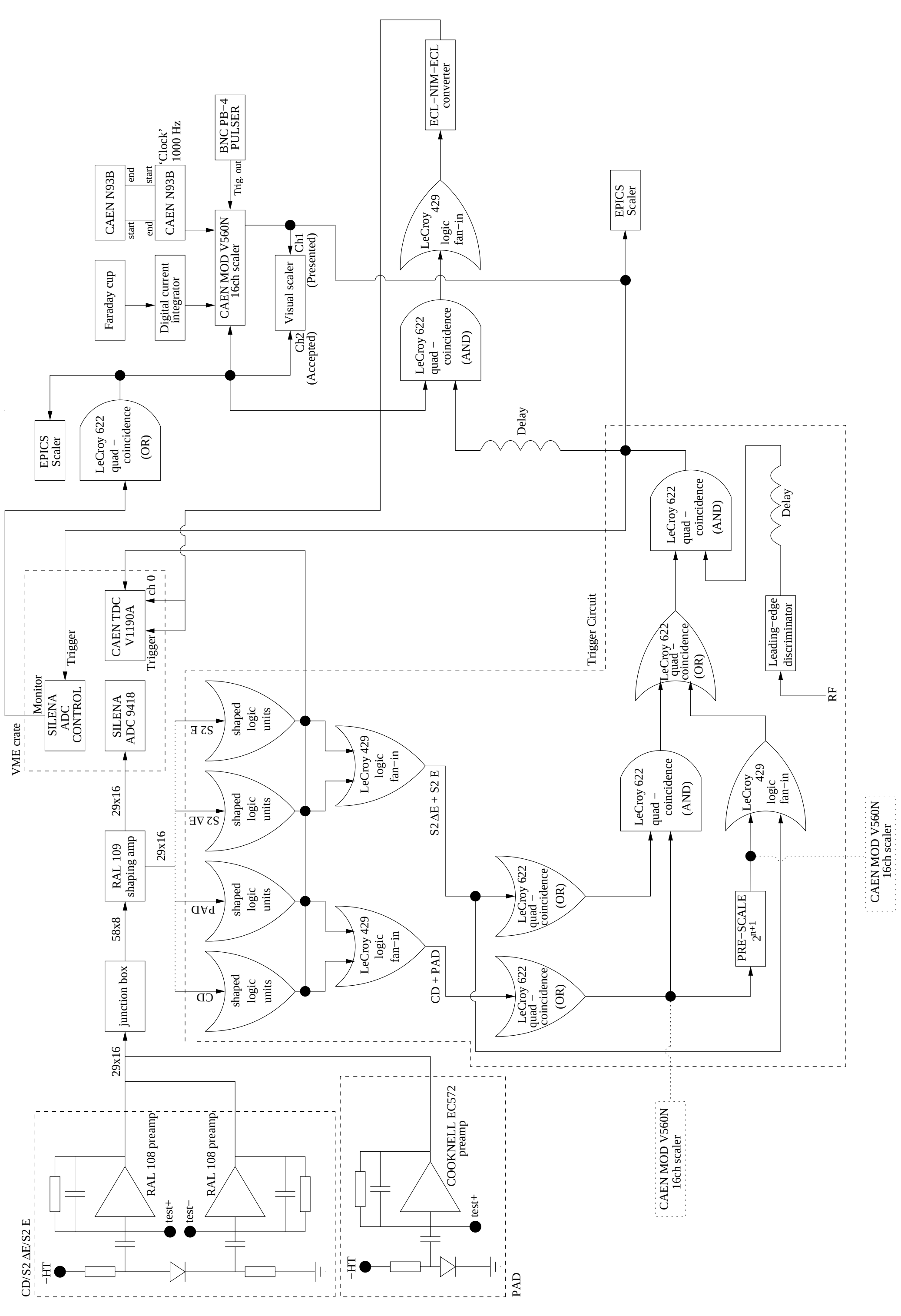

***Figure 5.9**: Schematic diagram of the experimental electronics setup.*

analogue signals were sent to 15 32-channel Silena 9418/6V VME Analogue-to-Digital Converters (ADCs).

Table 5.4: *DIP Gain resistors and corresponding full-scale range in the RAL109 shaping amplifier modules.*

Gain Resistor DIP (kΩ)	Nominal FSR (Terminated) (MeV)
0.022	17.1
1	33.3
2.2	53.2
3.3	71.4
4.7	94.9

The discriminated digital output of the RAL109 modules was daisy chained to both logic modules for the trigger and CAEN V1190A Time-to-Digital Converters (TDCs). The TDCs were used in common stop mode, *i.e.* started by the discriminator output of the RAL109 amplifiers and stopped by the RF signal from the accelerator. In common stop mode, the TDCs allow for measurement of the time-of-flight of particles with respect to the ISAC pre-buncher.

Trigger

The trigger logic used for the acquisition system, see Figure 5.9, consisted of a total OR of all the detectors in coincidence (AND) with the accelerator RF signal.

The discriminator logic output from the RAL109 amplifiers was sent to Edinburgh-built CAMAC[2] 48-input logic modules. Each module has 3x16 channel inputs and 4 possible output options. The first three outputs give the OR of each group of 16 input channels and the fourth output gives the total OR of all 48 input channels. Each detector telescope (CD-PAD, S2-S2) was assigned one of two logic Fan In/Out (FIFO) modules (LeCroy 429A); the output of the CAMAC modules was sent accordingly to each FIFO, creating a total OR for the entirety of each detector telescope. The output of the FIFO modules for each telescope was sent to multiple destinations: one output of each FIFO was sent to a quad-coincidence module (LeCroy 622) set in AND mode; this created

---

[2] Computer Automated Measurement And Control.

a coincidence condition between events in the CD-PAD and S2-S2 telescopes. Another output of the S2-S2 FIFO was sent to a secondary FIFO module; the other input to this secondary FIFO was the pre-scaled output of the CD-PAD FIFO. The CD-PAD FIFO output was pre-scaled because of the high number of scattering events in the CD-PAD telescope. This secondary FIFO acted as a total OR for events in all detectors.

The output from the secondary FIFO and the quad-coincidence (AND) module was sent to a second quad-coincidence module set in OR mode. The output of this second quad-coincidence module was sent to a third quad-coincidence module set in AND mode, with the delayed RF signal from the accelerator. This was the primary experimental trigger and was sent to the Silena ADC Control (SAC) module. If the ADCs were not in 'busy' mode, the SAC module passed the trigger to the ADCs and the analogue-to-digital conversion of the ADC input was made. The SAC module produced a 'Monitor' output indicating an accepted trigger.

Some logic signals in the trigger were embedded within the data as scalers. This was performed by a CAEN V560N 16-channel scaler module; a single width VME module housing 16 independent 32-bit counting channels. Seven scalers were used: triggers presented, triggers accepted, 1 kHz clock, Faraday cup/digital current integrator, 2Hz pulser, CD-PAD triggers and CD-PAD pre-scaled triggers. These scalers were used for online and offline diagnostics.

Timing

Timing information was provided by three 128-channel multi-hit CAEN V1190A TDCs, used in common stop mode. The START trigger for a TDC channel was the discriminator logic output from the corresponding RAL109 amplifier, indicating an event in one of the detectors had occurred. The main experimental trigger was delayed by a pair of B007 delay modules to allow for the ADCs to process the input ADC signal. The trigger was then sent to a quad-coincidence module set in AND mode with the SAC monitor output. The output of the quad-coincidence formed the STOP trigger for the TDCs and maintained synchronisation between the ADC and TDC data.

The number of TDC clock cycles between the TDC START and STOP triggers is the TDC conversion value. The TDCs worked in an inverse timing mode, thus more highly energetic particles had a greater conversion value.

Acquisition

The ADC and TDC modules were readout by a VME (Versa Module Eurocard) CPU, controlled by MIDAS (Multi Instance Data Acquisition System) software [71] running on a Sun Microsystems SunBlade 100 [72] workstation. Raw data files were written to hard disk and stored for offline analysis.

The acquisition system was inhibited by the finite time taken for the ADCs to accept, convert and readout data. During this time the ADCs are in a 'busy' state and any triggers which arrive at the SAC will not be sent to the ADCs. The time during which the ADC is non-responsive is referred to as the system *dead-time* and is calculated using Equation 5.1.

$$\text{dead time} = \frac{\text{total triggers presented} - \text{triggers accepted}}{\text{total triggers presented}} \tag{5.1}$$

5.4 Experimental Procedure

The experiment was performed over a 19 day period: 8 days of experimental setting up and calibration, 11 days of beam time and 4 days of post run calibrations and dismantling. The setting up consisted in mounting and cabling all the detectors, electronics and other equipment within the TUDA chamber, and building and configuring the data acquisition and trigger systems. The silicon detectors were calibrated using a Berkeley Nucleonics Corporation (BNC) PB-4 precision pulse generator [73] and a mixed α source[3]. A more detailed discussion and calculation of the detector calibration is provided in the following Data Analysis chapter.

The first experimental measurement was performed at a beam energy of 5.476 MeV/A, followed by 4.910, 4.619, 4.310 and 4.120 MeV/A, and then back up to 4.642 MeV/A as a potential energy of interest identified during online analysis. The measurement at 5.476 MeV/A is not in the region of astrophysically important energies, however, with the highest ^{21}Na(p,α)^{18}Ne

---

[3] A standard ^{239}Pu,^{241}Am,^{244}Cm α-emitting closed source, with a 2π emission solid angle. The alpha particles used in the calibration were emitted with 5.15659 (^{239}Pu), 5.48556 (^{241}Am) and 5.80477 (^{244}Cm) MeV.

cross section of the six beam energies investigated, it offered the opportunity to test the setup and (p,α) event selection techniques before moving to lower energies. At each beam energy a small amount of time was spent with the ^{21}Na beam on the 368 μg/cm^2 $(CD_2)_n$ target, this was for offline investigation of background reactions primarily on the ^{12}C in the target.

The amount of time spent at each beam energy is given in Table 5.5. Simple online analysis of the data provided an estimate of the ^{21}Na(p,α)^{18}Ne reaction yield, and once sufficient statistics had been collected, the beam energy was lowered to the next pre-tuned energy.

Table 5.5: *Time spent at each energy with a live ^{21}Na beam on a $(CH_2)_n$ target.*

Beam Energy (MeV/A)	^{21}Na Beam on Target (hrs)
5.476	4.7
4.910	17.9
4.642	11.4
4.619	18.4
4.310	33.7
4.120	47.7

5.5 Monte-Carlo Simulation

A Monte-Carlo simulation was written to calculate the efficiency of detecting ^{4}He ions in the S2-S2 telescope in coincidence with ^{18}Ne ions in the CD-PAD telescope. The simulation also calculated the energy of all particles in the detectors, taking into account energy losses in the target and detector dead-layers, allowing for the creation of simulated kinematic loci for comparison with the experimental data.

The simulation code was written in Fortran 90, and was substantially modified from an original simulation written by Dr. Alex Murphy for the study of the ^{18}F(p,α)^{15}O reaction [74]. The code for this experiment simulated the (p,α) reaction and the background (p,p) and (^{12}C,^{12}C) reactions for both ^{21}Na and ^{21}Ne beam species.

The code simulates a random interaction depth in a $(CH_2)_n$ target, and includes the energy loss of the beam species in the target; all energy losses are calculated in a subroutine which uses the method discussed in Appendix B and SRIM [67] range data tables. At the interaction location, the simulation generates randomised centre of mass θ and ϕ angles for the reaction products such that $0 < \theta < \pi$ and $-\pi < \phi < \pi$; isotropic and non-isotropic angular distributions can be simulated. The interaction energy, and θ and ϕ angles are used to calculate the kinematics of the reaction products. The code allows the user to generate the reaction products in either the ground state or an excited state. After generating the reaction products, the simulation determines whether both emitted particles are within the θ and ϕ angular ranges of either ΔE-E telescope; the code takes into account the separation between front p^+n strips, and the non-360° ϕ angular coverage of both types of DSSSD[4]. If the particles are within range, the energy losses of the reaction products through the remaining target, detector dead-layers and the energy deposited in the ΔE detector are calculated. During the data analysis, low energy cuts were applied to each detector to remove low energy background events. The same low energy cuts were applied to the simulated events.

For every ^{21}Na beam and $(CH_2)_n$ target combination given in Table 5.3, the simulation was performed for 1,000,000 events. All possible event coincidences were recorded, including those for ions stopped in the ΔE detector. An example of a screen output of the Monte-Carlo code indicating the total coincidence is shown in Figure 5.10. The results of the Monte-Carlo simulation, including detection efficiencies and spectra for comparison with experimental data, will be shown in the Data Analysis chapter.

---

[4] Both the type S2 and QQQ/2 detectors do not have full 360° ϕ angular coverage, which can be seen in Figures 5.5(a) and 5.5(b).

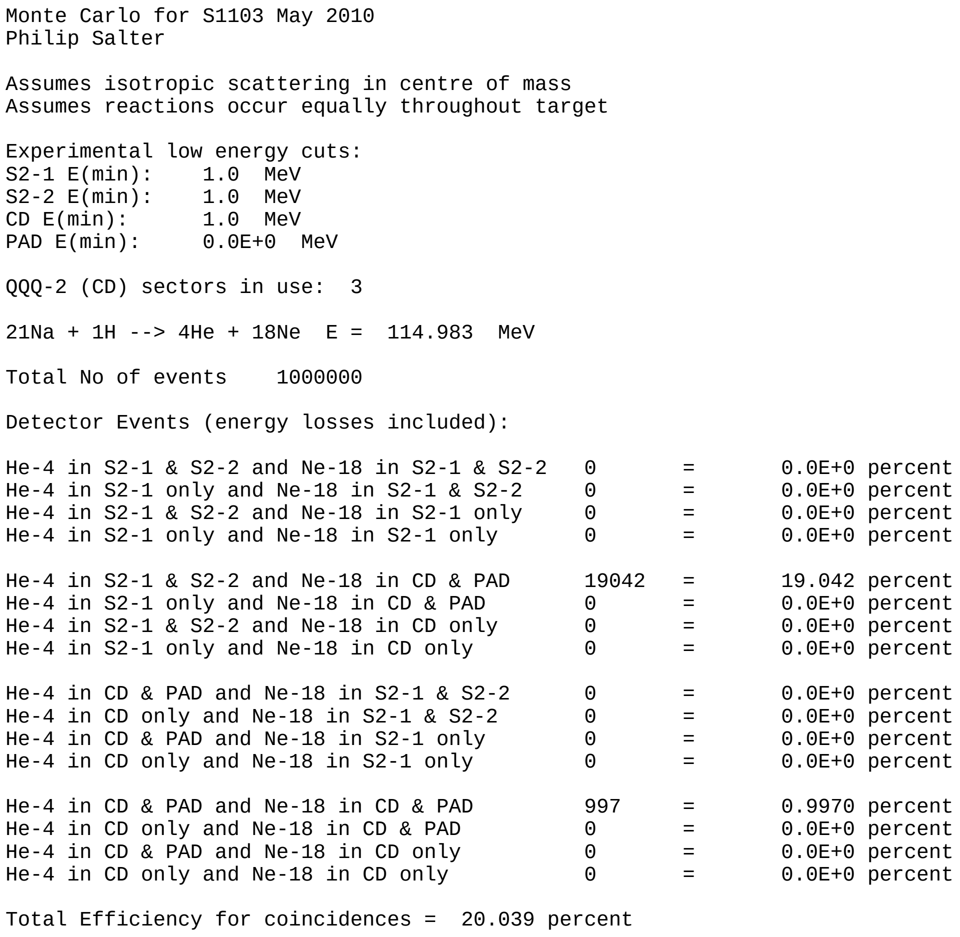

```
Monte Carlo for S1103 May 2010
Philip Salter

Assumes isotropic scattering in centre of mass
Assumes reactions occur equally throughout target

Experimental low energy cuts:
S2-1 E(min):    1.0  MeV
S2-2 E(min):    1.0  MeV
CD E(min):      1.0  MeV
PAD E(min):     0.0E+0  MeV

QQQ-2 (CD) sectors in use:  3

21Na + 1H --> 4He + 18Ne  E =  114.983  MeV

Total No of events    1000000

Detector Events (energy losses included):

He-4 in S2-1 & S2-2 and Ne-18 in S2-1 & S2-2   0       =       0.0E+0 percent
He-4 in S2-1 only and Ne-18 in S2-1 & S2-2     0       =       0.0E+0 percent
He-4 in S2-1 & S2-2 and Ne-18 in S2-1 only     0       =       0.0E+0 percent
He-4 in S2-1 only and Ne-18 in S2-1 only       0       =       0.0E+0 percent

He-4 in S2-1 & S2-2 and Ne-18 in CD & PAD      19042   =       19.042 percent
He-4 in S2-1 only and Ne-18 in CD & PAD        0       =       0.0E+0 percent
He-4 in S2-1 & S2-2 and Ne-18 in CD only       0       =       0.0E+0 percent
He-4 in S2-1 only and Ne-18 in CD only         0       =       0.0E+0 percent

He-4 in CD & PAD and Ne-18 in S2-1 & S2-2      0       =       0.0E+0 percent
He-4 in CD only and Ne-18 in S2-1 & S2-2       0       =       0.0E+0 percent
He-4 in CD & PAD and Ne-18 in S2-1 only        0       =       0.0E+0 percent
He-4 in CD only and Ne-18 in S2-1 only         0       =       0.0E+0 percent

He-4 in CD & PAD and Ne-18 in CD & PAD         997     =       0.9970 percent
He-4 in CD only and Ne-18 in CD & PAD          0       =       0.0E+0 percent
He-4 in CD & PAD and Ne-18 in CD only          0       =       0.0E+0 percent
He-4 in CD only and Ne-18 in CD only           0       =       0.0E+0 percent

Total Efficiency for coincidences =  20.039 percent
```

Figure 5.10: *Sample Monte-Carlo output for the ^{21}Na(p,α)^{18}Ne reaction. The simulation was performed for a 5.476 MeV/A ^{21}Na beam on a 311 μg/cm^2 $(CH_2)_n$ target. Under these conditions, the total coincidence detection efficiency for our experimental set up is 20%.*

Chapter 6

Data Analysis and Results

This chapter details the procedure followed to extract the cross sections from the experimental data. It describes the calibration of the detectors and the selection criteria applied to the data to obtain the ^{21}Na(α,p)^{18}Ne reaction yields. It also includes sections on the ^{21}Na beam intensity measurements; calculation of the coincident event detection efficiencies; comparisons of the experimental data with Monte-Carlo simulations; and calculations of the ^{18}Ne(α,p)^{21}Na cross section.

6.1 Detector Calibration

Before any meaningful information was extracted from the silicon detectors, all 292 detector channels were individually energy and time calibrated. These procedures are described below.

6.1.1 Energy Calibration

The purpose of the energy calibration is to establish a correspondence between ADC channel number and the energy deposited by a particle in the active area of the detector. Given the linear response of both the RAL108 preamplifiers and RAL109 amplifiers (see Section 5.3.2) a linear dependence is expected between the energy of a particle and its corresponding peak position in the ADC spectrum. The aim of the calibration is thus to determine the value of the *gain* and *offset* for each detector strip, by means of a linear best fit to the experimental data as:

$$\text{Energy (MeV)} = \text{gain(MeV/channel)} \times (\text{ADC(channel)} - \text{offset(channel)}) \tag{6.1}$$

The linearity of each detector strip was verified during the experimental setup phase by a pulser walk-through, performed using the BNC PB-4 pulse generator at the test input of each preamplifier module. The pulse generator was initially set at its maximum amplitude, with suitable attenuation such that it was within the full-scale range of the strip being examined. Enough counts were recorded before reducing the pulse amplitude in identical steps, thus producing a spectrum containing nine peaks, as shown in Figure 6.1. The channel separation between each of the nine peaks is identical for a system with a linear response. The pulser walk-through provided an indication of the electronic offset of a strip: the linear fit of the pulser peak position versus pulse amplitude enabled us to extract an offset for online analysis. For the offline analysis the offset was obtained from the linear fit performed to mixed-alpha and experimental data as discussed in the following paragraph.

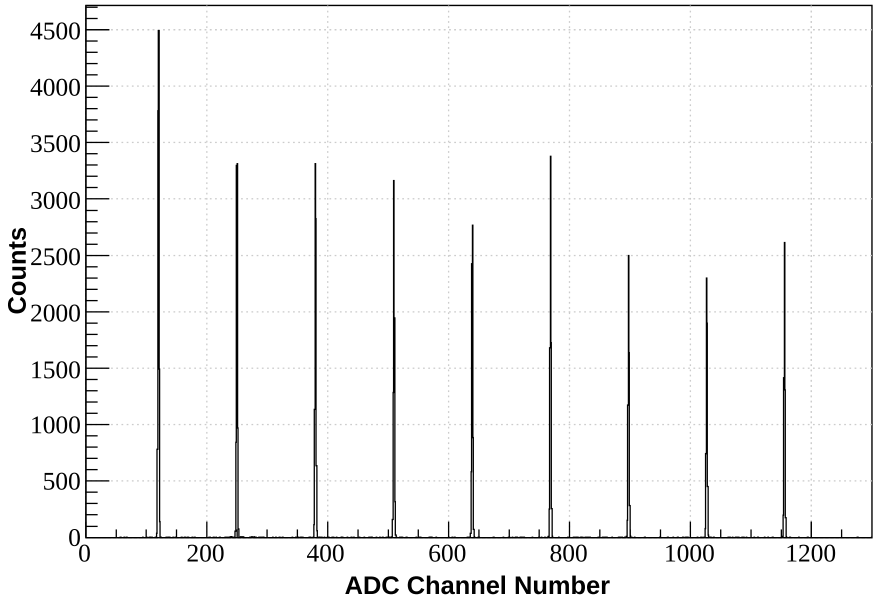

Figure 6.1: *Example of a pulser walk-through spectrum from a front* $p^{+}n$ *CD strip.*

It is desirable to calibrate a detector using the same charged particles as those detected in the reaction measurement and ideally at energies similar to the emitted reaction particles. The reason for this is a phenomenon in semiconductor detectors known as *pulse height defect* [56]; the pulse height of heavy ions is observed to be much less than that for light ions (^{1}H, ^{4}He *etc.*) at the same energy, *i.e.* for heavy ions there is an apparent difference between the measured energy and true energy as large as 19%. The mechanisms that contribute to pulse height defect are discussed in more detail in [56].

For the S2 ΔE-E detectors it was sufficient to use a mixed alpha source for the calibration since the detectors were primarily used for the detection of reaction alphas at energies $\sim$ 2.5 MeV (ΔE) and $\leq$ 33 MeV (E), respectively. The energy calibration of each S2 strip was performed using the source positioned at the target location of the TUDA chamber and pointed downstream at the detector arrays[1]. Data was collected over a time period of approximately 1.5 hours to accumulate sufficient statistics; a sample spectrum is shown in Figure 6.2. For every detector strip, the peak centroid of each alpha peak was identified using the MIDAS peak-find function. The peak centroid was then associated with the energy of the corresponding alpha particle after taking into account energy losses in the detector dead-layers, corrected for the θ dependence, and treating the alpha source as a point-like source. The angle of every front $p^{+}n$ strip was calculated to the strip mid-point. The dead-layers estimated for each detector are shown in Table 6.1. The estimates for the dead-layers are based on previous experience of the Edinburgh Nuclear Physics Group with MSL DSSSDs and specifications provided by MSL. However, these values were checked, and corrected if necessary, following an iterative comparison with simulated spectra (see Section 6.2.9), hence the variation of the dead-layer values provided in Table 6.1.

For every S2 strip, a linear fit was performed on the mixed alpha data, such as the one shown in Figure 6.3; the gain of the detector strip is the gradient of the straight line, and the offset is the y-axis intercept. A C^{++} script was written for use with the ROOT Analysis Software [75] to perform the least squares fit for all detector strips and to output the resulting gain and offset values to file.

The calibration of the CD and PAD detectors cannot be based solely on ~5.5

---

[1] Calibration of the E detectors of both ΔE-E telescopes was performed with the ΔE detectors removed since the $\sim$ 5.5 MeV alpha particles would be stopped in the ΔE detectors.

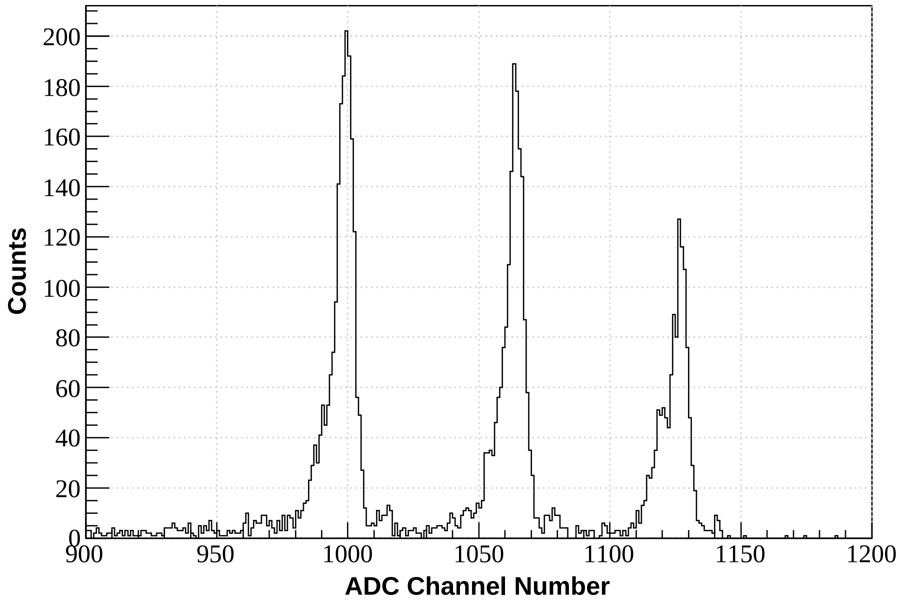

Figure 6.2: *Uncalibrated mixed alpha spectrum from a front* $p^{+}n$ *S2 strip.*

Table 6.1: *Estimated dead-layers included in all energy loss calculations following iteration procedure (see text).*

Dead-layer	Thickness (μm)
QQQ/2 front $p^{+}n$ junction	0.50
QQQ/2 rear $n^{+}n$ ohmic	0.50
QQQ/1 front	0.80
S2 front $p^{+}n$ junction	0.80
S2 rear $n^{+}n$ ohmic	0.80

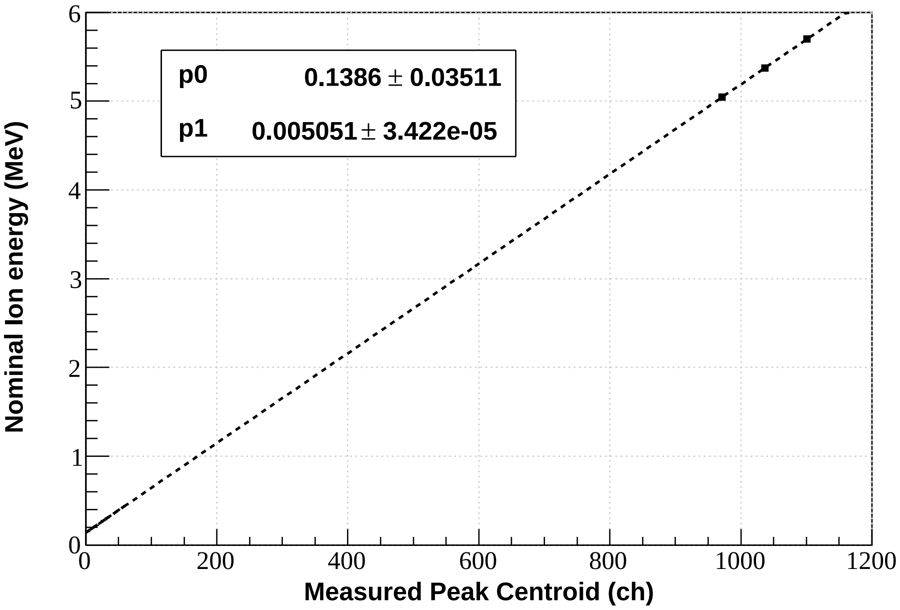

Figure 6.3: *Example of a calibration fit for a front* p^+n *S2 strip. The data points have been increased in size for visual purposes and obscure the error bars. The linear fit parameters p0 and p1 correspond to the y-axis intercept and gradient respectively.*

MeV alpha particles since the detectors were used for the detection of ^{18}Ne ions at energies ~ 55 MeV. A fourth data point in the region of 55 MeV was included in the calibration: the ion used was ^{21}Ne from Rutherford scattering off ^{12}C in the $(CH_2)_n$ target using a stable ^{21}Ne beam at 5.357 MeV/A on a 311 μg/cm^2 $(CH_2)_n$ target. For each CD strip and PAD sector, the peak centroid of the ^{21}Ne Rutherford peak was identified, as in Figure 6.4. ^{21}Ne events in the rear n$^+$n CD and PAD sectors were confined to those that passed through the inner-most (θ_{lab} = 1.6°) front p$^+$n strip of the CD detector, since there is no θ angle restriction on events in the rear n$^+$n CD and PAD sectors. The energy of the ^{21}Ne deposited in both the CD and PAD detectors was determined from the reaction kinematics at each detector channel after correction for energy losses in all relevant dead-layers and the target thickness. At a ^{21}Ne beam energy of 5.357 MeV/A, the ^{12}C(^{21}Ne,^{21}Ne)^{12}C Rutherford differential cross section and stopping power vary by 8.3% and 1.3% over a target thickness of 860 keV (311 μg/cm^2); a thin target treatment was employed (see Chapter 4) and the mean effective energy taken at the mid-target position ($E_{\text{eff}} = E_0 - \Delta E/2$, where E_0 is the beam energy and ΔE the energy loss over the target).

For every CD strip and PAD detector, a linear fit was performed to the mixed alpha and ^{12}C(^{21}Ne,^{21}Ne)^{12}C data. A sample calibration line is shown in Figure 6.5.

6.1.2 Time Calibration

The purpose of the time calibration is to establish a correspondence between TDC channel number and a time interval. The TDCs work on an internal clock and have a fixed gain of 0.8 ns/channel; the aim of the calibration is to determine the TDC offset for each detector strip, such that the time of a peak in a TDC spectrum is calculated as Equation 6.2:

$$\text{Time (ns)} = 0.8 \times \text{TDC(channel)} + \text{offset(ns)} \tag{6.2}$$

One of the particle identification techniques (discussed later in this chapter) used in this analysis was the selection of coincident-timing events between the two ΔE-E telescopes. As such, timing information was only required for the ΔE detectors of the ΔE-E telescopes, so the S2-E and PAD detectors were not time

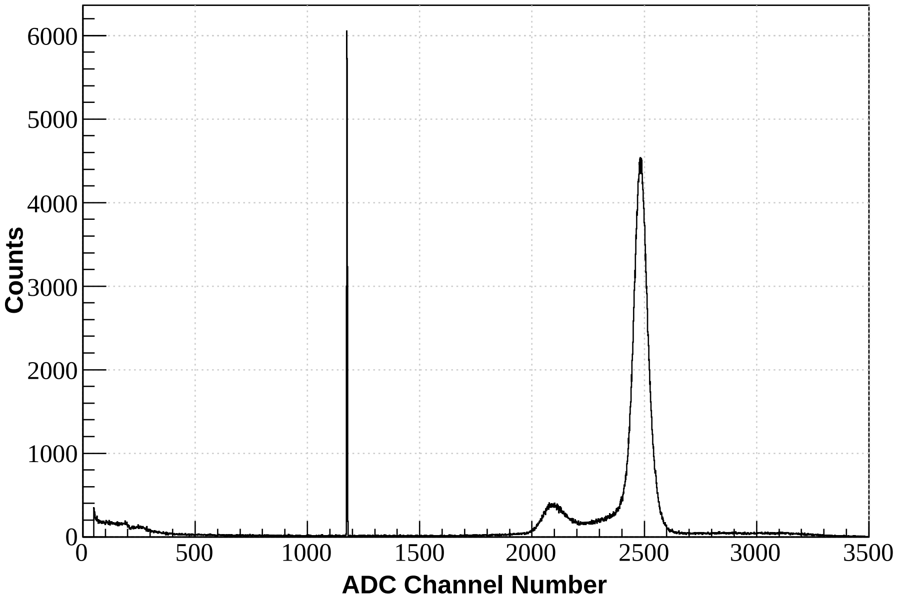

Figure 6.4: *Sample ADC spectrum of a front* $p^{+}n$ *CD strip with 5.357 MeV/A* ^{21}*Ne on a 311 µg/cm*^{2} *(CH*$_{2}$*)*$_{n}$ *target. The dominant peak around channel 2480 corresponds to the* ^{21}*Ne from* ^{12}*C(*^{21}*Ne,*^{21}*Ne)*^{12}*C Rutherford scattering. A pulser signal is observed at around channel 1180, and the smaller peak around channel 2100 is believed to correspond to* ^{18}*F ions from the* ^{1}*H(*^{21}*Ne,*^{18}*F)*^{4}*He reaction. However, since no further analysis has been made on this peak, it is unknown if there are other reactions contributing to its height.*

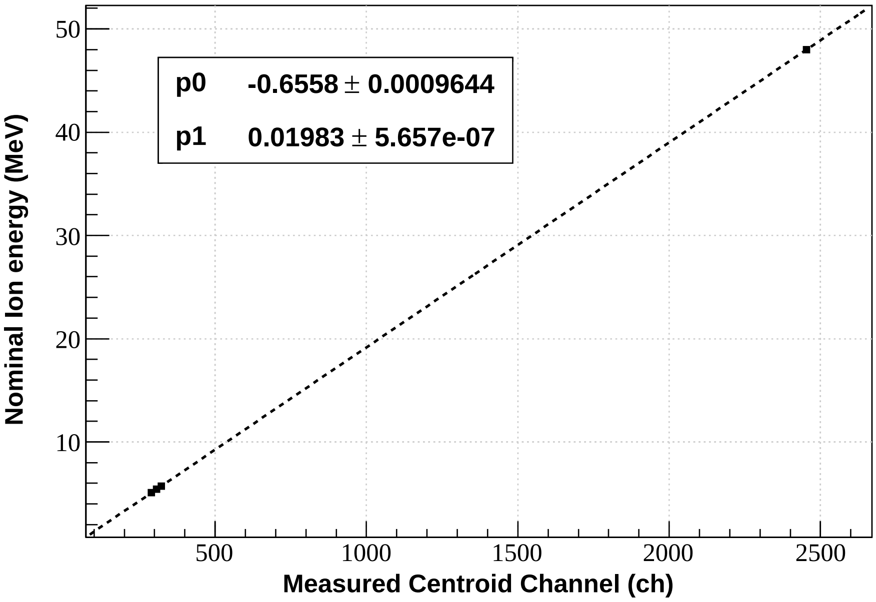

Figure 6.5: *Sample calibration fit for a front p^+n CD strip. The data points have been increased in size for visual purposes. The linear fit parameters p0 and p1 correspond to the y-axis intercept and gradient respectively.*

calibrated, and only the front p^+n strips of the ΔE detectors were calibrated.

The TDC signal received was relative to the RF signal of the accelerator, therefore the time-of-flight of events in the detectors was not relative to the target but to the pre-buncher of the accelerator. Thus, in each detector an arbitrary value for the central TDC channel was chosen to normalise all strips to; the offset from the arbitrary value for each strip was then determined. The calibration was performed using the dataset from the ^{21}Na run at 5.476 MeV/A beam energy. For the CD strips, the peak corresponding to ^{21}Na ions from ^{12}C(^{21}Na,^{21}Na)^{12}C scattering were identified (a sample TDC spectrum is shown in Figure 6.6); and for the S2-ΔE strips the peak corresponding to protons from ^{1}H(^{21}Na,^{21}Na)^{1}H scattering were selected.

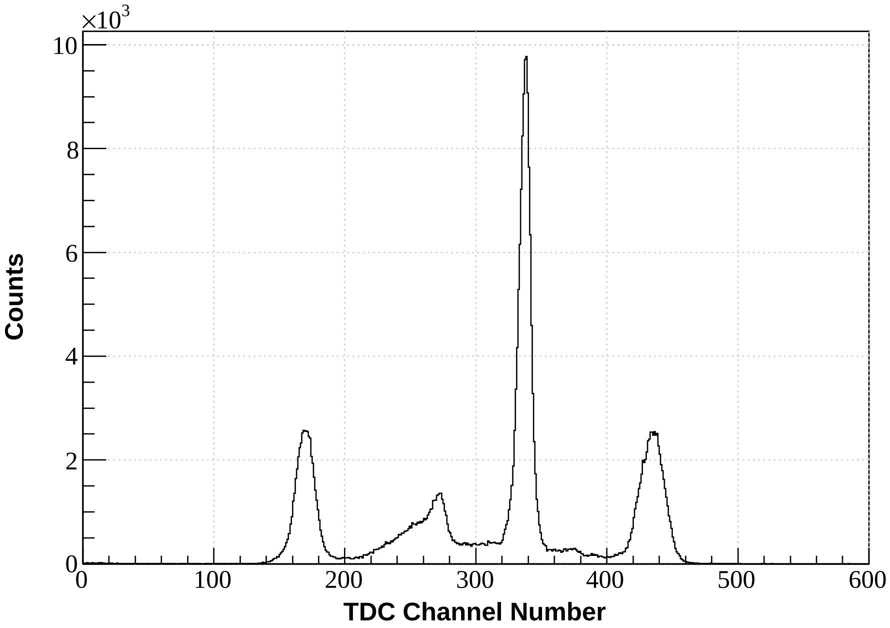

Figure 6.6: *Sample TDC spectrum of a front p^+n CD strip taken with 5.476 MeV/A ^{21}Na beam on a 311 μg/cm^2 $(CH_2)_n$ target. The dominant peak around channel 340 corresponds to ^{21}Na from ^{12}C(^{21}Na,^{21}Na)^{12}C Rutherford scattering.*

6.2 ^{21}Na(p,α)^{18}Ne Event Selection

As mentioned in Chapter 5, the offline analysis was performed using the MIDAS software and in particular, the MIDAS-SORT program. A sort code was written in Fortran 77 and used by the MIDAS-SORT program to extract ^{21}Na(p,α)^{18}Ne events from the raw data files, by selecting ^{4}He events in the S2-S2 telescope in coincidence with ^{18}Ne events in the CD-PAD telescope. To achieve this aim, a number of conditions, referred to as 'gates' or 'cuts', were applied to the raw data. These included:

- DSSSD Equal-energy gates
- ΔE-E telescope event gates
- Particle identification mass gates
- Co-planar two-body event gates
- Prompt-coincidence gates

Since the gate conditions applied to the raw data were dependent on the centre of mass energy, all the gates (except co-planar two-body events) were reset at each new beam energy. The following subsections discuss the implementation of the above conditions; sample spectra from all beam energies will be presented.

6.2.1 Equal-Energy Event Selection

The DSSSDs used in this study were constructed from a single wafer of silicon segmented into front radial strips and rear azimuthal sectors. If a charge particle interacts with the detector at a segment edge or in the space between segments, a phenomenon known as *charge sharing* may occur where the cloud of charge created by a single interaction event is shared across multiple segments. The equal-energy condition was applied to reject events that were shared across multiple segments. Since the DSSSDs were constructed from a single wafer of silicon, a *real* charged particle event within the silicon will result in a signal of equal size received from both the radial strip and azimuthal sector where the event occurred. Identification of real events from the data was performed by selecting events with equal-energies in the front and rear channels of a DSSSD. The selection was achieved by calculating the energy difference between the front and rear signals, applying an offset to account for negative differences, and gating on events around the offset, thus corresponding to a zero energy difference. An example of an energy-difference spectrum is shown in Figure 6.7. Events within the equal-energy gate were labelled as *good* events and retained for further analysis.

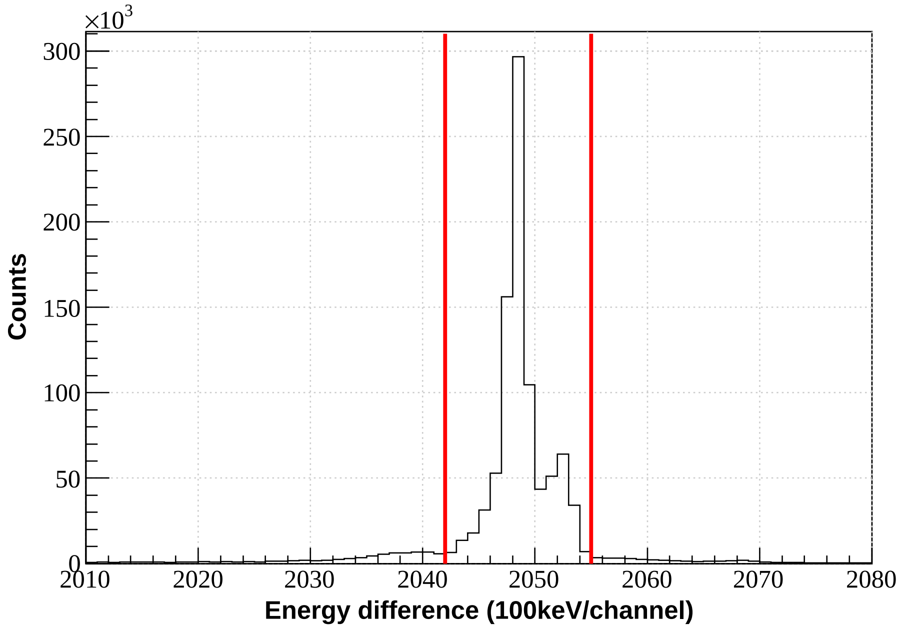

Figure 6.7: *Sample spectrum of the energy difference between events in the front radial strips and rear azimuthal sectors of the S2-ΔE DSSSD. The spectrum is from the 5.476 MeV/A ^{21}Na + 311 μg/cm^2 (CH$_2$)$_n$ run. An offset of 2048 channels was applied to the energy difference. Those counts under the main peak correspond to equal-energy events. An equal-energy gate was set between channels 2042 and 2055.*

6.2.2 ΔE-E Event Selection

Following the selection of *good* events in all the DSSSDs, events that occurred in both the ΔE and E detector of either set of telescopes were extracted. This was achieved by setting a logic statement that an event in any front strip of the ΔE detector and an event in any front strip (or the entire detector in the case of the PAD) of the E detector occurred within the same ADC gate (2 μs). An additional selection requirement was for the ADC event in the ΔE detector to have a corresponding TDC event. If both these requirements were satisfied, the telescope event was labelled as either a *good S2-S2* or *good CD-PAD* event and retained for further analysis.

6.2.3 Particle Identification Mass Gates

The particle identification mass gates were set using the methodology outlined in Section 4.3. Using Equation 4.7, the PI number of the ΔE-E event was calculated; knowing that b = 1.73 for protons and b = 1.65 for carbon ions [56], a value of b = 1.70 was chosen for the identification of ^{4}He ions in the S2-S2 telescope, and a value of b = 1.40 chosen for the identification of ^{18}Ne ions in the CD-PAD telescope. The PI number that is calculated is independent of particle energy and characteristic of the particle mq_{eff}^{2} (where q_{eff} is the rms charge state of the ion, which may or may not be fully stripped of atomic electrons: $q_{\mathrm{eff}} \leq Z$). Typical PI spectra observed throughout the experiment are shown in Figures 6.8 and 6.9; Z=2 ions which are predominantly ^{4}He particles from various reactions on the $(CH_2)_n$ target, including the desired ^{21}Na(p,α)^{18}Ne reaction, were identified as shown in Figure 6.8. The ^{4}He mass gate was set around this Z=2 peak.

In Figure 6.9, the Z=11 peak at PI ~ 2300 is dominated by ^{21}Na ions from Rutherford scattering off the Carbon in the target. In the Z=10 mass region at PI values less than the ^{21}Na peak, there are no discernible peaks that can be attributed to ^{18}Ne ions from the ^{21}Na(p,α)^{18}Ne reaction. Other reactions, such as ^{21}Na(^{12}C,^{20}Ne,^{1}H)3α, produce Z=10 ions which saturate the Z=10 mass region on the PI spectrum and prevents a proper selection of ^{18}Ne particles. Thus, the CD-PAD telescope PI spectrum was re-examined after applying the co-planar two-body and prompt-coincidence cuts, as discussed below.

Even though they are independent of energy, the PI gates were re-examined at each beam energy to ensure they were applied correctly. It was found that at lower beam energies, the width of the PI gates had to be increased compared with the width of gates at the highest beam energy. This was attributed to the increase in energy straggling of the reaction products at the lower beam energies, resulting in broadening of the Z=10 peak. Widening the PI gates accepted more background particles into the gate; this can be observed in the

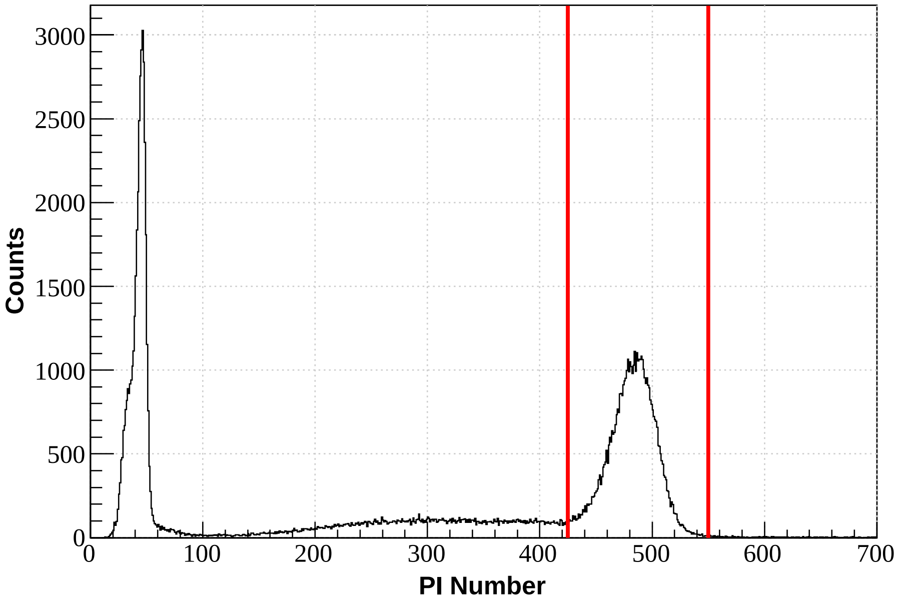

Figure 6.8: *Particle identification spectrum from the S2-S2 ΔE-E telescope. There are two resolved peaks: the proton peak at PI ~ 50, and the ^{4}He ion peak at PI ~ 490. The spectrum is from the 5.476 MeV/A ^{21}Na + 311 μg/cm^2 (CH$_2$)$_n$ measurement. The PI gate for ^{4}He ions was set between channels 425 and 550.*

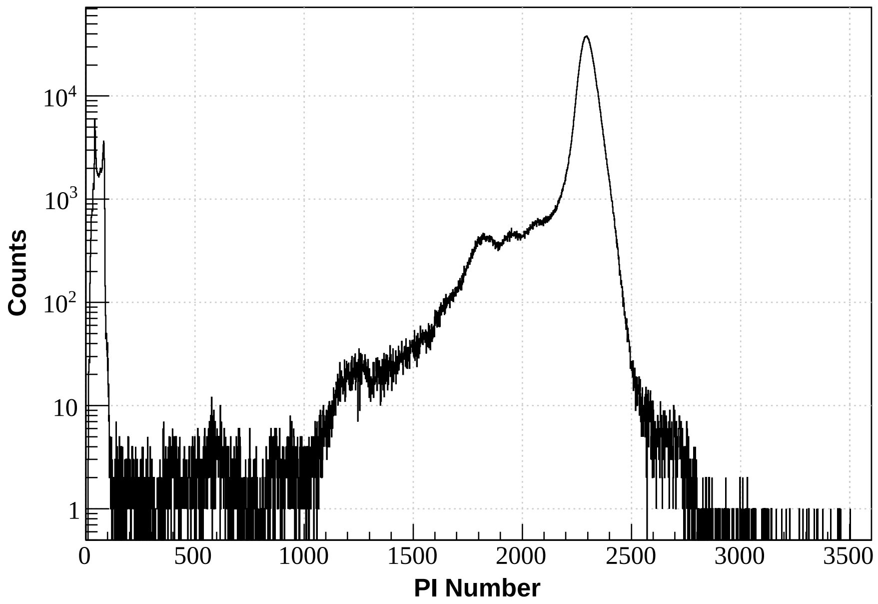

Figure 6.9: *Particle identification spectrum from the CD-PAD ΔE-E telescope. The peak at PI ∼ 2300 is attributed to scattered ^{21}Na ions. The spectrum is from the 5.476 MeV/A ^{21}Na + 311 μg/cm^2 $(CH_2)_n$ measurement.*

spectra presented later in this chapter where there are a greater number of background events at the lower beam energies.

6.2.4 Co-planar Two-body Event Selection

Two-body reaction kinematics confine the reaction products, in the centre of mass frame, to emission angles of 180° with respect to each other, in both the radial (θ) and azimuthal (ϕ) directions. In the laboratory reference frame, the ϕ emission angles remain at 180° with respect to each other. Therefore, two-body reaction events can be extracted by selecting coincident events in the azimuthal sectors of the CD and S2-ΔE detectors that are 180° apart.

For events in the CD and S2-ΔE detectors that occur within the same 2μs ADC acquisition window (this condition provides a *slow* coincidence between events in both detectors), a plot was made of the azimuthal sector in the CD detector against the azimuthal sector in the S2-ΔE detector where the *slow* coincidence events occurred, see Figure 6.10: events that are azimuthally separated by 180° lie on the observed locus. The 5.357 MeV/A ^{21}Ne + 311 μg/cm^2 (CH$_2$)$_n$ run was used to set the co-planar two-body reaction gate for use throughout the experiment: the detectors were not repositioned throughout the experiment and the ^{21}Ne(p,α)^{18}F reaction provided a larger two-body reaction yield to gate on than the ^{21}Na(p,α)^{18}Ne reaction. The locus in Figure 6.10 was gated upon, and the gate used throughout the analysis.

6.2.5 Prompt-coincidence Event Selection

The time-of-flight for an ion is given by Equation 4.8; for the 5.476 MeV/A ^{21}Na + 311 μg/cm^2 (CH$_2$)$_n$ run, ^{18}Ne ions are emitted with energies $E_{\text{lab}} \approx 76$ - 102 MeV and time-of-flight to the CD-PAD telescope of $t \approx 12$ - 10 ns; and ^{4}He ions are emitted with energies E_{lab} 35 - 9 MeV and time-of-flight to the S2-S2 telescope of $t \approx 2.7$ - 4.5 ns (not including energy loss effects). The time difference between a ^{18}Ne event in the CD-PAD telescope and a ^{4}He event in the S2-S2 telescope, given by Equation 4.9, is therefore $\Delta t \approx 9.3$ - 5.5 ns. Events from the ^{21}Na(p,α)^{18}Ne reaction were extracted by selecting events in the CD-PAD and S2-S2 telescopes with the appropriate time difference.

For every *good S2-S2* and *good CD-PAD* event within the same 2μs ADC

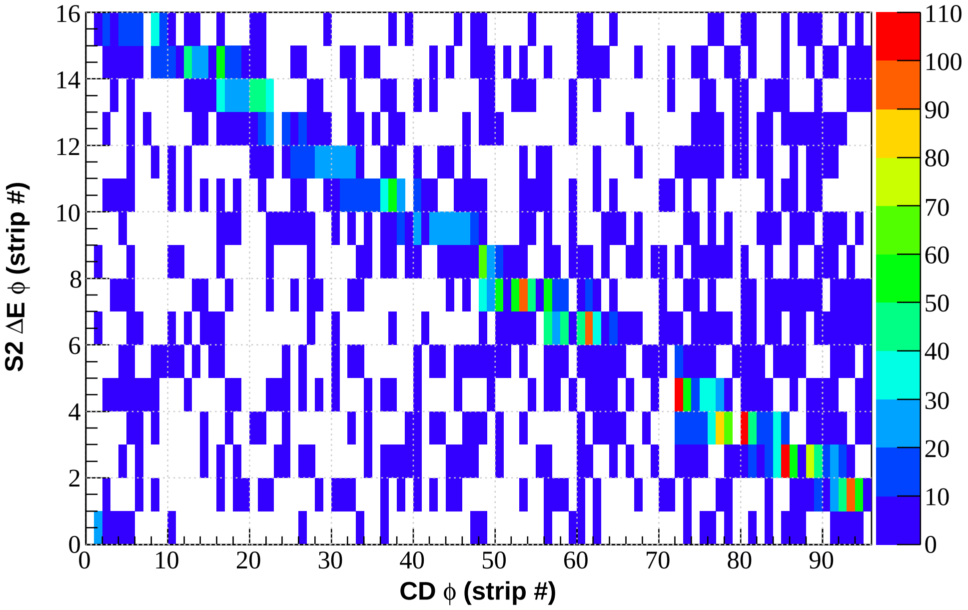

Figure 6.10: *S2-ΔE azimuthal sector vs. CD azimuthal sector plot for events occurring in the same 2μs ADC acquisition window: two-body reaction events are located on the diagonal locus. The spectrum is from the 5.357 MeV/A* ^{21}*Ne + 311 μg/cm*^{2} *(CH*$_2$*)*$_n$ *run.*

window, the TDC values of both events in the S2-ΔE and CD detector were calculated. The S2-ΔE TDC value was subtracted from the CD TDC value and an offset of 2048 channels applied to account for negative values. A sample time difference plot is shown in Figure 6.11. Events under the peak about the time difference corresponding to the ^{21}Na(p,α)^{18}Ne reaction were extracted for further analysis.

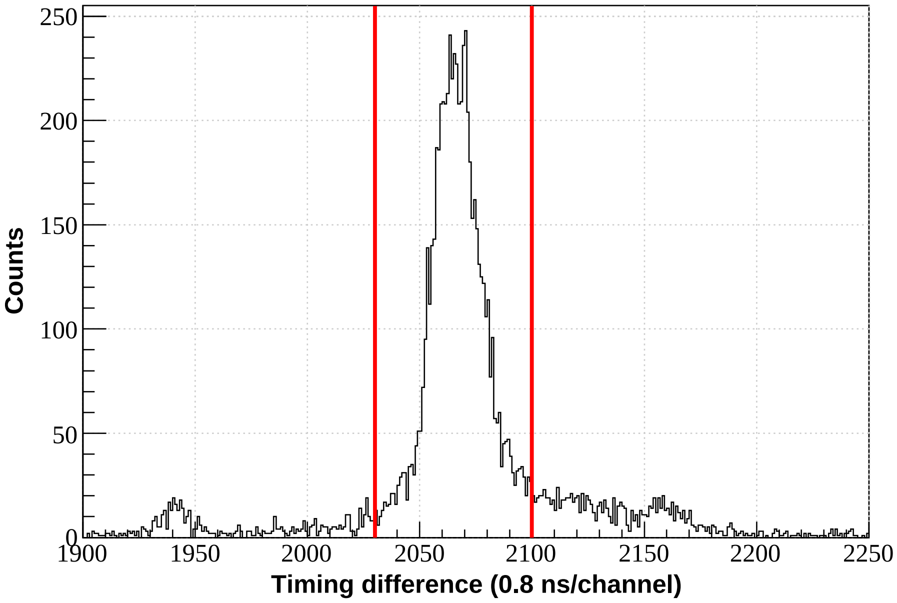

***Figure 6.11**: Sample spectrum of the timing difference (offset by 2048 channels) between events in the S2 ΔE and CD detectors. Counts in the peak around channel 2060 were selected as prompt coincidence events. The spectrum is from the 5.476 MeV/A ^{21}Na + 311 μg/cm^2 $(CH_2)_n$ run.*

To set the Z=10 ^{18}Ne mass gate for the CD-PAD, the co-planar and prompt coincidence conditions were applied to all *good CD-PAD* events. The inclusion of these cuts dramatically reduced the number of background events in the particle identification spectrum. A sample spectrum, from the same measurement as in Figure 6.9, is shown in Figure 6.12. In comparison to Figure 6.9, the majority of Z=11 events are removed and a clearer region of Z=10 particles can be identified and gated upon.

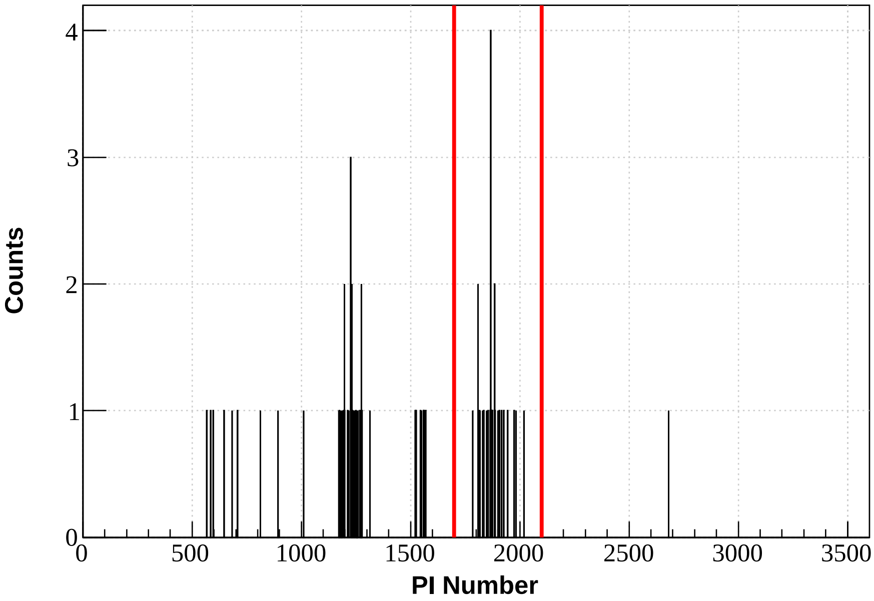

Figure 6.12: *Particle identification spectrum from the CD-PAD ΔE-E telescope with co-planar and prompt coincidence cuts. The majority of background events have been removed, and in comparison with the Z=10 peak in Figure 6.9, a clearer* ^{18}*Ne Z=10 region is identified and gated upon. The spectrum is from the 5.476 MeV/A* ^{21}*Na + 311 μg/cm*^{2} *(CH*$_{2}$*)*$_{n}$ *run.*

Events that satisfied the particle-identification mass gates, co-planar two-body gates and the prompt-coincidence gates were selected from the data and labelled as *candidate* (p,α) events. Given the high yield of background events from contaminant reactions, especially Rutherford scattering off the Carbon in the target, a further series of conditions were applied to the *candidate* (p,α) events. These conditions are listed below and discussed in the following subsections:

- 2D heavy ion Q-value versus ^{4}He Q-value
- 2D heavy ion total energy versus ^{4}He total energy
- ^{4}He kinematic curve
- 1D Sum (heavy ion + ^{4}He) energy

The conditions were applied in series as shown in the flow diagram in Figure 6.13. For each condition, gating on the ^{21}Na(p,α)^{18}Ne locus was found to be a little ambiguous because of the low ^{21}Na(p,α)^{18}Ne cross section; therefore, the Monte-Carlo simulation data was used to aid the positioning and size of the gates and only events that were obvious background events were rejected. To provide confidence in the size of the gates applied, those ^{21}Na(p,α)^{18}Ne events that were selected after the sum (heavy ion + ^{4}He) energy condition were re-examined as shown in the flow diagram in Figure 6.13; beginning with the Q-value versus Q-value condition: the position of the selected ^{21}Na(p,α)^{18}Ne locus was checked to be well within the gate applied, giving confidence that the applied gate was not cutting into the ^{21}Na(p,α)^{18}Ne locus. In the following subsections, each of the four conditions listed above will be discussed; for each condition, spectra will be provided showing the size of the gate applied and the location of the final ^{21}Na(p,α)^{18}Ne locus.

6.2.6 Reaction Q-Value

For every *candidate* (p,α) event, the Q-value of the reaction associated to the ^{4}He ion in the S2-S2 telescope and, separately, to the Z=10 heavy ion in the CD-PAD was calculated by reconstructing the total energies of the particles to an assumed reaction position at the mid-point of the $(CH_2)_n$ target, taking into

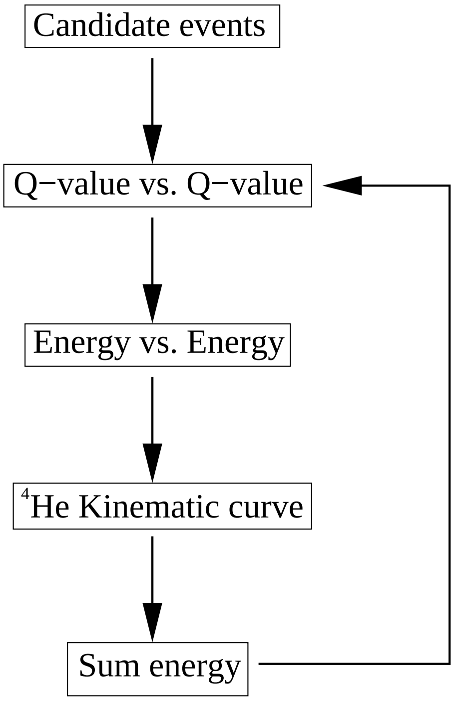

***Figure 6.13**: Flow diagram showing the sequence of conditions applied to the candidate (p,α) events.*

account the energy lost in the detector dead-layers and in the remainder of the target. The equation used to calculate the Q-value is [76]:

$$Q = T_b\left(1 + \frac{m_b}{m_Y}\right) - T_a\left(1 - \frac{m_a}{m_Y}\right) - 2\left(\frac{m_a}{m_Y}\frac{m_b}{m_Y}T_aT_b\right)^{1/2}\cos\theta \tag{6.3}$$

where T_a and m_a are the energy and mass of the ^{21}Na beam respectively, T_b, m_b and θ the energy, mass and angle of the ejectile for which the Q value is being calculated, and m_Y the mass of the recoil nucleus.

The Q-value was calculated for both the ^{4}He and Z=10 ions in the *candidate* (p,α) events, treating each ion as the ejectile in Equation 6.3. 2D plots of ^{4}He Q-value versus Z=10 Q-value for all beam energies are presented in Figure 6.14: both Q-values are offset by +100 channels and the histogram binning used is 100 keV/channel, therefore ^{21}Na(p,α)^{18}Ne events with a Q-value Q = -2.64 MeV are expected about the coordinate (74,74); *candidate* (p,α) events not located about the expected Q-value position arise from random coincidences between ^{4}He and non-^{18}Ne Z=10 ions. The Q-value loci of the selected ^{21}Na(p,α)^{18}Ne events are presented in Figure 6.15.

6.2.7 E(α) versus E(^{18}Ne) locus

Further removal of contaminant reactions from the *candidate* (p,α) events was achieved by plotting the Z=10 heavy ion total ΔE-E energy versus the ^{4}He total ΔE-E energy, presented in Figure 6.16 for all beam energies: two-body reaction kinematics restrict ^{21}Na(p,α)^{18}Ne events to a straight line locus. ^{4}He + Z=10 heavy ion coincidences which are not from the ^{21}Na(p,α)^{18}Ne reaction are not expected to be located on the straight line locus and were excluded from further analysis. Also presented in Figure 6.16 are the 2D gates applied to select the *candidate* (p,α) events, and the Monte-Carlo simulated loci. The final E(α) versus E(^{18}Ne) loci of the selected ^{21}Na(p,α)^{18}Ne events are presented in figure 6.17.

6.2.8 θ(α) versus E(α), Sum ^{4}He+^{18}Ne Energy

Further inspection of the selected (p,α) events was performed by examining the alpha particle's kinematic locus and the measured sum ^{4}He+^{18}Ne energy

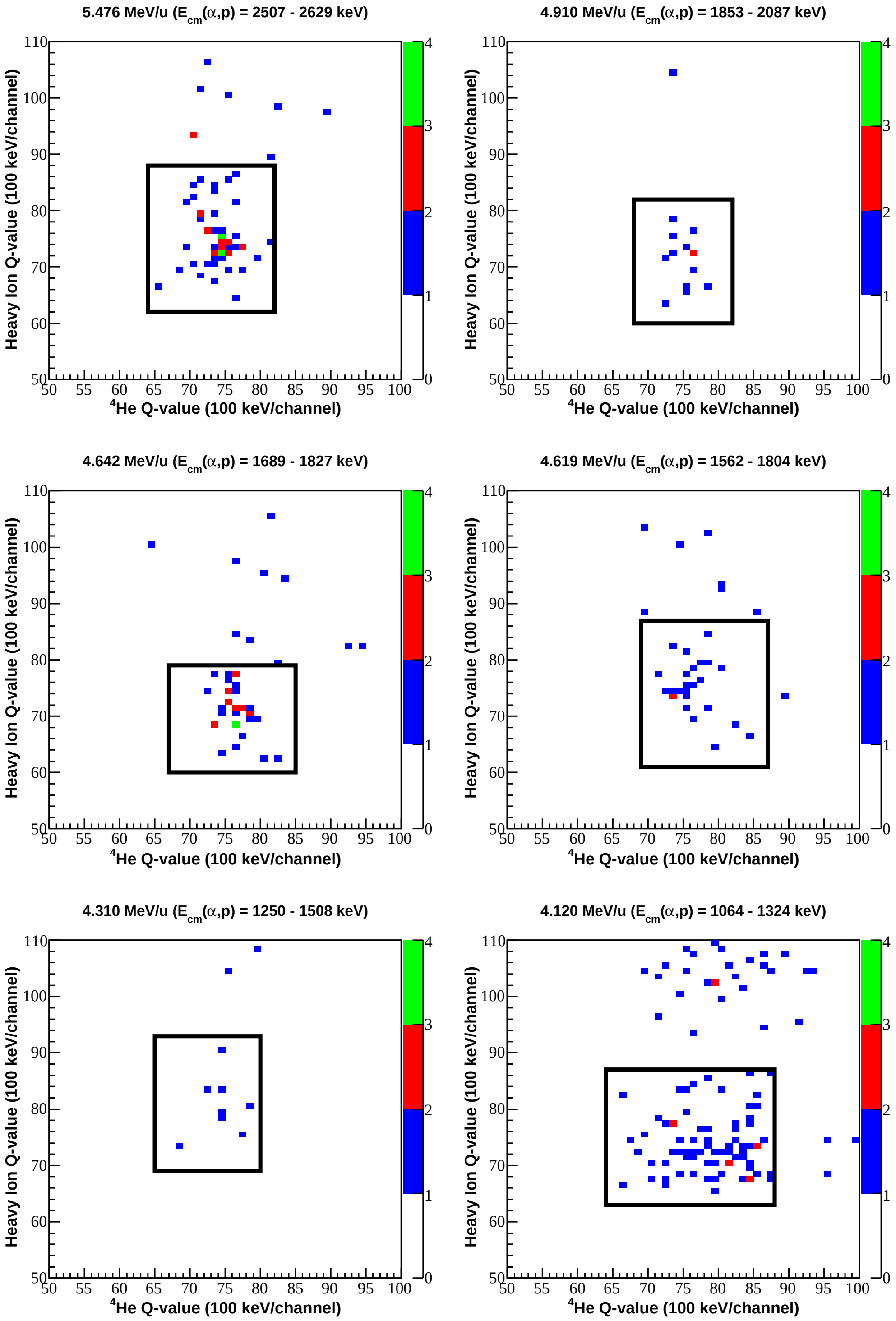

Figure 6.14: 2D Q-value versus Q-value plots for the six energies investigated. The 2D gates applied at each beam energy are shown, and their size is approximately Q ± 1 MeV.

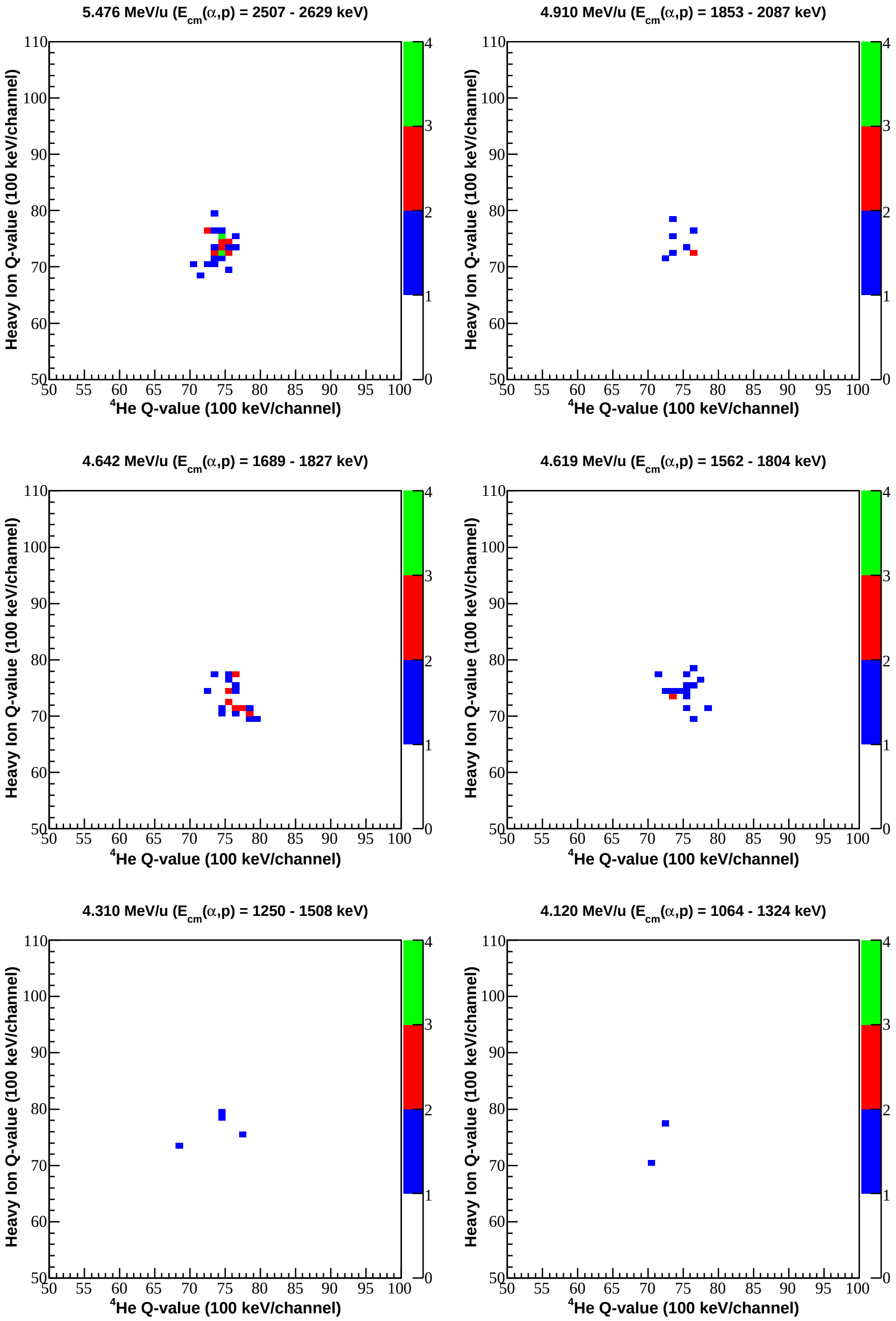

Figure 6.15: 2D Q-value versus Q-value loci of the selected ^{21}Na(p,α)^{18}Ne events at each beam energy.

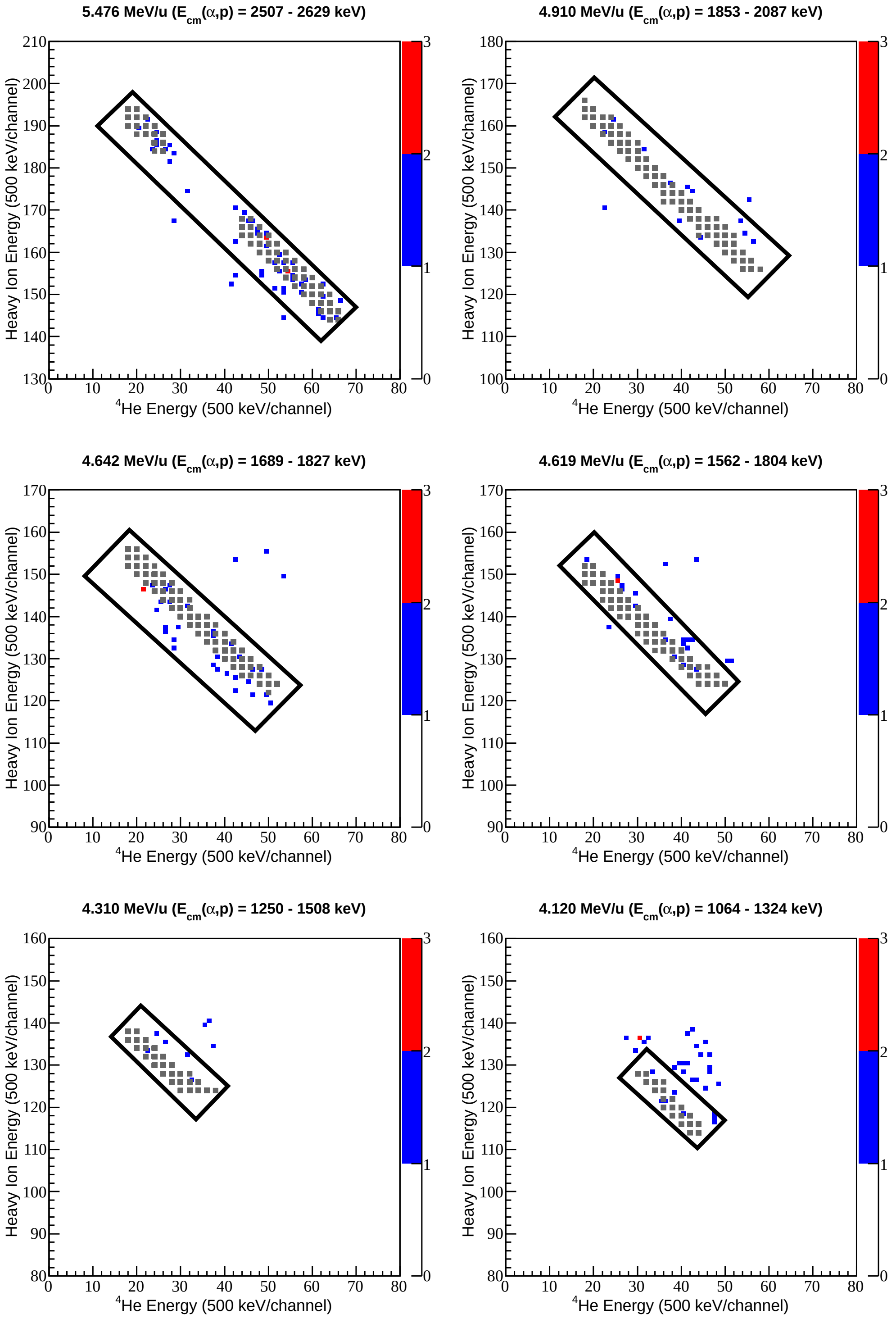

Figure 6.16: *Plots of heavy ion total energy versus ^{4}He total energy for the six energies investigated. The 2D gates applied and the Monte-Carlo simulated loci (grey squares) at each beam energy are also shown.*

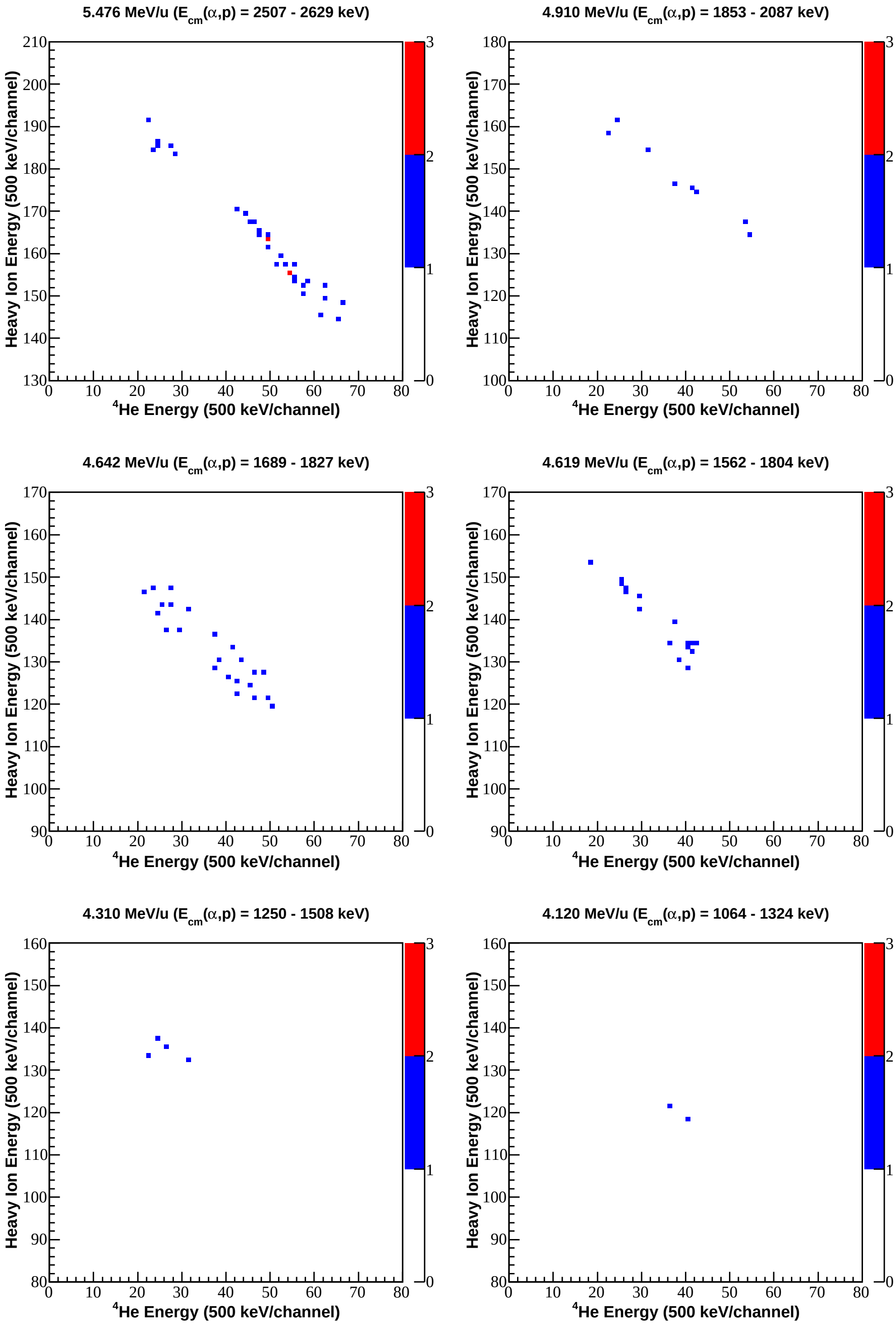

Figure 6.17: *Heavy ion total energy versus ^{4}He total energy loci of the selected ^{21}Na(p,α)^{18}Ne events at each beam energy.*

peak. The alpha particle's kinematic locus was chosen because of the greater angular resolution obtained in the S2-ΔE detector compared to the CD detector. Kinematic loci for all beam energies are presented in Figure 6.18, along with the 2D gates applied and the Monte-Carlo simulated loci. Obvious background events not on the expected kinematic locus were rejected: events were rejected in the 5.467, 4.619 and 4.120 MeV/A measurements; at the remaining beam energies no obvious background rejections could be made; it should be noted that the agreement between the expected kinematic locus and the locus obtained for the E_{beam} = 4.642 MeV/A measurement is not as strong as the agreement found for all the other beam energies (see Section 6.2.9 and Figure 6.18). The measurement at E_{beam} = 4.642 MeV/A was the last energy investigated and it is believed radiation damage of the silicon detectors is responsible for the small discrepancy between the observed and simulated kinematic curves. No events were therefore rejected from the alpha particle kinematic loci at E_{beam} = 4.642 MeV/A. The kinematic loci of the selected ^{21}Na(p,α)^{18}Ne events are presented in Figure 6.19.

The final selection condition came from the measured sum energy of the ^{4}He+^{18}Ne ions. The expected position of the sum energy peak is determined from the calculation: beam energy + Q-value - energy losses in the target & dead-layers (assuming the reaction products are emitted in their ground states). A condition based upon the sum energy of the reaction products allowed for the removal of any remaining contaminant reactions, for example, a random ^{4}He+^{20}Ne coincidence that had failed to be removed by the conditions implemented so far. Experimental sum energy spectra, Monte-Carlo simulated sum energy peaks and the 1D gates applied are presented in Figure 6.20.

Following the application of all conditions discussed in this section and with confidence in the location of all 2D gates, the *candidate* (p,α) events that satisfied all the conditions were selected and labelled as ^{21}Na(p,α)^{18}Ne events. Before the analysis was taken further and the ^{21}Na(p,α)^{18}Ne cross sections calculated, the selected ^{21}Na(p,α)^{18}Ne events were compared to the Monte-Carlo simulation as discussed below.

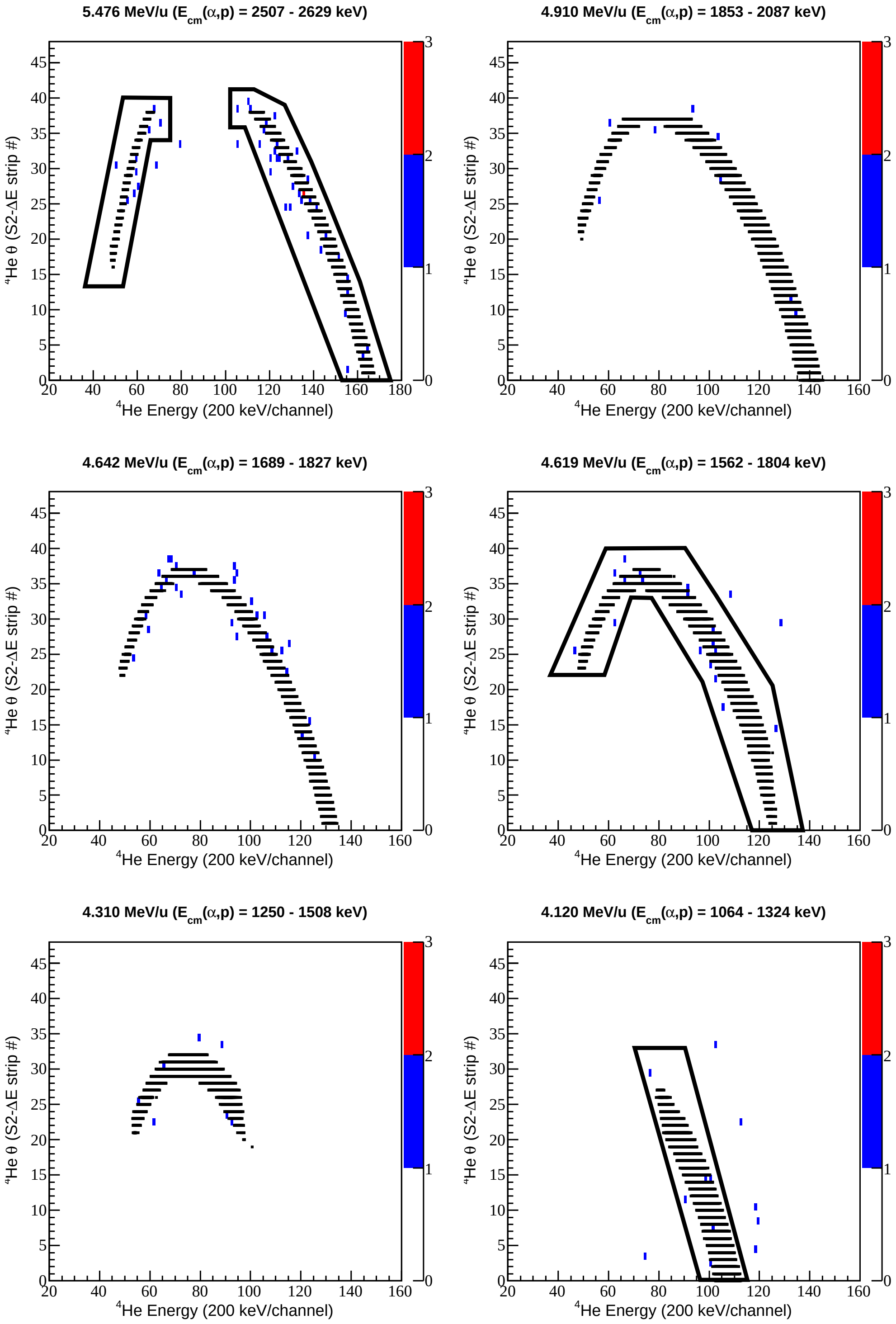

Figure 6.18: *Experimental and Monte-Carlo simulated (black) alpha particle kinematic curves (strip # vs. E) for the six energies investigated. The 2D gates applied at 5.476, 4.619 and 4.120 MeV/A are shown; gates were not applied at the remaining energies because there were no obvious background events to reject.*

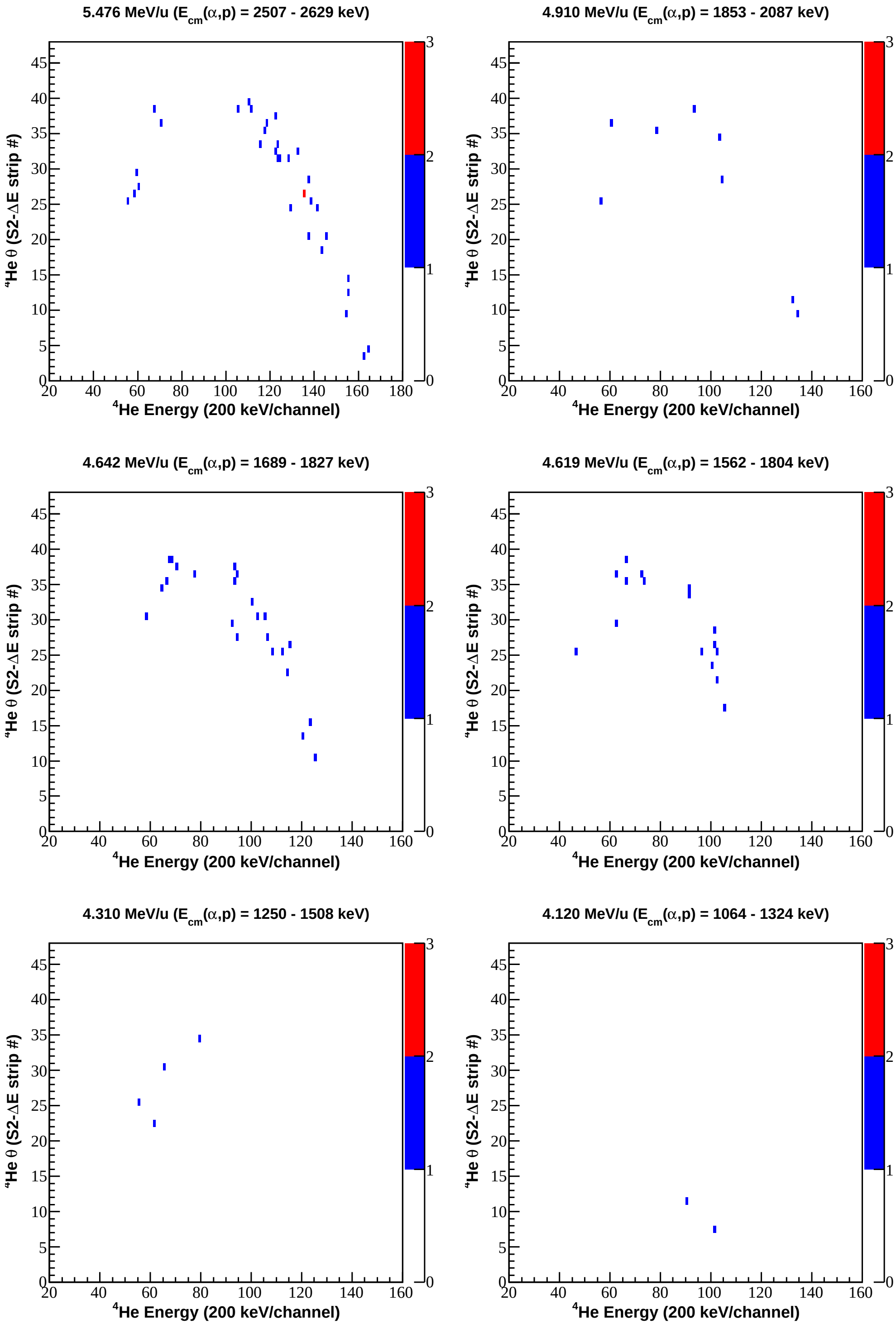

Figure 6.19: *Alpha particle kinematic curves (strip # vs. E) of the selected ^{21}Na(p,α)^{18}Ne events at each beam energy.*

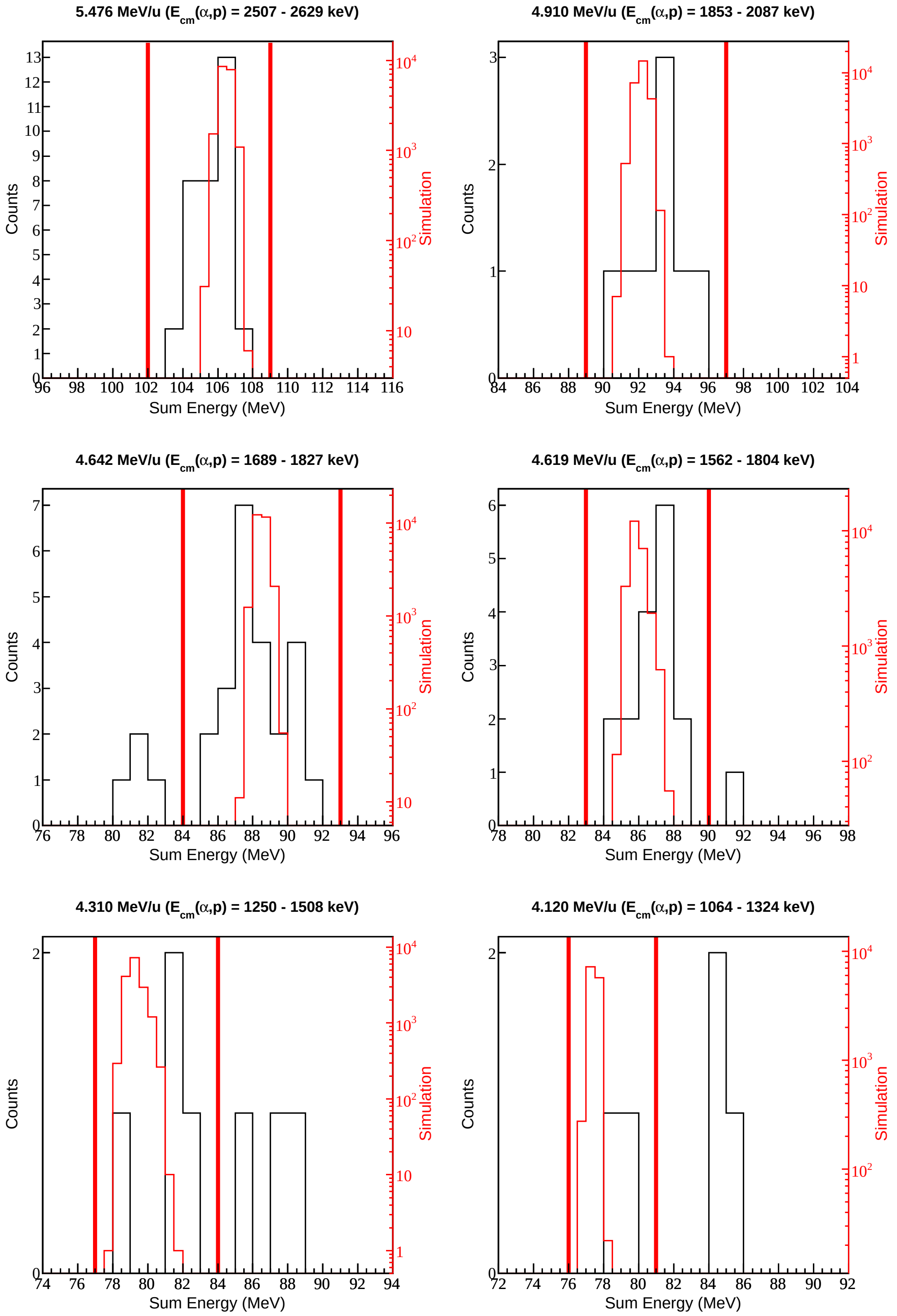

Figure 6.20: *^{4}He + ^{18}Ne sum energy spectra for the six energies the ^{21}Na(p,α)^{18}Ne experiment was performed at. The experimental (black) and Monte-Carlo simulated (thin-red) sum energy peaks and the 1D gates applied (thick-red) are shown.*

6.2.9 Comparison with Simulation

An examination was performed of the consistency in the kinematics of the selected (p,α) events with that expected from simulation; Figures 6.21 - 6.24 present comparisons of the Monte-Carlo simulation data with the extracted (p,α) events.

Before the ^{21}Na + $(CH_2)_n$ data was analysed, the ^{21}Ne + $(CH_2)_n$ data was examined to test the effectiveness of the reaction selection techniques discussed in the previous sections: Figure 6.21 presents kinematic loci and the sum ^{4}He+^{18}F energy peak for the ^{21}Ne(p,α)^{18}F reaction. There is good agreement between the simulated data and extracted (p,α) events; the simulation makes assumptions on the beam spot size and energy losses through detector layers, hence, the experimental loci are expected to have a greater width than the simulated data.

Figures 6.22 and 6.23 present the ^{21}Na(p,α)^{18}Ne alpha particle and ^{18}Ne kinematic loci, respectively, for all six experimental energies. The extracted (p,α) events are consistent with the expected kinematic loci. Figure 6.24 presents the ^{21}Na(p,α)^{18}Ne sum ^{4}He+^{18}Ne energy peak for the six experimental energies. Given the assumptions of the Monte-Carlo simulation mentioned earlier, the experimental sum energy peaks are consistent with the simulated peaks. The consistency between the simulated and experimental data offers confidence in the validity of the approach to extract ^{21}Na(p,α)^{18}Ne events.

For the 5.476 and 4.910 MeV/A measurements, it is possible for the emitted ^{18}Ne ions to be in their first excited state, E_x = 1.89 MeV [77]. However, as shown in Figure 6.25, there is clear separation between the loci for the reaction to the ground state and the reaction to the first excited state at the 5.476 MeV/A beam energy. At 4.910 MeV/A, it is kinematically impossible for ^{18}Ne ions in their first excited state to be detected since the maximum emission angle, $\theta_{\mathrm{lab}}^{\mathrm{max}}$ = 0.8°, is less than the minimum detection angle of the CD-PAD telescope.

The techniques discussed in this section were used to select ^{18}Ne and ^{4}He ions from the ^{21}Na(p,α)^{18}Ne reaction. In the subsection below, the measured ^{21}Na(p,α)^{18}Ne reaction yields from the number of detected ^{18}Ne+^{4}He coincidences are presented. From the measured yield the cross section of the ^{21}Na(p,α)^{18}Ne reaction can be calculated at each beam energy; the remaining

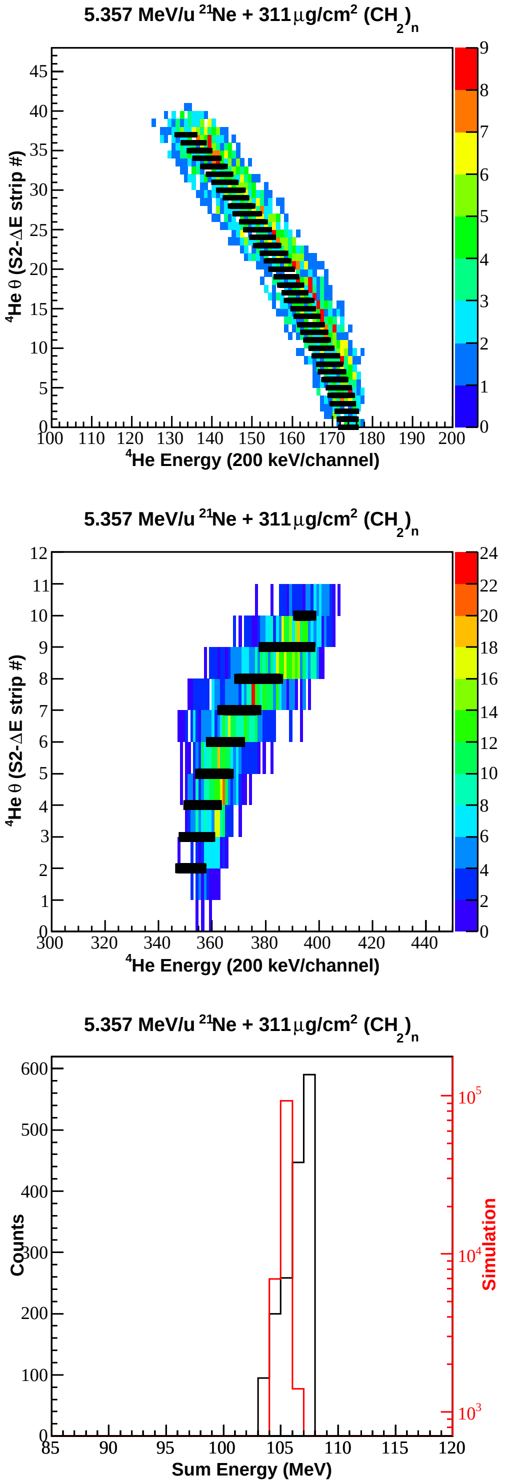

Figure 6.21: *Comparison between simulated and experimental data plots for the ^{21}Ne(p,α)^{18}F reaction: (top) alpha-particle kinematic locus (simulation-black); (middle) ^{18}F kinematic locus (simulation-black); (bottom) sum ^{4}He+^{18}F energy (simulation-red).*

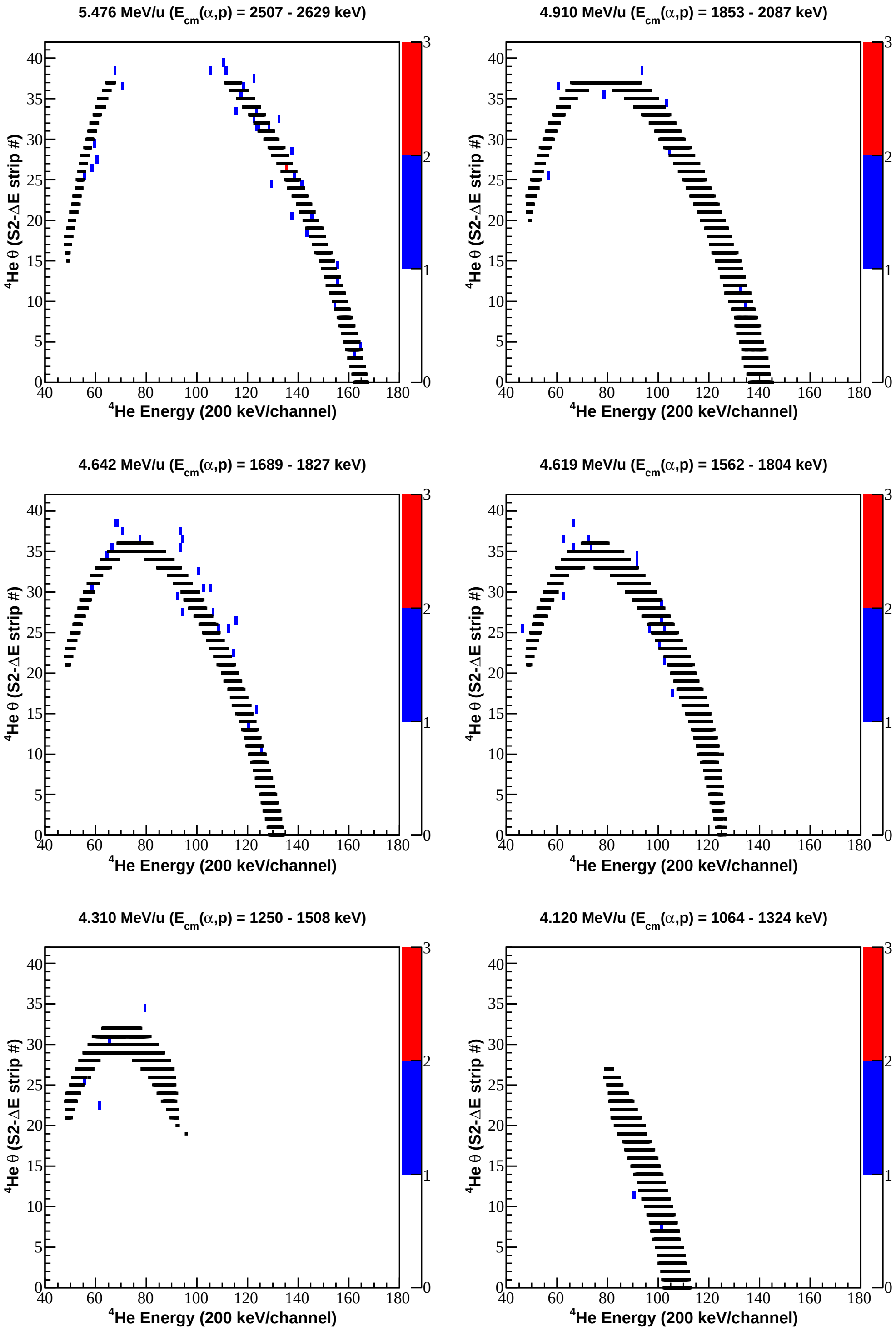

__Figure 6.22:__ Comparison between simulated (in black) and experimental alpha-particle kinematic loci for the six energies the ^{21}Na(p,α)^{18}Ne experiment was performed at.

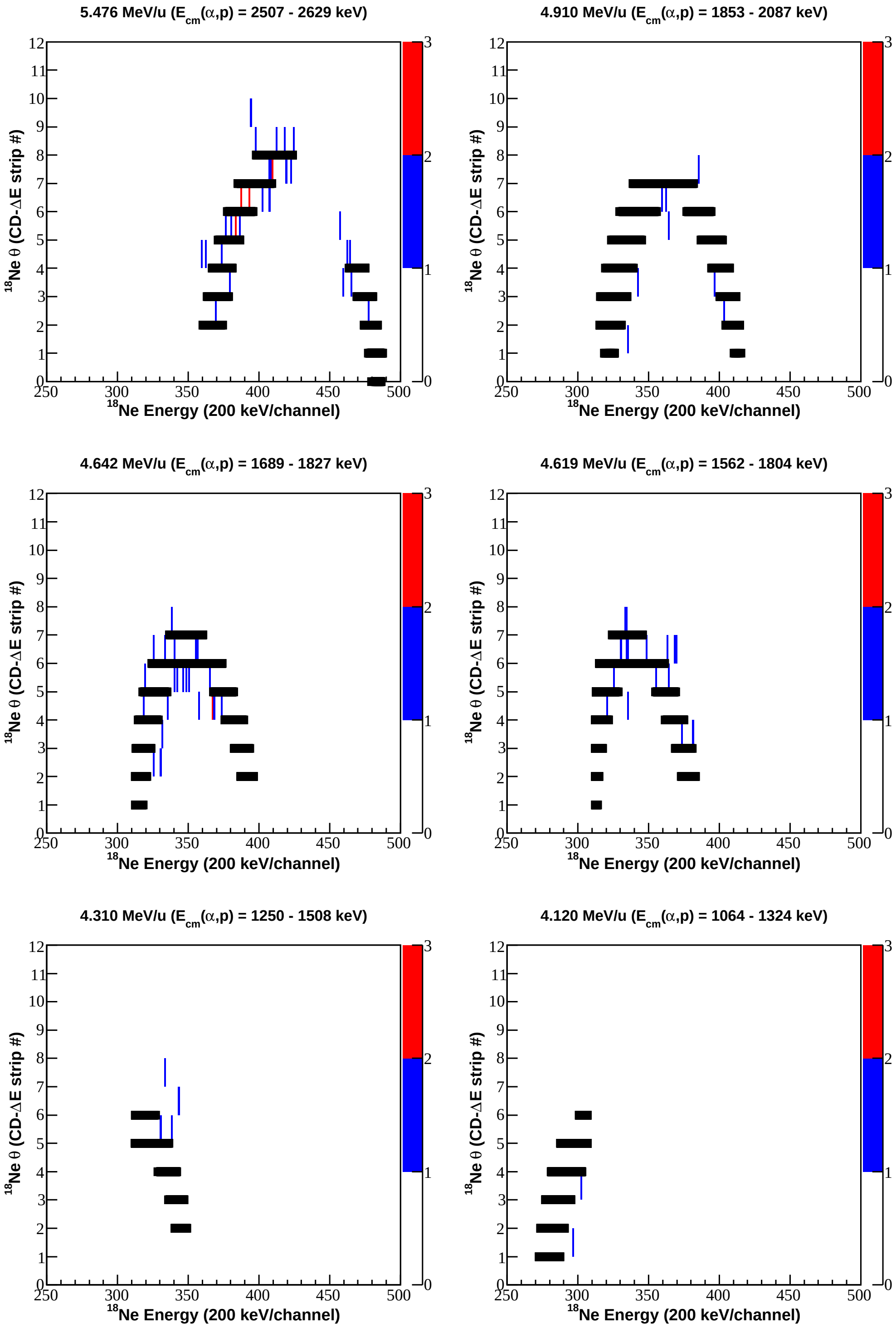

Figure 6.23: *Comparison between simulated (in black) and experimental ^{18}Ne kinematic loci for the six energies the ^{21}Na(p,α)^{18}Ne experiment was performed at.*

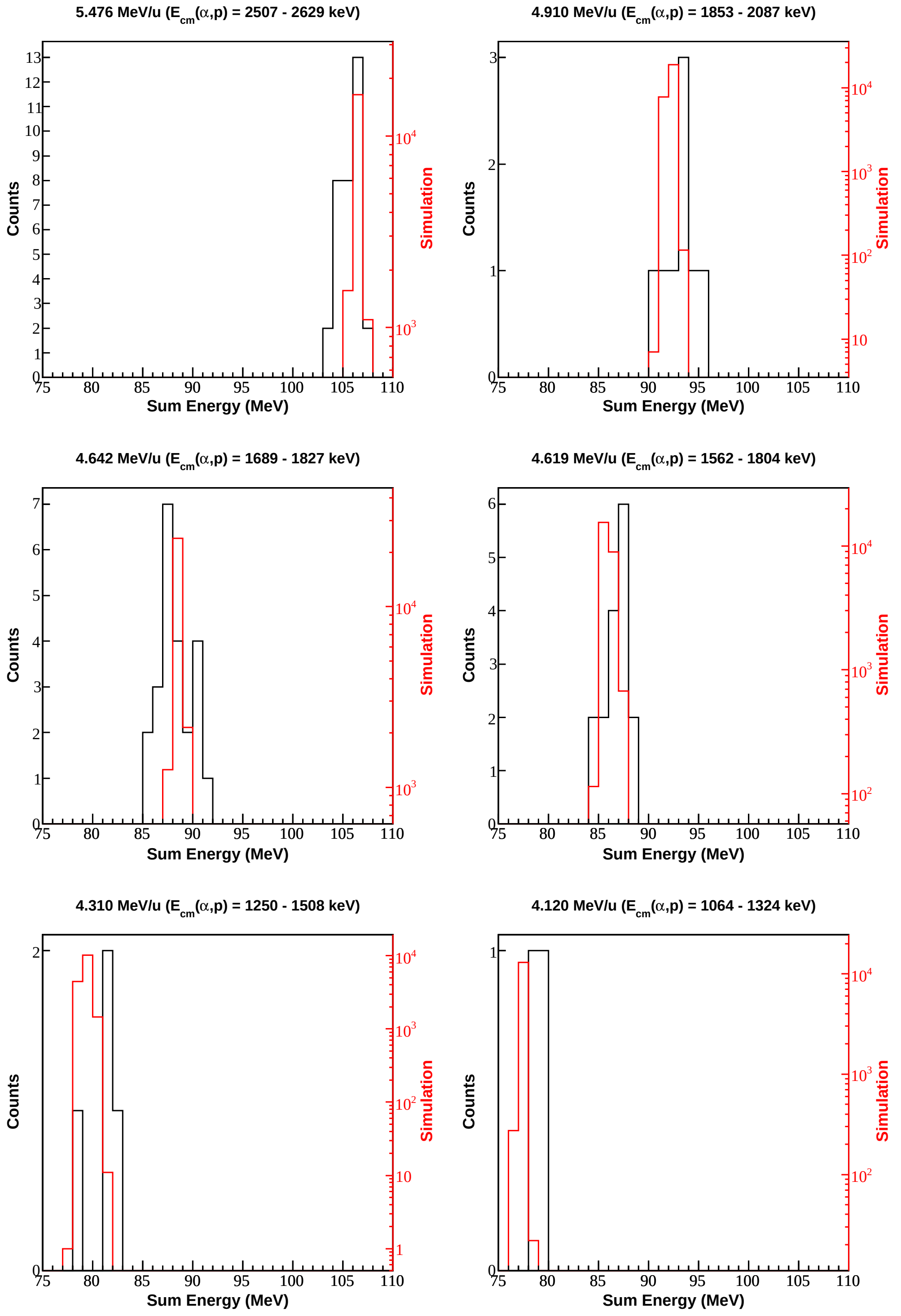

__Figure 6.24:__ Comparison between simulated (red) and experimental (black) sum ^{4}He+^{18}Ne energy peaks for the six energies the ^{21}Na(p,α)^{18}Ne experiment was performed at.

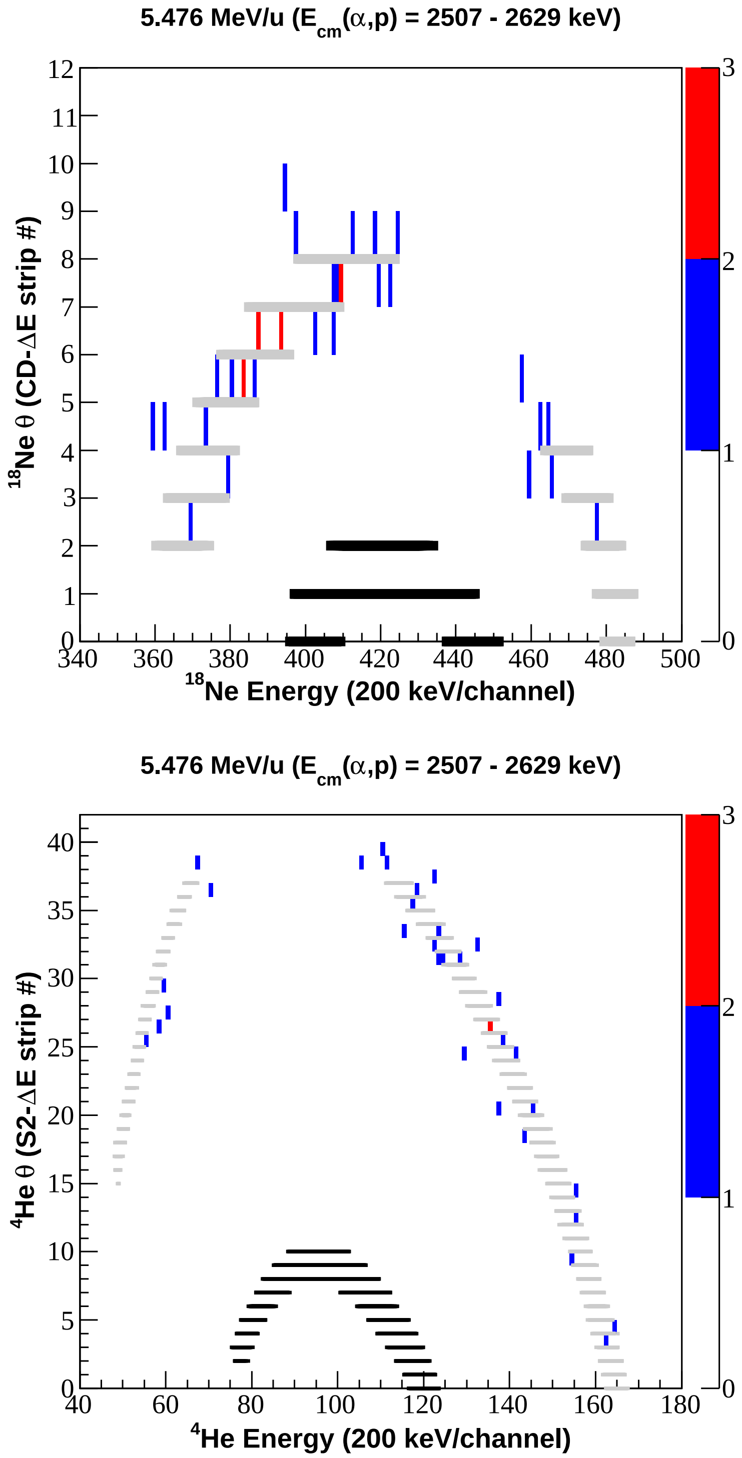

Figure 6.25: *^{18}Ne (top) and alpha-particle (bottom) kinematic loci for the 5.476 MeV/A ^{21}Na + 311 μg/cm^2(CH$_2$)$_n$ run. Both the experimental and simulated loci are shown; the simulated loci for the reaction to the ground state (black) and first excited state (grey) in ^{18}Ne are illustrated.*

sections of this chapter discuss the quantities required to calculate the cross section, followed by the calculation of the ^{21}Na(p,α)^{18}Ne cross section itself, and then the transformation of the cross section from the ^{21}Na(p,α)^{18}Ne direction to the ^{18}Ne(α,p)^{21}Na system.

6.2.10 ^{21}Na(p,α)^{18}Ne Reaction Yields

The ^{21}Na(p,α)^{18}Ne reaction yields for each beam energy are presented in Table 6.2: the errors attributed to the reaction yield are statistical in nature so are treated using Poisson statistics, except for the measurements at E_{beam} = 4.910, 4.619, 4.310 and 4.120 MeV/A where the low statistics warrant the use of the Feldman-Cousins method [78] for error determination, taking the limits at the 68% confidence level and zero background assumption (see Section 6.8).

***Table 6.2**: Measured ^{21}Na(p,α)^{18}Ne reaction yields.*

E_{beam} (MeV)	^{4}He + ^{18}Ne Yield
5.476	33 ± 5.7
4.910	$8\,^{+3.3}_{-2.7}$
4.642	23 ± 4.8
4.619	$16\,^{+4.8}_{-3.7}$
4.310	$4\,^{+2.8}_{-1.7}$
4.120	$2\,^{+2.3}_{-1.3}$

6.3 Target Thicknesses

For a target consisting of a compound, with chemical formula X_aY_b, the number of target nuclei per square centimetre of element X, n_X, and element Y, n_Y, are given by the following equations:

$$n_X = a\, d_{X_aY_b} \frac{N_A}{M_{X_aY_b}} \tag{6.4}$$

$$n_Y = b\, d_{X_aY_b} \frac{N_A}{M_{X_aY_b}} \tag{6.5}$$

where $d_{X_aY_b}$ is the target thickness, in units of g/cm^2, N_A the Avogadro constant, and $M_{X_aY_b}$ the molar mass of compound X_aY_b, in units of g/mol.

For the two $(CH_2)_n$ targets used throughout the experiment, the number of target ^{12}C and ^{1}H nuclei per cm^2 are shown in Table 6.3. Target deterioration was considered a negligible effect since relatively low beam intensities were used throughout the experiment.

Table 6.3: *Number of target nuclei per cm^2 for the two $(CH_2)_n$ targets used throughout the experiment. From the list of available targets in Table 5.2, the 311 μg/cm^2 target was constructed from a sandwich of the 78 (LLN 80) and 233 (LLN 250 #3) μg/cm^2 targets, and the 550 μg/cm^2 target was a sandwich of the 258 (LLN 250 #1) and 292 (LLN 250 #2) μg/cm^2 targets.*

$(CH_2)_n$ Target (μg/cm^2)	^{12}C N_T (/cm^2)	^{1}H N_T (/cm^2)
311	1.34 x10^{19}	2.67 x10^{19}
550	2.36 x10^{19}	4.73 x10^{19}

6.4 DAQ Live-time

Throughout the experiment, the BNC PB-4 pulser generator was connected to the test input of the preamplifier modules of the CD detector, and a suitably attenuated 1Hz signal sent through the DAQ. The live-time of the DAQ was calculated by examining the number of pulses the pulse generator emitted and the number of pulses in a single strip of the CD detector that were recorded, in the following equation:

$$\text{live-time} = \frac{\text{total pulses accepted}}{\text{total pulses presented}} \tag{6.6}$$

The live-time was calculated for each beam energy at which the experiment was performed and was typically 60% throughout the experiment.

6.5 ^{21}Na Beam Intensity Measurements

The ^{21}Na beam intensity was determined by measuring the ^{21}Na yield from ^{12}C(^{21}Na,^{21}Na)^{12}C Rutherford scattering because the beam intensity measurement from the Faraday cup mounted on the rear of the TUDA chamber was observed to be erratic and unreliable.

It is important that the selected ^{21}Na ions used for the beam intensity measurement have undergone Rutherford scattering in the target. For ^{12}C(^{21}Na,^{21}Na)^{12}C scattering at beam energies of E_{beam} = 5.476 - 4.120 MeV/A, the corresponding ^{21}Na+^{12}C centre of mass bombarding energies of E_{cm} = 41.3 - 30.4 MeV are well above the height of the ^{21}Na+^{12}C Coulomb barrier of E_c = 12.0 MeV. Under these conditions, the *grazing* angles for Rutherford scattering are $\theta_{gr}^{lab} = 7.1^\circ$ at E_{beam} = 5.476 MeV/A, to $\theta_{gr}^{lab} = 10.3^\circ$ at E_{beam} = 4.120 MeV/A (see Appendix C for a more detailed discussion of Rutherford scattering). Selection of scattered ^{21}Na ions within the *grazing* angle ensured the scattering mechanism was Rutherford.

The laboratory differential cross section for ^{12}C(^{21}Na,^{21}Na)^{12}C Rutherford scattering is given by the equation [76]:

$$\left(\frac{d\sigma}{d\Omega}\right)_{lab} = \left(\frac{zZe^2}{4\pi\epsilon_0}\right)^2 \left(\frac{1}{4T_{lab}}\right)^2 \frac{1}{\sin^4\frac{\theta_{lab}}{2}} \tag{6.7}$$

where z and Z are the atomic numbers of the projectile and target respectively, e the electron charge, T_{lab} the projectile energy, and θ_{lab} the scattering angle. The Rutherford differential cross section can also be calculated in the centre-of-mass frame, provided all the variables are in the centre-of-mass reference frame.

At the highest beam energy, E_{beam} = 5.476 MeV/A, the ^{12}C(^{21}Na,^{21}Na)^{12}C Rutherford differential cross section and stopping power vary by 4.8% and 1.4% respectively over a target thickness of Δ_{cm} = 969 keV (311 μg/cm^2). Likewise, at the lowest beam energy, E_{beam} = 4.120 MeV/A, the ^{12}C(^{21}Na,^{21}Na)^{12}C Rutherford differential cross section and stopping power vary by 14% and 4.2% respectively over a target thickness of Δ_{cm} = 2.1 MeV (550 μg/cm^2). Since the differential cross section varied by 14% over the target thickness for the lowest beam energy, the effective beam energy was calculated with Equation 4.14 and it was found to be very close to the beam energy at mid-target. A thin target treatment was therefore applied for ^{12}C(^{21}Na,^{21}Na)^{12}C Rutherford scattering at all beam energies.

For a thin target, Equation 4.12 can be re-arranged to give the number of projectiles, N_P, responsible for a detected reaction yield, N_R:

$$N_P = \frac{N_R}{N_T \frac{d\sigma}{d\Omega} \Delta\Omega \tau} \tag{6.8}$$

where N_T is the number of target ^{12}C nuclei, $d\sigma/d\Omega$ the reaction differential cross section at the mean effective energy in the target ($E_{\text{eff}} = E_0$ - $\Delta E/2$, where E_0 is the beam energy and ΔE the energy loss over the target), $\Delta\Omega$ the geometrical solid angle of the detectors from the target, and τ the live-time of the data acquisition system.

^{21}Na ions from ^{12}C(^{21}Na,^{21}Na)^{12}C Rutherford scattering were extracted from the inner most ring of the CD detectors in the CD-PAD telescope, corresponding to an angular range of θ_{lab} = 1.49 - 1.80°. The effective lab angle ($\theta^{eff}_{\text{lab}}$) of the Rutherford scattering was determined by calculating the lab angle corresponding to half the area underneath the $d\sigma/d\Omega$ curve for the angular range of the strip (θ_{lab} = 1.49 - 1.80°). For all beam energies the Rutherford effective lab angle was determined to be $\theta^{eff}_{\text{lab}}$ = 1.62°. The ^{21}Na ions were selected using the particle identification mass gate technique discussed in Section 6.2.3; a 2D plot of CD-PAD energy versus PI number was made, as shown in Figure 6.26: the ^{12}C(^{21}Na,^{21}Na)^{12}C Rutherford scattering locus is easily identifiable and is selected.

The solid angle of the inner most CD ring was calculated using Equation 6.9:

$$\Omega \;=\; \int_{\phi_1}^{\phi_2} d\phi \int_{\theta_2}^{\theta_1} \sin\theta \; d\theta \;=\; (\phi_2 - \phi_1)(\cos\theta_1 - \cos\theta_2) \tag{6.9}$$

where θ_1 and θ_2 are the inner and outer angles from the target of the innermost CD strip, and $(\phi_2 - \phi_1)$ is the azimuthal angular range of the ring, in the laboratory frame. The measured beam intensities are shown in Table 6.4.

6.6 Experimental Efficiencies

The efficiencies of coincident ^{4}He+^{18}Ne detection for the experimental setup were calculated using the Monte-Carlo simulation discussed in Section 5.5; the efficiencies calculated for each measurement and for isotropic and non-isotropic angular distributions are shown in Table 6.5: there are deviations

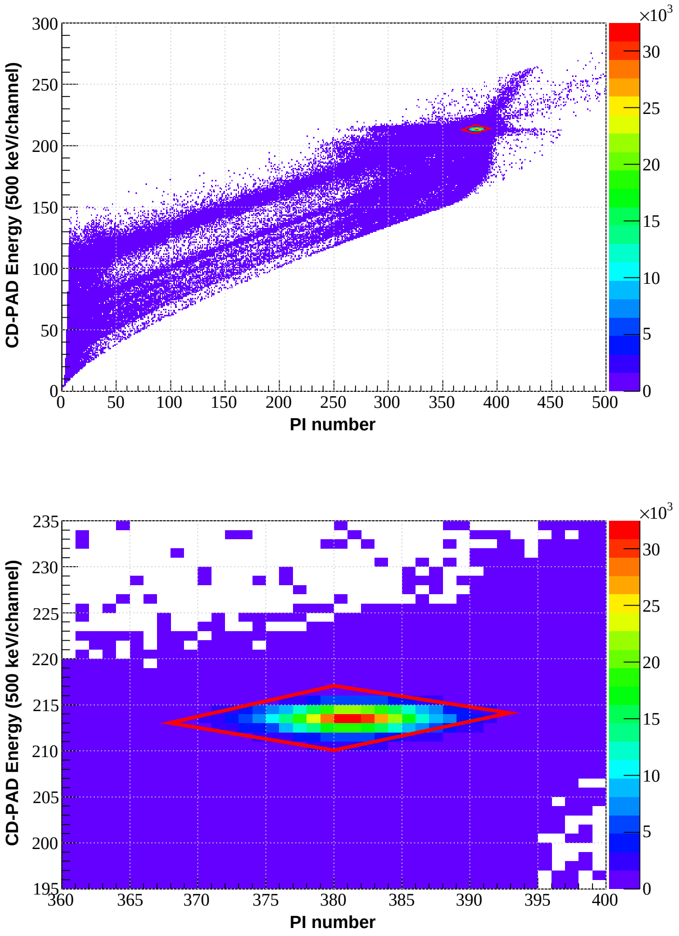

Figure 6.26: *CD-PAD energy versus PI number for the 5.476 MeV/A ^{21}Na + 311 μg/cm^2 (CH$_2$)$_n$ measurement. (Top) Plot of all events in the CD-PAD telescope; (bottom) ^{12}C(^{21}Na,^{21}Na)^{12}C Rutherford scattering locus.*

from the isotropic (l=0) detection efficiency of at most 21% at the highest beam energy to 54-56% at the two lowest beam energies. Since it is uncertain which angular distribution to use, the ^{21}Na(p,α)^{18}Ne reaction was assumed to be isotropic in the centre of mass, and the deviations in the detection efficiency for non-isotropic angular distributions treated as systematic uncertainties in the detection efficiency.

During the analysis, it was noticed that one of the QQQ/2 quadrants appeared to behave differently to the other three QQQ/2 quadrants that make up the CD detector. It was determined the quadrant was much thicker than the other three quadrants and could not be used in the ΔE-E telescope since heavy

Table 6.4: *Measured ^{21}Na beam intensities. The error on the beam intensity is discussed in Section 6.8.*

Beam Energy (MeV/A)	N_P (particles)
5.476	$(2.9 \pm 0.3)\times10^{10}$
4.910	$(3.2 \pm 0.3)\times10^{10}$
4.642	$(7.1 \pm 0.7)\times10^{11}$
4.619	$(5.0 \pm 0.5)\times10^{11}$
4.310	$(1.5 \pm 0.1)\times10^{12}$
4.120	$(6.9 \pm 0.7)\times10^{12}$

ions did not penetrate it, so it was left out of the data analysis. The removal of one of the QQQ/2 quadrants from the analysis resulted in a decrease in the efficiency (l=0) of the coincident ^{4}He+^{18}Ne detection of -7.5% (absolute value) at E_{beam} = 5.476 MeV/A to -4.7% (absolute value) at E_{beam} = 4.120 MeV/A.

Table 6.5: *Monte-Carlo simulation efficiency results for coincident ^{4}He (S2-S2 telescope) and ^{18}Ne (CD-PAD telescope) detection. The coincident detection efficiency is calculated for isotropic (l=0) and non-isotropic (l=1 to l=3) angular distributions.*

Beam Energy	Coincident Efficiency (ζ) (%)			
(MeV/A)	$l = 0$	$l = 1$	$l = 2$	$l = 3$
5.476	19.0	22.8	21.1	15.3
4.910	26.6	28.8	20.7	25.6
4.642	27.3	29.1	20.4	26.9
4.619	25.2	25.4	15.4	24.8
4.310	16.1	12.0	6.8	19.6
4.120	13.3	19.6	10.9	9.3

6.7 ^{18}Ne(α,p)^{21}Na Cross Section Determination

The cross section for the ^{21}Na(p,α)^{18}Ne reaction was calculated using the following equation:

$$\sigma(E_{\mathrm{eff}}) = \frac{N_R}{N_P N_T \zeta \tau} \qquad (6.10)$$

where N_R is the measured ^{21}Na(p,α)^{18}Ne yield, N_P the total number of beam particles, N_T the number of target ^{1}H nuclei per unit area in the $(CH_2)_n$ target, ζ the calculated coincident detection efficiency given the θ and ϕ geometry of the setup and energy loss effects through the detector dead-layers[2], and τ the DAQ live-time.

For the finite target thicknesses used in this experiment, the ^{21}Na(p,α)^{18}Ne cross section is expected to vary across the target. However, the approach taken in this work does not enable the distinction of contributions to the cross section from resonant or non-resonant mechanisms. Therefore, the cross sections calculated here are based on a major assumption that the cross section is approximately constant over the target thickness. A thin target treatment was applied and the mean effective energy taken as the beam energy at the mid-target position. The error given to each mean effective energy is not an error as such, but a limit on the energy that can be associated with the cross section. The measured ^{21}Na(p,α)^{18}Ne yields and associated cross sections are shown in Table 6.6.

Table 6.6: *Measured yields and associated cross sections of the ^{21}Na(p,α)^{18}Ne reaction. The errors on the yield and cross section presented here are statistical only and are discussed in Section 6.8.*

E_{beam} (MeV/A)	E^{cm}_{eff}(p,α) (keV)	^{4}He + ^{18}Ne Yield	σ(p,α) (mb)
5.476	5205 ± 61	33 ± 5.7	0.35 ± 0.06
4.910	4608 ± 117	$8^{+3.3}_{-2.7}$	$\left(3.0^{+1.2}_{-1.0}\right) \times 10^{-2}$
4.642	4395 ± 69	23 ± 4.8	$(5.3 \pm 1.1) \times 10^{-3}$
4.619	4320 ± 121	$16^{+4.8}_{-3.7}$	$\left(3.8^{+1.1}_{-0.9}\right) \times 10^{-3}$
4.310	4016 ± 129	$4^{+2.8}_{-1.7}$	$\left(5.6^{+3.9}_{-2.3}\right) \times 10^{-4}$
4.120	3832 ± 130	$2^{+2.3}_{-1.3}$	$\left(7.4^{+8.3}_{-4.6}\right) \times 10^{-5}$

---

[2] To take into account ions that were stopped in the detector dead-layers.

6.7.1 ^{18}Ne(α,p)^{21}Na Cross Section

The ^{18}Ne(α,p)^{21}Na cross sections were calculated using Equation 4.4:

$$\sigma_{^{18}Ne(\alpha,p)^{21}Na} = \sigma_{^{21}Na(p,\alpha)18Ne} \frac{m_p m_{^{21}Na}}{m_\alpha m_{^{18}Ne}} \frac{E^{cm}_{p^{21}Na}}{E^{cm}_{\alpha^{18}Ne}} \frac{(2j_p+1)(2j_{^{21}Na}+1)}{(2j_\alpha+1)(2j_{^{18}Ne}+1)} \tag{6.11}$$

with m(p) = 1.007276 *amu* (1 *amu* = 931.494 MeV/c^2), j(p) = 1/2, m(^{21}Na) = 20.997655 *amu*, j(^{21}Na) = 3/2, m(^{4}He) = 4.002700 *amu*, j(^{4}He) = 0, m(^{18}Ne) = 18.005710 *amu*, j(^{18}Ne) = 0, and

$$E^{\text{cm}}_{\alpha^{18}Ne} = E^{\text{cm}}_{p^{21}Na} - |\text{Q}| \tag{6.12}$$

where Q = 2.6373 MeV for the ^{18}Ne(α,p)^{21}Na reaction.

The calculated ^{18}Ne(α,p)^{21}Na cross sections are given in Table 6.7, and plotted as a function of centre-of-mass energy in Figure 6.27: the centre of mass energies correspond to an estimated interaction energy at the mid-point of the $(CH_2)_n$ target and the x-axis error bars in Figure 6.27 reflect half the target thickness.

Table 6.7: *Calculated ^{18}Ne(α,p)^{21}Na total cross sections. The errors on the cross section are statistical only and are discussed in Section 6.8.*

$E^{cm}_{\text{eff}}(\alpha,p)$ (keV)	$\sigma(\alpha,p)$ (mb)
2568 ± 61	1.7 ± 0.3
1970 ± 117	$0.17^{+0.07}_{-0.06}$
1758 ± 69	$(3.1 \pm 0.6) \times 10^{-2}$
1683 ± 121	$\left(2.3^{+0.7}_{-0.5}\right) \times 10^{-2}$
1379 ± 129	$\left(3.8^{+2.7}_{-1.6}\right) \times 10^{-3}$
1194 ± 130	$\left(5.5^{+6.2}_{-3.5}\right) \times 10^{-4}$

6.8 Error Evaluation

This section will outline the sources of statistical and systematic errors in the calculated cross sections, and include estimates of the total magnitude where appropriate. It will also discuss the contribution to the uncertainty from the

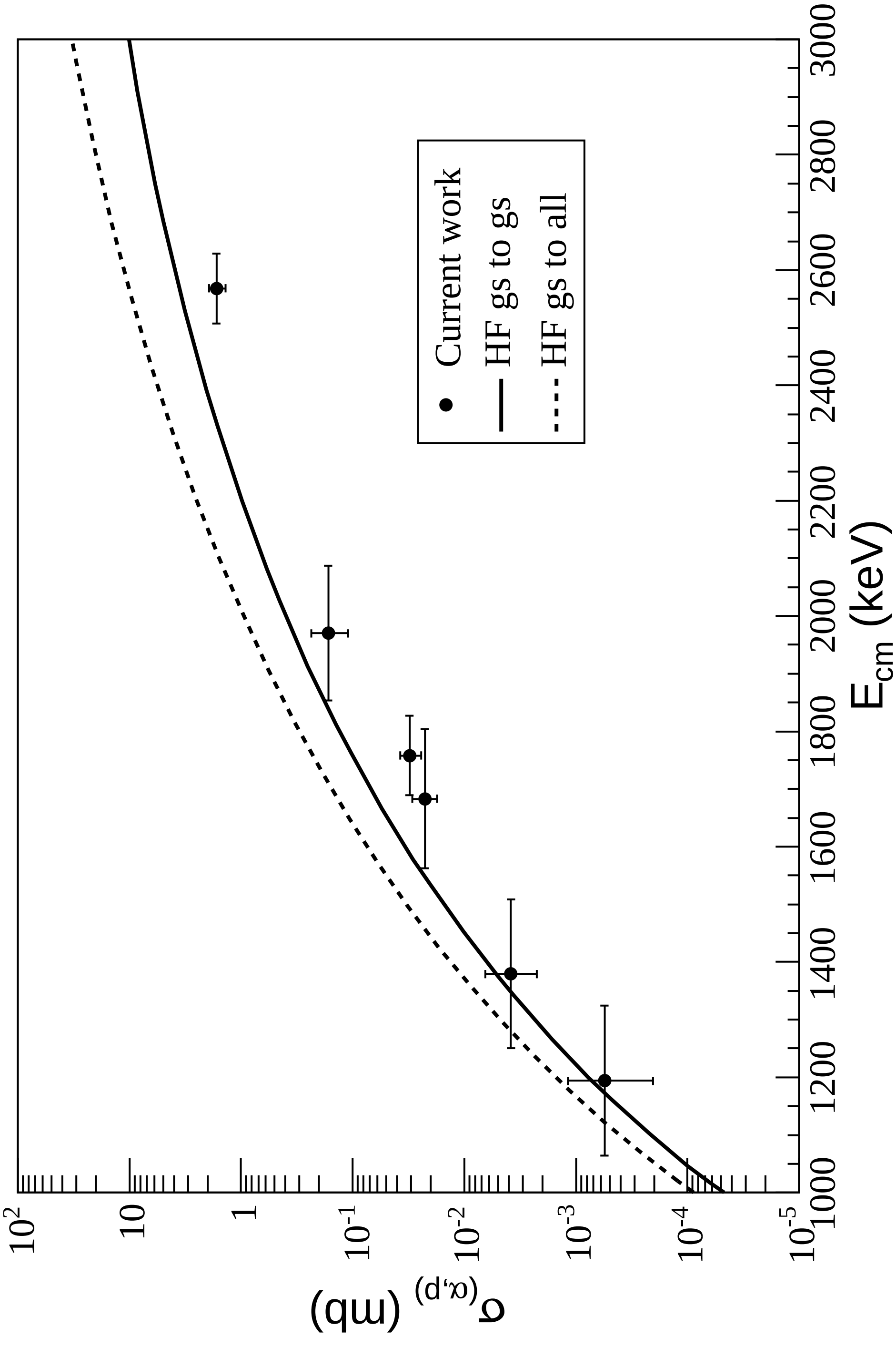

Figure 6.27: *^{18}Ne(α,p)^{21}Na cross section as a function of* $E_{cm}^{(\alpha,p)}$ $\left[= E_{cm}^{(p,\alpha)} - |Q|\right]$.

efficiencies of non-isotropic angular distributions.

6.8.1 Statistical Uncertainty

The dominant contribution to the total error, and the one presented with the cross sections in Tables 6.6 & 6.7 and the cross section plots in Figures 6.27 & 7.1, arises from the statistical error in the ^{21}Na(p,α)^{18}Ne reaction yield. For the 5.476 and 4.642 MeV/A measurements, the error in the yield is given as $\Delta N_R = \sqrt{N_R}$; and for the low reaction yields of the 4.910, 4.619, 4.310 and 4.120 MeV/A measurements, the error in the yield is determined using the more appropriate approach of the Feldman-Cousins [78] method for low statistics, taking the limits at the 68% confidence level and zero background assumption. The zero background assumption was justified by applying all cuts used in the ^{21}Na(p,α)^{18}Ne analysis to the ^{21}Na + $(CD_2)_n$ data taken at each beam energy; no ^{21}Na + $(CD_2)_n$ events survived the cuts applied[3] and a zero background was therefore justified. Table 6.8 shows the statistical error on the ^{4}He+^{18}Ne yield and both (p,α) and (α,p) cross sections for each beam energy. Also shown is the error on the effective centre-of-mass interaction energy, E_{cm}^{eff}, which represents half the thickness of the $(CH_2)_n$ target used, as discussed in Section 6.7.

6.8.2 Systematic Uncertainty

The systematic uncertainty in the cross section is dominated by the uncertainties in the measured target thicknesses and in the ^{21}Na beam intensity. These are discussed in more detail below.

Measurements of the $(CH_2)_n$ target thicknesses are discussed in Section 5.2.2 and the method used is described in Appendix A: the thickness measurements are dominated by the systematic error attributed to energy loss calculations with SRIM-2008; the other sources of error in the identification of the mixed-alpha source peak centroid position and the systematic uncertainty in the target surface density are considered negligible. The systematic error in the target thickness is estimated as 8%.

---

[3] The Q-value for the ^{21}Na(d,α)^{19}Ne reaction is Q = 6.776 MeV, so the reaction products are kinematically separate from the ^{21}Na(p,α)^{18}Ne reaction.

***Table 6.8*:** *Summary of the statistical error estimated for each cross section measurement; the statistical error arises from the ^{4}He+^{18}Ne yield, see text. The error on E_{cm}^{eff} represents half the thickness of the $(CH_2)_n$ target used.*

E_{beam} (MeV/A)	E_{cm}^{eff} (p,α) (MeV)	E_{cm}^{eff}(α,p) (MeV)	^{4}He+^{18}Ne Yield	σ(p,α) (mb)	σ(α,p) (mb)	$\Delta\sigma$ (%) [statistical]
5.476[a]	5.21±0.06	2.57±0.06	33±6	0.3±0.1	1.7±0.3	±17
4.910[b]	4.61±0.12	1.97±0.12	$8^{+3.3}_{-2.7}$	$\left(3.0^{+1.2}_{-1.0}\right)\times10^{-2}$	$0.17^{+0.07}_{-0.06}$	$^{+42}_{-34}$
4.642[a]	4.40±0.07	1.76±0.07	23±5	$(5.3 \pm 1.1)\times10^{-3}$	$(3.1 \pm 0.6)\times10^{-2}$	±21
4.619[b]	4.32±0.12	1.68±0.12	16^{+5}_{-4}	$\left(3.8^{+1.1}_{-0.9}\right)\times10^{-3}$	$\left(2.3^{+0.7}_{-0.5}\right)\times10^{-2}$	$^{+30}_{-23}$
4.310[b]	4.02±0.13	1.38±0.13	4^{+3}_{-2}	$\left(5.6^{+3.9}_{-2.3}\right)\times10^{-4}$	$\left(3.8^{+2.7}_{-1.6}\right)\times10^{-3}$	$^{+70}_{-42}$
4.120[b]	3.83±0.13	1.19±0.13	$2^{+2.3}_{-1.3}$	$\left(7.4^{+8.3}_{-4.6}\right)\times10^{-5}$	$\left(5.5^{+6.2}_{-3.5}\right)\times10^{-4}$	$^{+113}_{-63}$

[a] 311μg/cm^2 $(CH_2)_n$ target
[b] 550μg/cm^2 $(CH_2)_n$ target

The ^{21}Na beam intensity was calculated according to Equation 6.13:

$$N_P = \frac{N_R}{N_T \frac{d\sigma}{d\Omega} \Delta\Omega \tau} \tag{6.13}$$

and uncertainty in the value arises from four sources of error: the statistical error in the ^{12}C(^{21}Na,^{21}Na)^{12}C Rutherford yield, treated using Poisson statistics as $\Delta N_R = \sqrt{N_R}$; the error in the number of target ^{12}C nuclei, as discussed above; the error in the solid angle of the detector geometry, determined as 1.3% by estimating the systematic error in the positioning of each detector as ±1mm; and the statistical error in the number of pulses presented and pulses accepted for determination of the DAQ live-time, given as:

$$\Delta\tau \; = \; \frac{\sqrt{\text{pulses accepted}}}{\text{pulses presented}} \tag{6.14}$$

The error in the DAQ live-time was typically 0.5% and therefore considered negligible in the error calculation. Since each of the three remaining sources of error are independent of one another, they were added in quadrature:

$$\frac{\Delta N_P}{N_P} \; = \; \left[\left(\frac{\Delta N_R}{N_R} \right)^2 + \left(\frac{\Delta N_T}{N_T} \right)^2 + \left(\frac{\Delta[\Delta\Omega]}{\Delta\Omega} \right)^2 \right]^{\frac{1}{2}} \tag{6.15}$$

$\frac{\Delta N_P}{N_P}$ values were typically 8% for all beam energies and are dominated by the error in the target thickness.

The uncertainty in the coincident detection efficiency, ζ, due to a ±1mm error in the measurement of the geometry of the detector arrangement was considered negligible with respect to the other sources of systematic uncertainty. The Monte-Carlo simulations were re-run with simulated positions varied by ±1mm. The effect on the efficiency was a 0.2% variation and thus negligible.

A systematic uncertainty, which has not been accounted for in the error evaluation but will be highlighted here, is the uncertainty in the positioning of the gates discussed earlier in this chapter. The positioning of the gates was aided by the Monte-Carlo calculations, and there is, therefore, a systematic uncertainty from the position of these simulated loci. This uncertainty can be estimated by varying the input parameters of the Monte-Carlo simulation by their individual quantities of uncertainty, and hence vary the boundary conditions of the gates, and observe how the data fractional acceptance changes.

To obtain the total systematic uncertainty the non-independent contributions from the beam intensity and target thickness measurements were summed, resulting in a value of 16% systematic uncertainty for each measurement; this error is less than the statistical uncertainty at all beam energies. A summary of the systematic contributions is given in Table 6.10.

6.8.3 Efficiencies for non-isotropic angular distributions

The efficiency of coincident ^{4}He+^{18}Ne detection was calculated assuming the ^{21}Na(p,α)^{18}Ne reaction has an isotropic angular distribution in the centre-of-mass. This assumption is valid since the angular distribution of the ^{21}Na(p,α)^{18}Ne reaction is unknown, however, it is important to investigate the affect of non-isotropic angular distributions on the detection efficiency and hence the measured cross section.

Detection efficiencies for $l = 1$ to $l = 3$ angular distributions[4] were calculated using the Monte-Carlo simulation, see Section 5.5; the results of the calculations are shown in Section 6.6 and again in Table 6.9 below. Deviations from the isotropic efficiency are as large as 21% at E_{beam} = 5.476 MeV/A to 54-56% at the two lowest beam energies; the maximum deviation of non-isotropic efficiencies from the isotropic efficiency are shown in Table 6.9 for each beam energy. These deviations in the detection efficiency are comparable to, or smaller than, the reaction yield statistical uncertainties given in Table 6.8, and can be treated as an additional systematic uncertainty.

A summary of all contributions to the systematic uncertainty in the cross section measurements is given in Table 6.10.

Table 6.11 shows the uncertainty in the cross section measurements from all dominant statistical and systematic contributions.

---

[4] Efficiencies for angular distributions beyond l=3 were ignored because of their low probability of occurring.

Table 6.9: *Coincident ^{4}He+^{18}Ne detection efficiencies for l=0 to l=3 angular distributions. Also shown is the maximum deviation of the non-isotropic efficiencies from the isotropic case.*

E_{beam}	Coincident Efficiency (%)				% deviation
(MeV/A)	$l = 0$	$l = 1$	$l = 2$	$l = 3$	from $l = 0$
5.476	19	23	21	15	21 (l = 1,3)
4.910	27	29	21	26	22 (l = 2)
4.642	27	29	20	27	26 (l = 2)
4.619	25	25	15	25	40 (l = 2)
4.310	16	12	7	20	56 (l = 2)
4.120	13	20	11	9	54 (l = 1)

***Table 6.10**: Summary of the systematic contributions to the uncertainty for each cross section measurement. The solid angle ($\Delta\Omega$), DAQ live-time ($\Delta\tau$) and efficiency ($\Delta\zeta$ [geometry]) contributions were considered negligible. The non-independent target thickness (ΔN_T) and beam intensity (ΔN_P) contributions were summed to obtain a systematic uncertainty of 16%, which is to be taken into account with the systematic uncertainty arising from the non-isotropic deviations in the detection efficiency ($\Delta\zeta$ [non-isotropic]).*

E_{beam} (MeV/A)	$\sigma(\alpha,p)$ (mb)	$\frac{\Delta N_T}{N_T}$ (%)	$\frac{\Delta N_P}{N_P}$ (%)	$\frac{\Delta[\Delta\Omega]}{\Delta\Omega}$ (%)	$\frac{\Delta\tau}{\tau}$ (%)	$\Delta\zeta/\zeta$ (%) [geometry]	$\Delta\zeta/\zeta$ (%) [non-isotropic]
5.476	1.7	8.0	8.1	1.3	0.5	0.2	21
4.910	0.17	8.0	8.1	1.3	0.5	0.2	22
4.642	3.1×10^{-2}	8.0	8.1	1.3	0.5	0.2	26
4.619	2.3×10^{-2}	8.0	8.1	1.3	0.5	0.2	40
4.310	3.8×10^{-3}	8.0	8.1	1.3	0.5	0.2	56
4.120	5.5×10^{-4}	8.0	8.1	1.3	0.5	0.2	54

Table 6.11: *Summary of the % uncertainties for each cross section measurement. The statistical uncertainty arises from the ^{4}He+^{18}Ne yield; the systematic uncertainty is dominated by the uncertainty in the measured target thicknesses and in the ^{21}Na beam intensity (summed to give ±16%), and the effect of non-isotropic angular distributions on the detection efficiency.*

E_{beam} (MeV/A)	$\sigma(\alpha,p)$ (mb)	$\Delta\sigma$ (%) [statistical]	$\Delta\sigma$ (%) [systematic]	$\Delta\sigma$ (%) [non-isotropic]
5.476	1.7	±17	±16	±21
4.910	0.17	$^{+42}_{-34}$	±16	±22
4.642	3.1×10^{-2}	±21	±16	±26
4.619	2.3×10^{-2}	$^{+30}_{-23}$	±16	±40
4.310	3.8×10^{-3}	$^{+70}_{-42}$	±16	±56
4.120	5.5×10^{-4}	$^{+113}_{-63}$	±16	±54

Chapter 7

Results and Discussion

The aim of this work was three-fold: a) to perform a time-reverse measurement of the ^{18}Ne(α,p)^{21}Na cross section in as wide an energy region as possible and down to the lowest energy feasible; b) to test the validity of the Hauser-Feshbach statistical model for the calculation of the ^{18}Ne(α,p)^{21}Na cross section; and c) to perform a comparison with previous ANL time-reverse measurements.

In this chapter the cross sections measured in this work are compared with the Hauser-Feshbach calculation and the ANL measurements of the ^{18}Ne(α,p)^{21}Na cross section, and the differences between the data sets are discussed. Using the measured cross sections, the ^{18}Ne(α,p)^{21}Na reaction rate is calculated and compared with previous estimates, and the astrophysical implications of the rate discussed.

7.1 Cross Section Comparisons

The cross sections measured in this work are presented in Figure 7.1 together with the NON-SMOKER Hauser-Feshbach (HF) calculations of the cross section for ground-state to ground-state and ground-state to all state transitions [46,54] and the unpublished cross sections measured in the ANL experiment [42].

In comparison with the ANL cross section measurements, there is an overall good agreement with the cross sections measured in this work, except perhaps in the energy region E_{cm} = 1600 - 1800 keV.

In comparison with the NON-SMOKER HF calculations, Figure 7.1 shows, surprisingly, that the two lowest data points at E_{cm} = 1379 and 1194 keV are in agreement with the HF_{gs}[1] calculation. However, the remaining measurements at higher energies are up to a factor 2 lower than the HF_{gs} calculation; this is contrary to expectations, as lower energies correspond to lower excitation energies, and therefore lower level densities, in the compound nucleus where one expects the HF formalism to fail. The reason for the discrepancy between our data and the HF_{gs} calculation is unclear, but it would suggest that the level density of natural parity states in ^{22}Mg is smaller than is assumed by the HF calculation. Thus, it appears that the HF statistical model is not appropriate for calculation of the ^{18}Ne(α,p)^{21}Na cross section, and caution should be used with the application of the formalism for nuclei in this mass region. In fact, it has been reported by Deibel *et al.* [79] in their recent investigation of the ^{33}Cl(p,α)^{30}S reaction that the compound nucleus ^{34}Ar is at the limit of the region where the Hauser-Feshbach statistical model can be applied.

7.2 ^{18}Ne(α,p)^{21}Na Reaction Rate

Calculation of the ^{18}Ne(α,p)^{21}Na reaction rate was performed by numerical integration of Equation 2.11:

$$< \sigma v > = \left(\frac{8}{\pi\mu}\right)^{\frac{1}{2}} \frac{1}{(kT)^{\frac{3}{2}}} \int_0^\infty S(E)exp\left(-\frac{E}{kT} - 2\pi\eta\right)dE$$

with the *exp2rate* Fortran code written by T. Rauscher [80]: using the experimental results calculated as astrophysical S(E)-factors (see Equation 2.10), the code used a cubic spline interpolation to fit functions to both the upper and lower limit of the S-factor, taking into account the S-factor and $E_{cm}(\alpha$,p) error bars associated with each data point. The numerical integration was then performed using the upper and lower S(E)-factor limits over the centre-of-mass energy range E_{cm} = 1194 - 2568 keV to give upper and lower reaction rate limits. The results of the calculations are presented in Table 7.1: the upper and lower limits of the reaction rate and the arithmetic mean between the limits are given. The calculated reaction rate for the temperature interval T = 0.95 - 2.45 GK is

---

[1] From herein, HF_{gs} refers to ground-state to ground-state transitions, and HF_{all} refers to ground-state to all transitions.

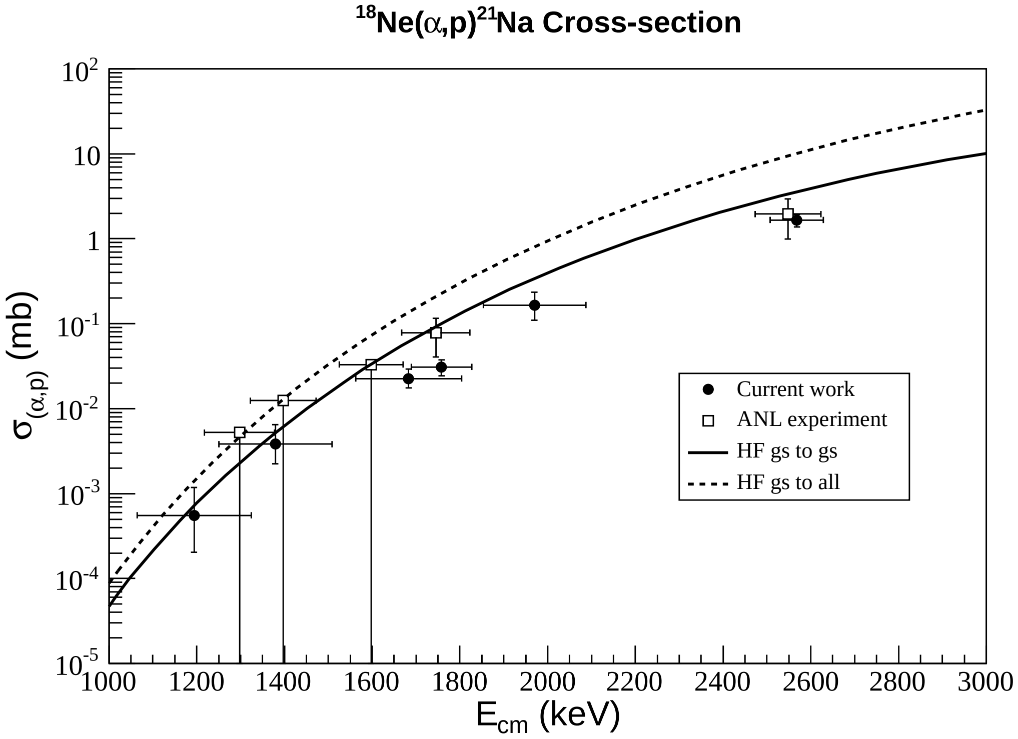

Figure 7.1: *Measured* ^{18}*Ne(*α*,p)*^{21}*Na cross sections (filled circles) as a function of* $E_{cm}^{dir.}$. *For comparison, the ANL 2004 [42] results (open squares) and HF calculations (solid line: ground-state to ground-state; dotted line: ground-state to all states) [46,54] are also shown.*

shown in Figure 7.2. The most recent calculation by Matić *et al.* [34] and the HF_{gs} and HF_{all} calculations [46, 54] are also presented for comparison. The reaction rate calculated in this work is a factor 2-3 lower than the HF_{gs} calculations, and is 1-1.5 orders of magnitude lower than the Matić *et al.* [34] reaction rate. A possible reason for the discrepancy between the Matić *et al.* rate and this work is that the reaction rate determined in this work represents lower limits of the rate since the time-reverse technique only connects the ground states of ^{21}Na and ^{18}Ne, but it is questionable whether this would result in such a large discrepancy. Matić *et al.* [34] used the ^{24}Mg(p,t)^{22}Mg reaction to populate and identify states in ^{22}Mg, and calculated the ^{18}Ne(α,p)^{21}Na reaction rate using the resonance parameters obtained, or where there was no experimental information, the resonance parameters were estimated. Uncertainties in the reaction rate reported in the Ph.D. thesis of A. Matić [81] are attributed to the presence of unknown states in ^{22}Mg that can significantly contribute to the rate (the observed level density of the mirror ^{22}Ne is larger than that of ^{22}Mg above the ^{18}Ne+^{4}He threshold); incorrect spin assignments; unknown resonance parameters and inaccurately measured resonance energies.

The ^{18}Ne(α,p)^{21}Na reaction rate calculated over the temperature range T = 0.1 - 10 GK is shown in Figure 7.3. However, outside the temperature range T = 0.95 - 2.45 GK the reaction rate has to be extrapolated from the cubic spline interpolation since there is no experimental data, and therefore the reliability of the calculated rate drastically decreases, especially for T < 0.95 GK.

As far as astrophysical implications of our new rate are concerned, the effect of our ^{18}Ne(α,p)^{21}Na reaction rate on the nucleosynthesis in Type-I X-ray bursts is estimated to be small [82]. Hydrodynamical models of Type I X-ray bursts, [83], currently use the ^{18}Ne(α,p)^{21}Na reaction rate given by Chen *et. al.* [21], which agrees to a factor ~3 with the SMOKER Hauser Feshbach calculation [26]. Lowering the ^{18}Ne(α,p)^{21}Na reaction rate in these X-ray burst models by a factor 2.5 has shown there is a less than 1-2% change in the energy production and some minor increases in isotope abundances, see Table 7.2. Current theoretical investigations [83] have predicted that only a factor 10 increase in the ^{18}Ne(α,p)^{21}Na rate has an effect on the overall nucleosynthesis and energy production of an X-ray burst. However, this does not diminish the potential importance of the ^{18}Ne(α,p)^{21}Na reaction with respect to the breakout

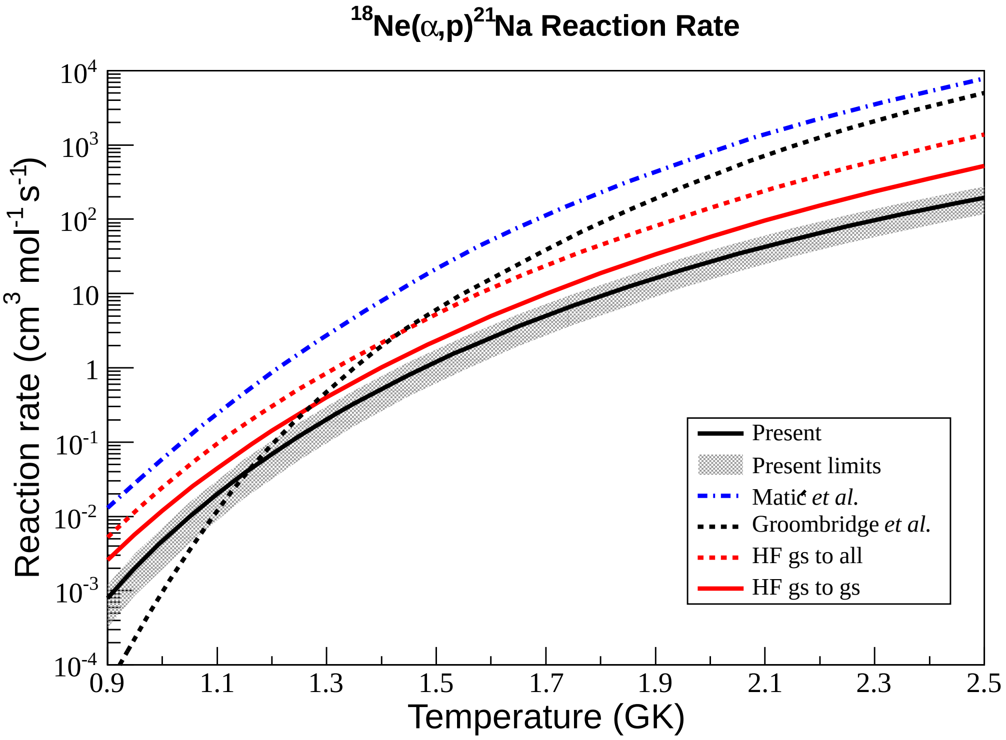

Figure 7.2: *The* ^{18}*Ne*(α,*p*)^{21}*Na reaction rate calculated as a function of temperature. The solid black line represents the arithmetic mean reaction rate based on the current work, with upper and lower limits shown as a dotted grey region. Other curves shown are the* HF_{gs} *(solid red) and* HF_{all} *(dashed red) calculations [46, 54], Matić et al. (dot-dashed blue) [34], and Groombridge et al. (dashed black) [29].*

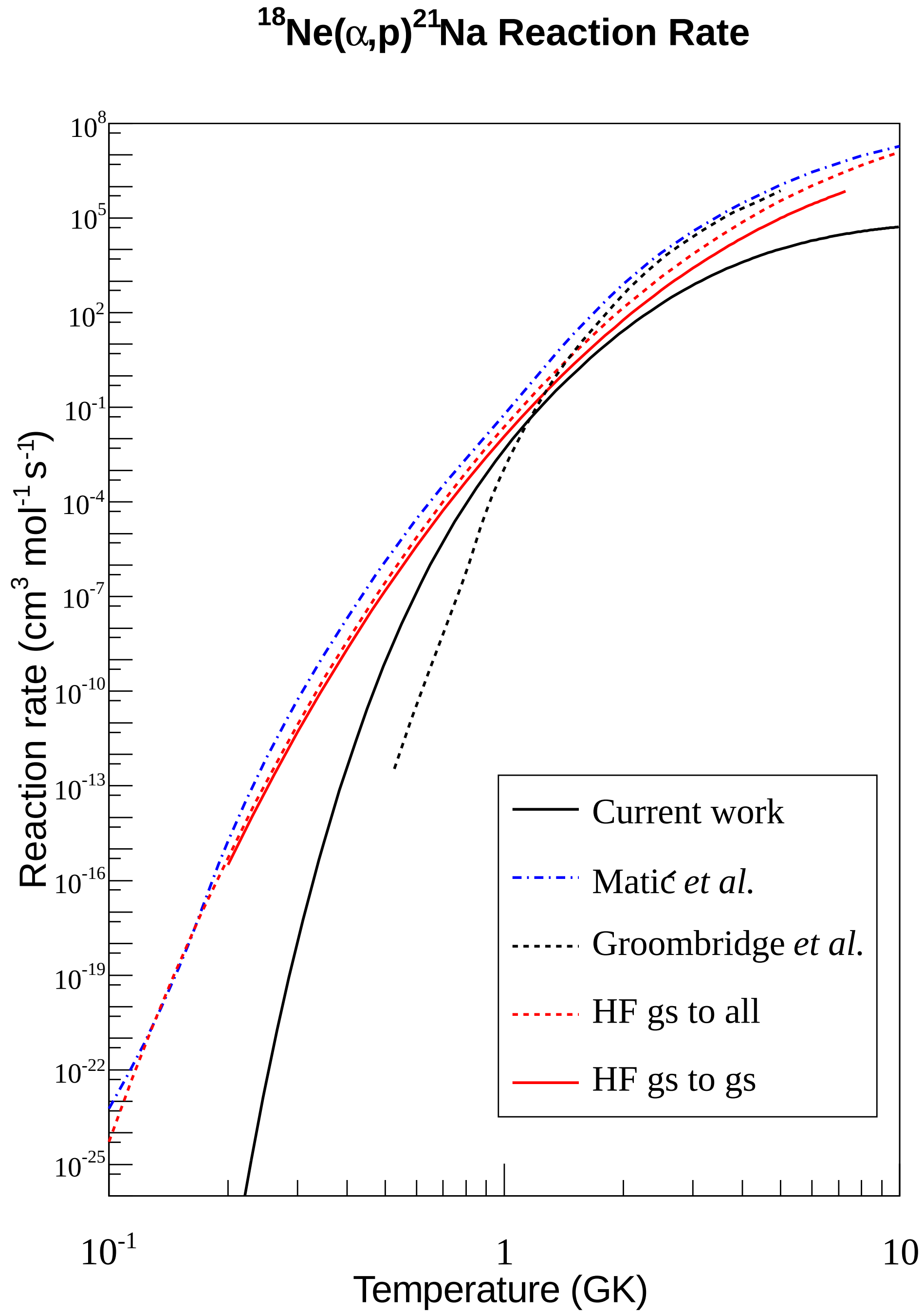

Figure 7.3: *The ^{18}Ne(α,p)^{21}Na reaction rate calculated as a function of temperature for the temperature range T = 0.1 - 10 GK. The solid black line represents the arithmetic mean reaction rate based on the current work. Other curves shown are the HF_{gs} (solid red) and HF_{all} (dashed red) calculations [46, 54], and the rates from Matić et al. (dot-dashed blue) [34] and Groombridge et al. (dashed black) [29].*

***Table 7.1**: Calculated rates of the ^{18}Ne(α,p)^{21}Na reaction as a function of temperature.*

Temperature	$N_A < \sigma v >$ (cm^3 mol^{-1} s^{-1})		
T_9 (K)	limit low	limit high	arithmetic mean
0.95	8.5×10^{-4}	3.2×10^{-3}	$(2.0 \pm 1.2)\times10^{-3}$
1.05	4.4×10^{-3}	1.6×10^{-2}	$(9.9 \pm 5.6)\times10^{-3}$
1.15	1.7×10^{-2}	5.9×10^{-2}	$(3.8 \pm 2.1)\times10^{-2}$
1.25	5.8×10^{-2}	1.8×10^{-1}	$(1.2 \pm 0.6)\times10^{-1}$
1.35	1.6×10^{-1}	5.0×10^{-1}	$(3.3 \pm 1.7)\times10^{-1}$
1.45	4.1×10^{-1}	1.2	$(8.0 \pm 3.9)\times10^{-1}$
1.55	9.4×10^{-1}	2.6	1.8 ± 0.8
1.65	2.0	5.3	3.6 ± 1.7
1.75	3.8	9.9	6.9 ± 3.1
1.85	6.9	$1.7\times10^{+1}$	$(1.2 \pm 0.5)\times10^{+1}$
1.95	$1.2\times10^{+1}$	$3.0\times10^{+1}$	$(2.1 \pm 0.9)\times10^{+1}$
2.05	$2.0\times10^{+1}$	$4.8\times10^{+1}$	$(3.4 \pm 1.4)\times10^{+1}$
2.15	$3.1\times10^{+1}$	$7.5\times10^{+1}$	$(5.3 \pm 2.2)\times10^{+1}$
2.25	$4.7\times10^{+1}$	$1.1\times10^{+2}$	$(8.0 \pm 3.3)\times10^{+1}$
2.35	$6.9\times10^{+1}$	$1.6\times10^{+2}$	$(1.2 \pm 0.5)\times10^{+2}$
2.45	$9.9\times10^{+1}$	$2.3\times10^{+2}$	$(1.7 \pm 0.7)\times10^{+2}$

sequence from the Hot-CNO cycle. Indeed, one could speculate that for a factor 2-3 lower reaction rate the breakout via the ^{18}Ne(α,p)^{21}Na reaction is delayed and would occur at higher temperatures than previously predicted.

***Table 7.2**: Minor increases in the final yields for a selection of species close to ^{18}Ne using the standard hydrodynamical model of a Type-I X-ray burst and a model with a factor 2.5 lower ^{18}Ne(α,p)^{21}Na reaction rate [82]. These minor increases in isotope abundance are an inherent consequence of the hydrodynamical models used and as such, no conclusions should be drawn from them [84].*

Isotope	Increase in final yield
^{18}Ne	×1.14
^{19}Ne	×1.03
^{20}Mg	×1.17
^{21}Mg	×1.15
^{22}Mg	×1.06
^{23}Al	×1.06
^{24}Si	×1.07
^{25}Si	×1.07
^{26}Si	×1.04
^{27}P	×1.05
^{28}S	×1.07
^{29}S	×1.07
^{30}S	×1.07

Chapter 8

Conclusions and Further Work

The ^{18}Ne(α,p)^{21}Na reaction is considered one of the key reactions in X-ray burst scenarios and forms one of the potential breakout sequences from the HCNO cycle, which can lead energy generation into the *rp*-process. The aim of this work was three-fold: a) the indirect measurement of the ^{18}Ne(α,p)^{21}Na cross section via the time-reverse ^{21}Na(p,α)^{18}Ne reaction in a wide energy region and at the lowest energy feasible, b) to test the validity of the Hauser-Feshbach (HF) statistical model for the calculation of the ^{18}Ne(α,p)^{21}Na cross section and, c) to perform a comparison with previous ANL time-reverse measurements.

The time-reverse reaction was studied at the ISAC II facility, TRIUMF, Canada. Measurements were made with thin $(CH_2)_n$ targets at six separate beam energies, corresponding to $E_{cm}(\alpha,p)$ = 2568, 1970, 1758, 1683, 1379 and 1194 keV; the measurement at E_{cm} = 1194 keV is the lowest energy measurement to date of the ^{18}Ne(α,p)^{21}Na cross section. Reaction alpha-particles and ^{18}Ne ions were detected by two sets of DSSSD ΔE-E telescopes. The ^{21}Na(p,α)^{18}Ne cross sections were determined and transformed to the ^{18}Ne(α,p)^{21}Na frame by detailed balance according to the reciprocity theorem. At $E_{cm} \geq 1683$ keV, the measured cross sections are up to a factor 2 lower than the NON-SMOKER HF calculations for ground-state to ground-state transitions [46, 54], and for 1194 keV $\leq E_{cm} \leq$ 1379 keV the two are in agreement. The discrepancy between our data and the HF calculations confirms that caution should be used with the application of the HF formalism for nuclei in this mass region.

Very good agreement is observed between the measured cross sections and the unpublished ANL measurements [42]; the current work improves on the

ANL measurements by measuring the cross section at a lower energy and measuring total cross sections rather than upper limits for $E_{cm} \leq 1600$ keV.

The ^{18}Ne(α,p)^{21}Na reaction rate was calculated over the experimental energy range and compared with the previous calculation of Matić *et al.* [34], and with the Hauser-Feshbach statistical model. The ^{18}Ne(α,p)^{21}Na reaction rate determined in this work was a factor 2-3 lower than the NON-SMOKER HF calculation for ground-state to ground-state transitions, and 1-1.5 orders of magnitude lower than the reaction rate determined by Matić *et al.* [34]. The astrophysical implications of this lower rate on the energy generation and nucleosynthesis in an X-ray burst are modest, but the breakout of the Hot-CNO cycle via the ^{18}Ne(α,p)^{21}Na reaction may occur at greater temperatures than previously estimated.

This work has also shown that the time-reverse technique is a useful approach for providing information on the ^{18}Ne(α,p)^{21}Na cross section, however, we feel we have reached the limit of what can be achieved by this approach because of the low cross sections involved (for example, at $E_{beam} = 4.120$ MeV/A it took 48 hours to detect two ^{21}Na(p,α)^{18}Ne reaction events). In order to extend the cross section measurements to lower energies which are more relevant to X-ray bursts, higher ^{21}Na beam intensities and hydrogen gas targets are required. However, both these approaches introduce additional complications. The use of a more intense ^{21}Na beam will increase the detected ^{18}Ne+^{4}He yield and therefore reduce the statistical error on the reaction yield. However, a more intense ^{21}Na beam will also increase the yield of scattered particles into the detectors, particularly if a solid $(CH_2)_n$ target is used, and thus increase the radiation damage to the silicon. Alternatively, a hydrogen gas target introduces complications such as those in relation to handling a gas target and resolving the interaction energy of a reaction within the gaseous target. Incidentally, this approach has been exploited for the study of another reaction of astrophysical interest and involves filling the TUDA scattering chamber with hydrogen gas [85]. Depending on the results from these measurements it may be beneficial to repeat the time-reverse measurement with a pure hydrogen gas target. However, no matter how many improvements are made to the time-reverse approach, an intrinsic limitation will always remain since the time-reverse approach can only access ground-state to ground-state transitions for the forward reaction. Thus, major improvements for the determination of the ^{18}Ne(α,p)^{21}Na reaction cross section can be achieved by a direct measurement. To reach the energy region of astrophysical interest, however, ^{18}Ne beam intensities in excess of 10^7 pps would be required. These are not available at present.

In summary, the work carried out in this thesis has measured the ^{18}Ne(α,p$_0$)^{21}Na cross section in the energy region $E_{cm}(\alpha,p)$ = 1.19 - 2.57 MeV, with the measurement at $E_{cm}(\alpha,p)$ = 1.19 MeV being the lowest energy measured to date.

Appendix A

Thickness Measurements of $(CH_2)_n$ and $(CD_2)_n$ targets

The thicknesses of the $(CH_2)_n$ and $(CD_2)_n$ targets produced by Paul Demaret at UCL, Louvain-la-Neuve (LLN), Belgium, and Carmelo Marchetta at INFS LNS-Catania, Italy, were measured at Edinburgh prior to the ^{21}Na(p,α)^{18}Ne experiment.

Under vacuum conditions, a collimated beam of alpha particles was directed onto a selected target, as shown in Figure A.1. A standard mixed-alpha closed source containing ^{239}Pu,^{241}Am and ^{244}Cm was used. The alpha source was collimated twice: a 2 mm diameter collimator was placed over the $\sim$ 5 mm diameter active surface of the source, and a second collimator, 4 mm in diameter, was positioned immediately before the silicon detector. This arrangement of collimators produced an effective beam spread of 5.8° and a beam spot diameter of 1.4 mm. A target ladder was manufactured such that the target area in the beam spot could be changed; for each target three measurements were made: one with the beam spot at the centre of the target, and one at each of the two target edges. Immediately after the target position was a brass snout with small bar magnets positioned above and below the beam line. These magnets were used to suppress *delta* electrons knocked out of the target, by deflecting the electrons out of the beam line. A Canberra Passivated Implanted Planar Silicon (PIPS) detector, [86], was positioned at the end of the beam line for the detection of the alpha particles. The detector dead-layer was assumed to be $\sim$ 50 nm, as quoted on the Canberra website. A Cooknell EC572

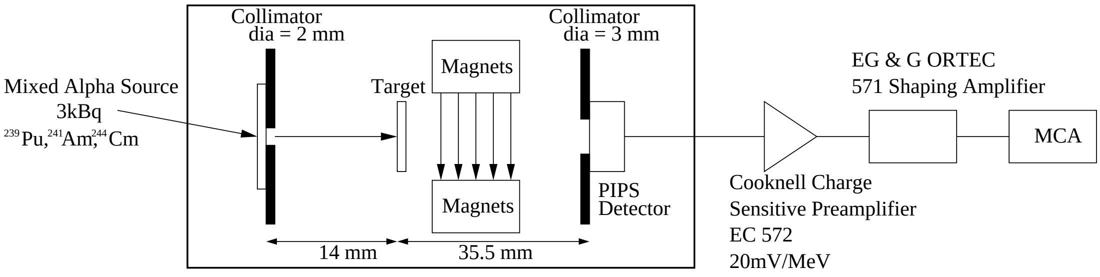

Figure A.1: *Schematic of the experimental setup for the thickness measurements of the* $(CH_2)_n$ *and* $(CD_2)_n$ *targets.*

Charge Sensitive Preamplifier and an EG & G ORTEC 571 Shaping amplifier were used with the PIPS detector. The PIPS detector was calibrated using the mixed-alpha source with no target at the target position; it was assumed there was no energy loss on the alpha particles exiting the source.

For each target, alpha particles from the mixed-alpha source were detected in the PIPS detector after having experienced energy loss through the target. The centroid peaks were identified on the resulting triple peaked energy spectrum, and the measured alpha particle energies calculated with knowledge of the detector gain and offset. Using SRIM-2008, [67], the range in $(CH_2)_n$ or $(CD_2)_n$ of the degraded alpha particles was determined. SRIM-2008 was then used to calculate the range in $(CH_2)_n$ or $(CD_2)_n$ of the same alpha particles at the nominal energies they were emitted from the source, *i.e.* without any energy loss. The thickness of the target was determined by subtracting the range of the degraded alpha particles from the nominal range of the alpha particles.

In addition, the FWHM values of the alpha peaks were recorded for all targets. For each target, the energy resolution of the detector, $\sim$ 15 keV, was added in quadrature with the energy straggling calculated from TRIM-2008 [67], and compared with the observed FWHM. Any significant discrepancy between measured and estimated FWHM is an indication of non-uniformity in the target.

A summary of the measured thicknesses is given in Table A.1; the density of polyethylene is 0.93 g/cm^3. The error accompanying each measured thickness is from the random error due to centroid identification (± 1 channel), and the systematic error of 5.6% [10] for all stopping power calculations within SRIM-2008. The overall error associated to the target thickness is 8%. The

Table A.1: Measured target thicknesses. Targets are $(CH_2)_n$ unless otherwise stated.

Target	Nominal Thickness (μg/cm^2)	Measured Thickness (μg/cm^2)	^{241}Am FWHM (± 5.7) (keV)	TRIM ^{241}Am FWHM (keV)
Catania POS 1	352	359 ± 29	108.5	31.9
Catania POS 2	389	387 ± 31	96.2	33.6
Catania POS 3	332	326 ± 27	86.0	30.0
Catania POS 4	339	353 ± 28	74.9	31.2
Catania POS 5	391	392 ± 31	68.0	26.0
Catania POS 6	321	310 ± 25	29.8	26.0
250 LLN #1	250	258 ± 21	34.1	38.0
250 LLN #2	250	292 ± 23	33.1	30.6
250 LLN #3	250	233 ± 19	32.3	28.0
80 LLN	80	78 ± 6	25.3	20.2
Catania $(CD_2)_n$	322	368 ± 26	45.7	42.1

error accompanying the FWHM measurements is from the random error due to channel identification of the FWHM (± 2 channels).

The non-uniformity in the Catania targets POS 1 to POS 5 was unacceptable for the ^{21}Na(p,α)^{18}Ne experiment; the thickness measurements were repeated, however, similar results were observed. As such, targets POS 1 to POS 5 were removed from the batch of targets available for the experiment.

Appendix B

Energy Loss of a Charged Particle Through a Medium

All energy loss calculations performed in this work used the Ion Range Tables calculated by the SRIM-2008 software [67]. The SRIM-2008 program calculates ion stopping powers, and hence ion range, in a medium for a user defined range of ion energies. The calculations are based on experimental stopping powers and the Bethe formula:

$$-\frac{dE}{dx} = \frac{4\pi e^4 Z^2}{m_0 v^2} NB \tag{B.1}$$

where

$$B \equiv Z\left[\ln\frac{2m_0 v^2}{I} - \ln\left(1 - \frac{v^2}{c^2}\right) - \frac{v^2}{c^2}\right] \tag{B.2}$$

and v and Ze are the velocity and charge of the incident particle, N and Z are the number density and atomic number of the absorbing atoms, m_0 is the electron rest mass, e the electron charge and I is the experimentally determined average excitation and ionisation potential of the absorber [56]. An example range table output from SRIM-2008 program is shown in Figure B.1.

To calculate the energy loss of an ion at a known initial energy, a Fortran program was written to read in the SRIM range table and interpolate between the energies in the table. The code used was heavily modified from a subroutine originally written by Dr. Alex Murphy [74]. SRIM tables, like the one in Figure B.1, were created for all ions and mediums of interest, up to energies of 1 GeV.

```
Sodium in Polyethylene       Wed Jul 07 17:44:34 2010       1
 ==================================================================
              Calculation using SRIM-2006
              SRIM version ---> SRIM-2008.03
              Calc. date   ---> October 28, 2009
 ==================================================================

 Disk File Name = SRIM Outputs\Sodium in Polyethylene

 Ion = Sodium [11] , Mass = 20.998 amu

 Target Density =  9.3000E-01 g/cm3 = 1.1979E+23 atoms/cm3
 ======= Target  Composition ========
    Atom   Atom   Atomic    Mass
    Name   Numb   Percent   Percent
    ----   ----   -------   -------
      H      1    066.67    014.37
      C      6    033.33    085.63
 ====================================
 Bragg Correction = 0.54%
 Stopping Units =  keV / micron
 See bottom of Table for other Stopping units

   Ion        dE/dx      dE/dx     Projected  Longitudinal   Lateral
  Energy      Elec.      Nuclear     Range     Straggling   Straggling
-----------  ---------- ---------- ----------  ----------  ----------
  10.00 keV   6.555E+01  2.406E+02     325 A        94 A        71 A
  11.00 keV   6.875E+01  2.384E+02     354 A       101 A        77 A
  12.00 keV   7.181E+01  2.361E+02     382 A       108 A        82 A
  13.00 keV   7.474E+01  2.337E+02     411 A       115 A        87 A
  14.00 keV   7.756E+01  2.313E+02     439 A       121 A        92 A
  15.00 keV   8.028E+01  2.288E+02     468 A       128 A        97 A
  16.00 keV   8.292E+01  2.263E+02     496 A       135 A       102 A
  17.00 keV   8.547E+01  2.238E+02     525 A       141 A       107 A
  18.00 keV   8.795E+01  2.213E+02     553 A       147 A       112 A
  20.00 keV   9.270E+01  2.164E+02     611 A       160 A       121 A
  22.50 keV   9.833E+01  2.105E+02     683 A       176 A       133 A
  25.00 keV   1.036E+02  2.049E+02     756 A       191 A       145 A
  27.50 keV   1.087E+02  1.996E+02     829 A       206 A       157 A
  30.00 keV   1.135E+02  1.945E+02     902 A       220 A       169 A
  32.50 keV   1.182E+02  1.898E+02     975 A       235 A       180 A
  35.00 keV   1.226E+02  1.852E+02    1049 A       249 A       192 A
  37.50 keV   1.269E+02  1.809E+02    1123 A       262 A       203 A
  40.00 keV   1.311E+02  1.768E+02    1197 A       276 A       215 A
  45.00 keV   1.394E+02  1.693E+02    1345 A       302 A       237 A
  50.00 keV   1.462E+02  1.624E+02    1494 A       327 A       259 A
  55.00 keV   1.516E+02  1.562E+02    1644 A       352 A       281 A
  60.00 keV   1.563E+02  1.505E+02    1794 A       376 A       303 A
  65.00 keV   1.606E+02  1.452E+02    1945 A       399 A       325 A
  70.00 keV   1.646E+02  1.404E+02    2098 A       422 A       346 A
  80.00 keV   1.722E+02  1.318E+02    2404 A       466 A       388 A
  90.00 keV   1.796E+02  1.244E+02    2712 A       509 A       429 A
 100.00 keV   1.870E+02  1.179E+02    3021 A       549 A       470 A
 110.00 keV   1.945E+02  1.121E+02    3329 A       588 A       510 A
 120.00 keV   2.021E+02  1.070E+02    3635 A       625 A       549 A
 130.00 keV   2.097E+02  1.024E+02    3940 A       659 A       587 A
 140.00 keV   2.172E+02  9.821E+01    4243 A       693 A       625 A
 150.00 keV   2.248E+02  9.442E+01    4542 A       724 A       661 A
 160.00 keV   2.323E+02  9.095E+01    4839 A       754 A       696 A
 170.00 keV   2.397E+02  8.777E+01    5132 A       783 A       731 A
 180.00 keV   2.469E+02  8.484E+01    5422 A       810 A       764 A
 200.00 keV   2.611E+02  7.960E+01    5992 A       862 A       828 A
 225.00 keV   2.780E+02  7.402E+01    6685 A       922 A       904 A
 250.00 keV   2.940E+02  6.927E+01    7359 A       976 A       974 A
 275.00 keV   3.092E+02  6.517E+01    8013 A      1025 A      1040 A
 300.00 keV   3.237E+02  6.158E+01    8651 A      1070 A      1102 A
 325.00 keV   3.376E+02  5.842E+01    9271 A      1110 A      1160 A
 350.00 keV   3.512E+02  5.561E+01    9876 A      1148 A      1215 A
 375.00 keV   3.643E+02  5.309E+01    1.05 um     1182 A      1266 A
 400.00 keV   3.773E+02  5.082E+01    1.10 um     1214 A      1315 A
 450.00 keV   4.024E+02  4.688E+01    1.22 um     1276 A      1405 A
```

```
Sodium in Polyethylene       Wed Jul 07 17:44:34 2010       2
 500.00 keV   4.267E+02  4.357E+01    1.32 um     1330 A      1486 A
 550.00 keV   4.504E+02  4.074E+01    1.42 um     1377 A      1560 A
 600.00 keV   4.734E+02  3.830E+01    1.52 um     1419 A      1627 A
 650.00 keV   4.959E+02  3.617E+01    1.62 um     1457 A      1689 A
 700.00 keV   5.178E+02  3.428E+01    1.71 um     1490 A      1746 A
 800.00 keV   5.605E+02  3.110E+01    1.88 um     1558 A      1847 A
 900.00 keV   6.017E+02  2.852E+01    2.04 um     1614 A      1935 A
   1.00 MeV   6.420E+02  2.637E+01    2.19 um     1662 A      2011 A
   1.10 MeV   6.814E+02  2.455E+01    2.34 um     1703 A      2079 A
   1.20 MeV   7.203E+02  2.299E+01    2.47 um     1739 A      2139 A
   1.30 MeV   7.586E+02  2.163E+01    2.60 um     1770 A      2194 A
   1.40 MeV   7.965E+02  2.044E+01    2.73 um     1798 A      2242 A
   1.50 MeV   8.340E+02  1.938E+01    2.85 um     1822 A      2287 A
   1.60 MeV   8.711E+02  1.844E+01    2.96 um     1844 A      2327 A
   1.70 MeV   9.078E+02  1.760E+01    3.07 um     1864 A      2364 A
   1.80 MeV   9.441E+02  1.683E+01    3.18 um     1882 A      2398 A
   2.00 MeV   1.015E+03  1.550E+01    3.38 um     1924 A      2458 A
   2.25 MeV   1.101E+03  1.413E+01    3.61 um     1973 A      2522 A
   2.50 MeV   1.184E+03  1.300E+01    3.82 um     2013 A      2576 A
   2.75 MeV   1.262E+03  1.205E+01    4.02 um     2048 A      2623 A
   3.00 MeV   1.335E+03  1.124E+01    4.21 um     2077 A      2663 A
   3.25 MeV   1.403E+03  1.054E+01    4.40 um     2103 A      2699 A
   3.50 MeV   1.467E+03  9.930E+00    4.57 um     2127 A      2731 A
   3.75 MeV   1.526E+03  9.392E+00    4.73 um     2147 A      2759 A
   4.00 MeV   1.580E+03  8.913E+00    4.89 um     2166 A      2785 A
   4.50 MeV   1.674E+03  8.098E+00    5.20 um     2221 A      2831 A
   5.00 MeV   1.753E+03  7.430E+00    5.49 um     2269 A      2871 A
   5.50 MeV   1.818E+03  6.871E+00    5.77 um     2311 A      2905 A
   6.00 MeV   1.872E+03  6.396E+00    6.04 um     2350 A      2936 A
   6.50 MeV   1.916E+03  5.986E+00    6.30 um     2386 A      2964 A
   7.00 MeV   1.951E+03  5.630E+00    6.56 um     2420 A      2989 A
   8.00 MeV   2.003E+03  5.038E+00    7.06 um     2533 A      3035 A
   9.00 MeV   2.035E+03  4.566E+00    7.55 um     2636 A      3075 A
  10.00 MeV   2.051E+03  4.180E+00    8.04 um     2733 A      3112 A
  11.00 MeV   2.056E+03  3.858E+00    8.53 um     2825 A      3145 A
  12.00 MeV   2.053E+03  3.585E+00    9.01 um     2914 A      3177 A
  13.00 MeV   2.043E+03  3.350E+00    9.50 um     3000 A      3207 A
  14.00 MeV   2.029E+03  3.146E+00    9.99 um     3085 A      3235 A
  15.00 MeV   2.010E+03  2.967E+00   10.48 um     3169 A      3263 A
  16.00 MeV   1.989E+03  2.809E+00   10.98 um     3252 A      3290 A
  17.00 MeV   1.966E+03  2.667E+00   11.49 um     3334 A      3316 A
  18.00 MeV   1.941E+03  2.541E+00   12.00 um     3417 A      3342 A
  20.00 MeV   1.890E+03  2.322E+00   13.04 um     3730 A      3392 A
  22.50 MeV   1.823E+03  2.099E+00   14.39 um     4198 A      3454 A
  25.00 MeV   1.758E+03  1.917E+00   15.78 um     4648 A      3516 A
  27.50 MeV   1.694E+03  1.766E+00   17.23 um     5088 A      3579 A
  30.00 MeV   1.634E+03  1.638E+00   18.73 um     5522 A      3643 A
  32.50 MeV   1.577E+03  1.528E+00   20.29 um     5953 A      3708 A
  35.00 MeV   1.524E+03  1.433E+00   21.90 um     6382 A      3775 A
  37.50 MeV   1.474E+03  1.350E+00   23.57 um     6812 A      3844 A
  40.00 MeV   1.427E+03  1.276E+00   25.29 um     7243 A      3915 A
  45.00 MeV   1.362E+03  1.152E+00   28.87 um     8857 A      4063 A
  50.00 MeV   1.304E+03  1.051E+00   32.62 um     1.03 um     4219 A
  55.00 MeV   1.236E+03  9.669E-01   36.56 um     1.18 um     4385 A
  60.00 MeV   1.176E+03  8.960E-01   40.71 um     1.32 um     4560 A
  65.00 MeV   1.122E+03  8.352E-01   45.06 um     1.45 um     4746 A
  70.00 MeV   1.075E+03  7.826E-01   49.61 um     1.59 um     4943 A
  80.00 MeV   9.928E+02  6.959E-01   59.29 um     2.10 um     5368 A
  90.00 MeV   9.250E+02  6.273E-01   69.72 um     2.57 um     5835 A
 100.00 MeV   8.675E+02  5.715E-01   80.88 um     3.02 um     6343 A
 110.00 MeV   8.180E+02  5.253E-01   92.75 um     3.46 um     6889 A
 120.00 MeV   7.747E+02  4.864E-01  105.30 um     3.89 um     7472 A
 130.00 MeV   7.364E+02  4.531E-01  118.54 um     4.32 um     8091 A
 140.00 MeV   7.022E+02  4.242E-01  132.44 um     4.75 um     8743 A
 150.00 MeV   6.714E+02  3.990E-01  147.00 um     5.18 um     9429 A
 160.00 MeV   6.434E+02  3.767E-01  162.21 um     5.61 um     1.01 um
 170.00 MeV   6.178E+02  3.569E-01  178.07 um     6.04 um     1.09 um
 180.00 MeV   5.944E+02  3.392E-01  194.56 um     6.48 um     1.17 um
 200.00 MeV   5.527E+02  3.088E-01  229.45 um     8.15 um     1.33 um
 225.00 MeV   5.084E+02  2.779E-01  276.61 um    10.54 um     1.55 um
```

```
Sodium in Polyethylene        Wed Jul 07 17:44:34 2010       3
 250.00 MeV   4.710E+02  2.529E-01  327.69 um    12.79 um     1.79 um
 275.00 MeV   4.388E+02  2.322E-01  382.68 um    14.98 um     2.05 um
 300.00 MeV   4.108E+02  2.148E-01  441.56 um    17.14 um     2.32 um
 325.00 MeV   3.863E+02  1.999E-01  504.30 um    19.31 um     2.62 um
 350.00 MeV   3.648E+02  1.870E-01  570.88 um    21.50 um     2.92 um
 375.00 MeV   3.456E+02  1.758E-01  641.28 um    23.70 um     3.25 um
 400.00 MeV   3.286E+02  1.659E-01  715.45 um    25.93 um     3.59 um
 450.00 MeV   2.996E+02  1.492E-01  874.81 um    34.38 um     4.31 um
 500.00 MeV   2.760E+02  1.356E-01    1.05 mm    42.29 um     5.10 um
 550.00 MeV   2.566E+02  1.245E-01    1.24 mm    49.97 um     5.95 um
 600.00 MeV   2.404E+02  1.151E-01    1.44 mm    57.53 um     6.86 um
 650.00 MeV   2.262E+02  1.070E-01    1.65 mm    65.06 um     7.82 um
 700.00 MeV   2.129E+02  1.001E-01    1.88 mm    72.63 um     8.83 um
 800.00 MeV   1.910E+02  8.867E-02    2.38 mm   101.02 um    11.03 um
 900.00 MeV   1.737E+02  7.968E-02    2.92 mm   127.48 um    13.45 um
   1.00 GeV   1.595E+02  7.241E-02    3.53 mm   153.27 um    16.08 um
-----------------------------------------------------------
 Multiply Stopping by        for Stopping Units
 -------------------        ------------------
  1.0000E-01                 eV / Angstrom
  1.0000E+00                keV / micron
  1.0000E+00                MeV / mm
  1.0753E-02                keV / (ug/cm2)
  1.0753E-02                MeV / (mg/cm2)
  1.0753E+01                keV / (mg/cm2)
  8.3481E-02                 eV / (1E15 atoms/cm2)
  1.0778E-03                L.S.S. reduced units
 ==================================================================
 (C) 1984,1989,1992,1998,2008 by J.P. Biersack and J.F. Ziegler
```

Figure B.1: *SRIM-2008 range table output for* ^{21}*Na in Polyethylene -* $(CH_2)_n$.

For a user defined ion, medium and energy of interest, the program selected the corresponding SRIM range table, and interpolated between the energy/range intervals to determine the range of the ion in the medium. After the user input of the target medium thickness, the program subtracts the medium thickness from the extracted ion range and re-interpolates between the energy/range intervals to extract the corresponding new energy. The program assumes the stopping power is linear between the energy/range intervals of the SRIM range table.

Appendix C

Rutherford Scattering

The material presented here has been taken from [87], and the reader is strongly advised to read on in [87] for further reading on two-body reaction kinematics. Consider the scattering of two ions in the Coulomb field, with masses A_1 and A_2, and charge Z_1e and Z_2e respectively, as illustrated in Figure C.1. The distance of closest approach, D, between the two centres of mass and the centre-of-mass scattering angle, Θ, are related by

$$D = a\left(1 + \mathrm{cosec}\frac{\Theta}{2}\right) \tag{C.1}$$

where a is defined as one-half the distance of closest approach in a head-on collision ($\Theta = 180°$):

$$a = \frac{Z_1 Z_2 e^2}{\mu v_\infty^2} \tag{C.2}$$

with μ as the reduced mass of the system, $\mu = A_1A_2/(A_1 + A_2)$, and v_∞ as the initial velocity of the approaching projectile. If one considers a and the asymptotic wavelength of relative motion at large separation, $\lambda\!\!\!^{-} = \hbar/\mu v_\infty$, one can obtain the Sommerfeld parameter:

$$n = \frac{a}{\lambda\!\!\!^{-}} = \frac{Z_1 Z_2 e^2}{\hbar v_\infty} \tag{C.3}$$

Considering the the two constants of motion for a particle: the total energy $E_{cm} = \frac{1}{2}\mu v_\infty^2$, and classical angular momentum $L\hbar$ (where L is used for classical momenta, and l for quantised angular momenta, both in units of $\hbar$.), the requirement of energy conservation from infinity to the point of closest

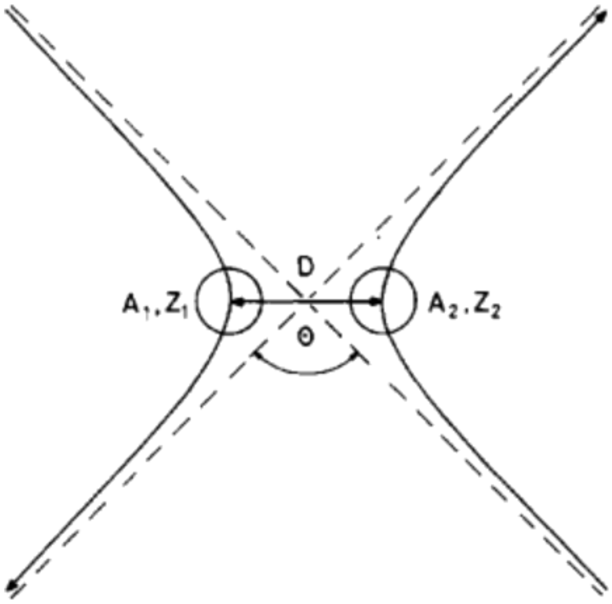

Figure C.1: *Coulomb scattered trajectories in the centre of mass system [87].*

approach gives:

$$E_{cm} = \frac{Z_1 Z_2 e^2}{D} + \frac{L^2 \hbar^2}{2\mu D^2} \tag{C.4}$$

If the Sommerfeld parameter (Equation C.3) and $k = \mu v_\infty/\hbar$ are inserted into the above equation, one obtains:

$$L^2 = kD(kD - 2n) \tag{C.5}$$

and

$$kD = n + (n^2 + L^2)^{1/2} \tag{C.6}$$

From Equations C.1, C.3 and C.6, the scattering angle, Θ, can be expressed in terms of n and L:

$$\sin\frac{\Theta}{2} = \frac{n}{kD - n} = \frac{n}{(n^2 + L^2)^{1/2}} \tag{C.7}$$

If we define the Coulomb barrier, E_c, as the asymptotic kinetic energy in the centre of mass system at the classical threshold for nuclear reactions *i.e.* $D \approx R_c$, and the Coulomb interaction distance:

$$R_c = r_{0c}\,(A_1^{1/3} + A_2^{1/3}) \tag{C.8}$$

as the corresponding distance of closest approach in the absence of nuclear interactions, with r_{0c} = 1.2-1.5 fm. From $E_{cm} = \frac{1}{2}\mu v_\infty^2$ and Equation C.2, and with $2a = R_c$ and $E_{cm} = E_c$:

$$E_c = \mu\epsilon_c = \frac{Z_1 Z_2 e^2}{R_c} \tag{C.9}$$

where ϵ_c:

$$\epsilon_c = \frac{E_c}{A_{12}} = \frac{Z_1 Z_2 e^2}{A_{12} R_c} \tag{C.10}$$

Equation C.9 is the the Coulomb potential between two spherically symmetric, non-penetrating charge distributions with total charges $Z_1 e$ and $Z_2 e$ at a distance R_c.

For bombarding energies above the Coulomb barrier, there are two different kinematic situations depending on whether the distance of closest approach is greater or less than R_c. For large impact parameters, corresponding to small scattering angles, the particles follow Coulomb trajectories as shown in Figure C.1. For small impact parameters, the collision is dominated by nuclear interactions and usually leads to inelastic processes. For the limiting case of a *'grazing collision'* (*i.e.* $D = R_c$), the *grazing* angle (in the centre of mass) for Coulomb scattering is obtained from Equation C.7:

$$\sin\frac{\Theta_{gr}}{2} = \frac{n}{kR_c - n} = \frac{\epsilon_c}{2\epsilon - \epsilon_c} \tag{C.11}$$

where:

$$\epsilon = \frac{E_{lab}}{A_1} = \frac{E_{cm}}{\mu} = \frac{m}{2} v_\infty^2 \tag{C.12}$$

In the laboratory reference frame, the *grazing* angle, θ_{gr}, is given by:

$$\tan\theta_{gr} = \frac{\sin\Theta_{gr}}{\cos\Theta_{gr} + \gamma_3} \tag{C.13}$$

where $\gamma_3 = A_1/A_2$.

Bibliography

[1] E. M. Burbidge, G. R. Burbidge, W. A. Fowler, and F. Hoyle, Reviews of Modern Physics **29**, 547 (1957).

[2] R. Narayan and R. L. Cooper, The Astrophysical Journal **665**, 628 (2007).

[3] R. Wijnands and M. van der Klis, Astronomy and Astrophysics **345**, L35 (1999).

[4] A. Zezas *et al.*, The Astrophysical Journal **661**, 135 (2007).

[5] M. Suzuki *et al.*, Publications of the Astronomical Society of Japan **59**, 263 (2007).

[6] M. Ajello *et al.*, The Astrophysical Journal **673**, 96 (2008).

[7] J. José and C. Iliadis, Reports on Progress in Physics **74**, 096901 (2011).

[8] S. E. Woosley and R. E. Taam, Nature **263**, 101 (1976).

[9] F. Haberl *et al.*, The Astrophysical Journal **314**, 266 (1987).

[10] C. Iliadis, *Nuclear Physics of Stars* (Wiley-VCH, New York, 2007).

[11] H. Schatz *et al.*, Physics Reports **294**, 167 (1998).

[12] R. K. Wallace and S. E. Woosley, The Astrophysical Journal Supplement Series **45**, 389 (1981).

[13] S. Ayasli and P. C. Joss, The Astrophysical Journal **256**, 637 (1982).

[14] R. E. Taam, Annual Review of Nuclear and Particle Science **35**, 1 (1985).

[15] M. Y. Fujimoto, M. Sztajno, W. H. G. Lewin, and J. van Paradijs, The Astrophysical Journal **319**, 902 (1987).

[16] R. E. Taam, S. E. Woosley, T. A. Weaver, and D. Q. Lamb, The Astrophysical Journal **413**, 324 (1993).

[17] W. H. G. Lewin, J. van Paradijs, and R. E. Taam, Space Science Reviews **62**, 223 (1993).

[18] D. A. Hardy, http://www.astroart.org, (12 July 2011).

[19] B. Davids *et al.*, Physical Review C **67**, 012801 (2003).

[20] H. Schatz, International Journal of Mass Spectrometry **251**, 293 (2006).

[21] A. A. Chen *et al.*, Physical Review C **63**, 065807 (2001).

[22] J. L. Fisker, H. Schatz, and F.-K. Thielemann, The Astrophysical Journal Supplement Series **174**, 261 (2008).

[23] J. José, F. Moreno, A. Parikh, and C. Iliadis, The Astrophysical Journal Supplement Series **189**, 204 (2010).

[24] C. E. Rolfs and W. S. Rodney, *Cauldrons in the Cosmos* (University of Chicago Press, Chicago, 1988).

[25] C. Angulo *et al.*, Nuclear Physics A **656**, 3 (1999).

[26] J. Görres, M. Wiescher, and F.-K. Thielemann, Physical Review C **51**, 392 (1995).

[27] F.-K. Thielemann, M. Arnould, and T. J. W., in *Advance in Nuclear Astrophysics*, edited by E. Vangioni-Flam (Editions Frontière, Gif sur Yvette, 1987), p. 525.

[28] W. Bradfield-Smith *et al.*, Physical Review C **59**, 3402 (1999).

[29] D. Groombridge *et al.*, Physical Review C **66**, 055802 (2002).

[30] N. Bateman *et al.*, Physical Review C **63**, 035803 (2001).

[31] S. Michimasa *et al.*, The European Physical Journal A - Hadrons and Nuclei **14**, 275 (2002).

[32] B. Davids *et al.*, Physical Review C **68**, 055805 (2003).

[33] K. Y. Chae *et al.*, Physical Review C **79**, 055804 (2009).

[34] A. Matic *et al.*, Physical Review C **80**, 055804 (2009).

[35] J. A. Caggiano *et al.*, Physical Review C **66**, 015804 (2002).

[36] G. P. A. Berg *et al.*, Nuclear Physics A **718**, 608 (2003).

[37] S. Bishop *et al.*, Physical Review Letters **90**, 162501 (2003).

[38] J. M. D'Auria *et al.*, Physical Review C **69**, 065803 (2004).

[39] C. Ruiz *et al.*, Physical Review C **71**, 025802 (2005).

[40] J. J. He *et al.*, Physical Review C **80**, 015801 (2009).

[41] S. Sinha *et al.*, Argonne National Laboratory Annual Report, p8–10, (2003) (unpublished).

[42] S. Sinha *et al.*, Argonne National Laboratory Annual Report, p6–7, (2004) (unpublished).

[43] Private communication with C. Angulo, 2006.

[44] L. Wolfenstein, Physical Review **82**, 690 (1951).

[45] W. Hauser and H. Feshbach, Physical Review **87**, 366 (1952).

[46] T. Rauscher and F.-K. Thielemann, Atomic Data and Nuclear Data Tables **75**, 1 (2000).

[47] I. J. Thompson and F. M. Nunes, *Nuclear Reactions for Astrophysics* (Cambridge University Press, UK, 2009).

[48] K. Langanke, Nuclear Physics A **778**, 233 (2006).

[49] H. A. Bethe, Phys. Rev. **50**, 332 (1936).

[50] W. Dilg, W. Schantl, H. Vonach, and M. Uhl, Nuclear Physics A **217**, 269 (1973).

[51] T. Rauscher, F.-K. Thielemann, and K.-L. Kratz, Nuclear Physics A **621**, 331 (1997).

[52] T. Rauscher, F.-K. Thielemann, and K.-L. Kratz, Physical Review C **56**, 1613 (1997).

[53] T. Rauscher and F.-K. Thielemann, in *Stellar Evolution, Stellar Explosions and Galactic Chemical Evolution*, edited by A. Mezzacappa (IOP, Bristol, 1998), p. 519.

[54] T. Rauscher and F.-K. Thielemann, Atomic Data and Nuclear Data Tables **79**, 47 (2001).

[55] T. Rauscher, http://nucastro.org/reaclib.html, (18 May 2011).

[56] G. F. Knoll, *Radiation Detection and Measurement* (John Wiley & Sons, Inc., 2000).

[57] F. S. Goulding and B. G. Harvey, Annual Review of Nuclear Science **25**, 167 (1975).

[58] F. S. Goulding and D. A. Landis, Semiconductor Nuclear-Particle Detctors and Circuits **1**, 757 (1969).

[59] TRIUMF, http://legacyweb.triumf.ca/isac/isacIIa-03.pdf, (10 May 2011).

[60] M. Marchetto *et al.*, The European Physical Journal - Special Topics **150**, 241 (2007).

[61] A. Shotter, Nuclear Physics A **752**, 532 (2005).

[62] J. F. Baugh, C. E. Burkhardt, J. J. Leventhal, and T. Bergeman, Physical Review A **58**, 1585 (1998).

[63] K. Jayamanna *et al.*, Review of Scientific Instruments **79**, 02C711 (2008).

[64] R. Laxdal *et al.*, presented at EPAC98, 6^{th} European Particle Accelerator Conference, Stockholm, June 22-26 (2008) (unpublished).

[65] http://www.micronsemiconductor.co.uk/, (12 July 2011).

[66] Private communication with T. Davinson, Jan 2009.

[67] J. F. Ziegler, http://www.srim.org/, (12 July 2011).

[68] S. Thomas, T. Davinson, and A. Shotter, Nuclear Instruments and Methods in Physics Research Section A: Accelerators, Spectrometers, Detectors and Associated Equipment **288**, 212 (1990), Proceedings of the Fifth European Symposium on Semiconductors Detectors.

[69] http://www.bergquistcompany.com, (12 July 2011).

[70] http://www.ftssystems/rschillerback.htm, (12 July 2011).

[71] http://npg.dl.ac.uk/MIDAS/, (12 July 2011).

[72] http://www.oracle.com/uk/index.html, (12 July 2011).

[73] http://www.berkeleynucleonics.com/products/model-pb4.html, (12 July 2011).

[74] C. E. Beer *et al.*, Physical Review C **83**, 042801 (2011).

[75] http://root.cern.ch/drupal/, (12 July 2011).

[76] K. S. Krane, *Introductory Nuclear Physics* (John Wiley & Sons, Inc., 1988).

[77] http://www.nndc.bnl.gov/nudat2/, (3 August 2011).

[78] G. J. Feldman and R. D. Cousins, Physical Review D **57**, 3873 (1998).

[79] C. M. Deibel *et al.*, Phys. Rev. C **84**, 045802 (2011).

[80] T. Rauscher, http://nucastro.org/codes.html, *exp2rate* version 2.1 (15 March 2012).

[81] A. Matić, Ph.D. thesis, University of Groningen, 2007.

[82] Private communication with J. José, Oct 2011.

[83] A. Parikh, J. José, F. Moreno, and C. Iliadis, The Astrophysical Journal Supplement Series **178**, 110 (2008).

[84] Private communication with J. José, Feb 2012.

[85] J. Brown *et al.*, proposal S1287, https://mis.triumf.ca/science/experiment/view/727 (unpublished).

[86] http://www.canberra.com/products/505.asp, (1 August 2011).

[87] R. Bass, *Nuclear Reactions with Heavy Ions* (Springer-Verlag, Berlin Heidelberg New York, 1980).